

The first phase of planet formation: Collisional behavior and mechanical properties of dust aggregates

Dissertation

der Mathematisch-Naturwissenschaftlichen Fakultät

der Eberhard Karls Universität Tübingen

zur Erlangung des Grades eines

Doktors der Naturwissenschaften

(Dr. rer. nat.)

vorgelegt von

Konstantin Alexander Seizinger

aus Stuttgart

Tübingen

2013

Tag der mündlichen Qualifikation:

29.01.2014

Dekan:

Prof. Dr. Wolfgang Rosenstiel

1. Berichterstatter:

Prof. Dr. Wilhelm Kley

2. Berichterstatter:

Prof. Dr. Jürgen Blum

3. Berichterstatter:

Prof. Dr. Carsten Dominik

In memory of Giordano Bruno
1548 – 1600

Zusammenfassung

Seit den Anfängen der modernen Astronomie wurde über die Frage spekuliert, ob unser Planetensystem im Universum eine Sonderrolle einnimmt. In den vergangenen zwei Jahrzehnten gelang Astronomen die Entdeckung hunderter sog. Exo-Planeten, die um fremde Sterne kreisen. Parallel dazu geriet die Frage, auf welche Weise Planeten entstehen, in den Fokus. Auch wenn Astrophysiker in den letzten Jahren einer Antwort deutlich näher gekommen sind und sich die groben Umrisse des Planetenentstehungsprozesses klar abzeichnen, sind noch immer viele Detailfragen offen.

Als gesichert gilt, dass es ausgehend vom Kollaps einer interstellaren Molekülwolke zur Bildung einer sog. protoplanetaren Scheibe kommt. Diese besteht aus Gas, das um den in ihrem Zentrum entstandenen jungen Stern rotiert. In diese Gasscheibe sind mikroskopische Staub- und Eisteilchen eingebettet, die sich im Laufe der Zeit zu größeren, hochporösen Aggregaten verklumpen. Mit zunehmender Größe der Kollisionspartner wächst die Kollisionsgeschwindigkeit, was zur Kompaktifizierung der Aggregate führt. Kompakte Aggregate können voneinander abprallen und hohe Kollisionsgeschwindigkeiten führen zu Fragmentation; beide Effekte wirken einem weiteren Anwachsen entgegen. Erst ab einer Größe von ungefähr einem Kilometer reicht die Masse der Staub- und Eisbrocken aus, damit ihre Gravitation den weiteren Wachstumsprozess bis zum "ausgewachsenen" Planeten bestimmen kann.

Ziel dieser Dissertation ist es, den Wachstumsprozess von Mikrometergroßen Staubkörnern zu makroskopischen Aggregaten mit Hilfe von Computersimulationen genauer zu untersuchen. Im Rahmen eines Molekulardynamik-Ansatzes wird ein solches Aggregat aus bis zu einigen hunderttausend mikroskopischen, kugelförmigen Teilchen zusammengesetzt, die bei Kontakt miteinander wechselwirken. Im Rahmen dieser Promotion wurde zunächst für Staub das Wechselwirkungsmodell mit Hilfe geeigneter Laborexperimente kalibriert. Danach konnte das mechanische Verhalten poröser Staubaggregate untersucht werden und hierbei insbesondere die Kompressions-, Zug- und Scherfestigkeit bestimmt werden. Die genaue Kenntnis dieser Größen ist von zentraler Bedeutung um das Kollisionsverhalten makroskopischer Staubbrocken zu simulieren.

Außerdem wurde detailliert untersucht, wie sich die mikroskopische Struktur auf das Kollisionsverhalten auswirkt. Hierbei war von besonderem Interesse, unter welchen Bedingungen Aggregate voneinander abprallen und in welchem Geschwindigkeitsbereich der Übergang zu Fragmentation stattfindet. Der letzte Teil dieser Dissertation behandelte die Frage, wie stark verschiedene Arten von Staubaggregaten durch den Einschlag winziger Projektile erodiert werden.

Contents

1	Introduction	9
2	Work in context	17
2.1	Connections to SPH simulations	17
2.2	Connections to laboratory experiments	18
2.3	Connections to theoretical studies	19
3	Publications	21
3.1	Seizinger, Speith & Kley, 2012	23
3.2	Schräpler, Blum, Seizinger & Kley, 2012	35
3.3	Seizinger & Kley, 2013	45
3.4	Seizinger, Speith & Kley, 2013	55
3.5	Seizinger, Krijt & Kley, 2013	65
4	Summary & Outlook	73
4.1	Implications for the interaction model	73
4.2	Implications for MD simulations	73
4.3	Implications for SPH simulations	74
4.4	Implications for the growth of larger bodies	75
4.5	Outlook	75
5	Acknowledgements	77
	Bibliography	79

1 Introduction

Most people raising their heads and glancing at the sky on a clear and cloudless night, will be awestruck by the myriad of small, gleaming dots. From the very beginning of its existence, mankind has speculated about the nature of this phenomenon. Thanks to the efforts of countless astronomers and scientists our current knowledge has surpassed even the wildest dreams and expectations of scholars pondering the nature of the universe just a few centuries earlier.

Yet, for a moment let us adopt the perspective of a hypothetical, extraterrestrial observer, living on a planet similar to ours only a few hundred light years away. Looking at our solar system through one of their most powerful telescopes he would see nothing but a tiny spot of light being emitted from our sun. The vast majority of fascinating objects in our solar system would be invisible; hidden in the dark. Planets, moons, asteroids, volcanoes, weather phenomena, and, most importantly, life in all its manifold forms.

The hunt for extrasolar planets

As recently as 1995, the swiss astrophysicists Michel Mayor and Didier Queloz announced the detection of the first extrasolar planet that orbits 51 Pegasi, a star similar to our sun ([Mayor and Queloz, 1995](#)). However, the exoplanet has not been observed directly with a powerful telescope. Instead, its existence has been inferred from its gravitational interaction with 51 Pegasi. While orbiting the central star, both the planet and the star move around their common center of mass. An external observer can detect this motion from the periodic red and blue shift of the stellar spectral lines caused by the Doppler effect (see left panel of Fig. 1.1). Measuring the time variability of the red/blue shift, the orbital period can be determined (see right panel of Fig. 1.1). The mass of the star can be calculated from its luminosity and color. Applying Kepler's third law the semi-major axis and the mass of the planet can be calculated from the orbital period and the mass of the central star.

Since then several other methods to detect extrasolar planets have been developed. The most important one is the so-called "transit method". When a planet transits the central star, one can detect a slight diminution of the luminosity as the planet blocks out a tiny fraction of the light. The necessity of observing several transits constitutes a severe drawback of this method. When looking for Earth-like planets with an orbital period comparable to the Earth several years of observation time are required. Additionally, the observer must reside in the plane in which the planet orbits the star to be able to observe a transit. Interestingly, the transit method allows one to determine the size of the planet. In combination with its mass one can thus determine an average density and gain deeper insight regarding the composition of the planet.

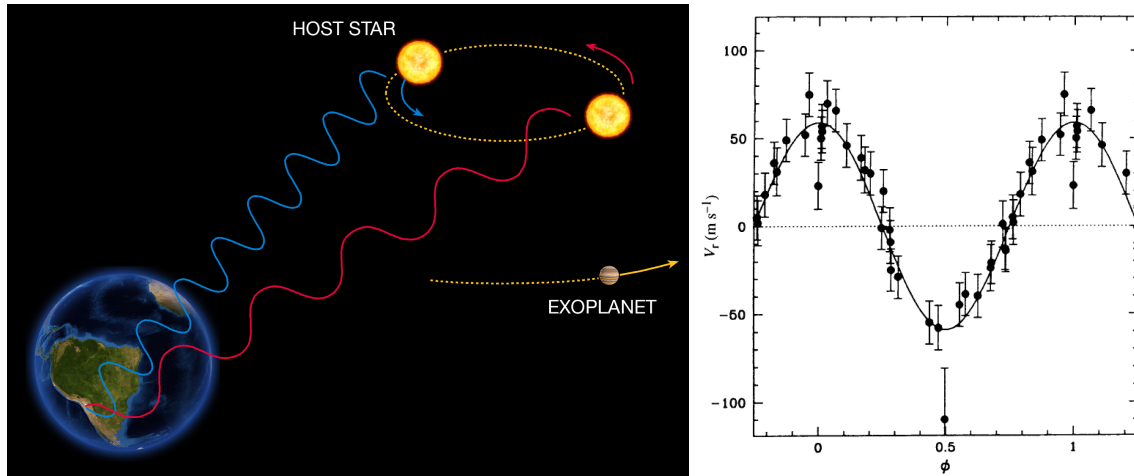


Figure 1.1: Detection of extrasolar planets by the radial velocity method. **Left:** Schematic view of the radial velocity method (Picture from ESO). **Right:** Orbital motion of 51 Pegasi determined by *Mayor and Queloz (1995)*.

Looking at the planets in our solar system clear patterns emerge. Small, rocky planets are found close to the sun, followed by the gas giants Jupiter and Saturn farther out. At even greater distances to the sun we find the ice giants Neptune and Uranus. Long before the discovery of extrasolar planets, scientists wondered whether these patterns will be found in any hypothetical extrasolar system. If we plot the mass of each known extrasolar planet with respect to its semi-major axis (see Fig. 1.2) we see at first glance that this is not the case. For instance, a fair amount of the exo-planets that have been discovered so far are very massive and close to their stars (so called “hot Jupiters”). Though one has to be very careful: the radial velocity method favors the detection of hot Jupiters; finding Earth-like planets is far less likely. Taking the sensitivity of the different methods into account, one can estimate the abundance of extrasolar planets. Depending on various assumptions, estimates on the number of terrestrial planets range from 10^9 to 10^{10} for the Milky Way alone (e.g. *Dressing and Charbonneau, 2013; Kopparapu, 2013*).

Refined methods boost our chances of detecting Earth-like planets. Kepler-10b was the first earth-sized planet detected by the Kepler mission (*Batalha et al., 2011*). However, owing to Kepler-10b’s proximity to its central star, its surface temperature is far too high to support life. To the present day, astronomers all around the world are eagerly searching for a “second earth”, a terrestrial planet of roughly one earth mass that orbits its central star at a distance that allows the existence of liquid water on its surface. Considering the vast number of extrasolar planets in the universe, it appears reasonable to speculate that the discovery of a second Earth is only a matter of time.

From cosmic dust bunnies. . .

Much to the regret of all planetary scientist, it is impossible to observe the birth of planets directly. The major impediment is the insurmountable distance between

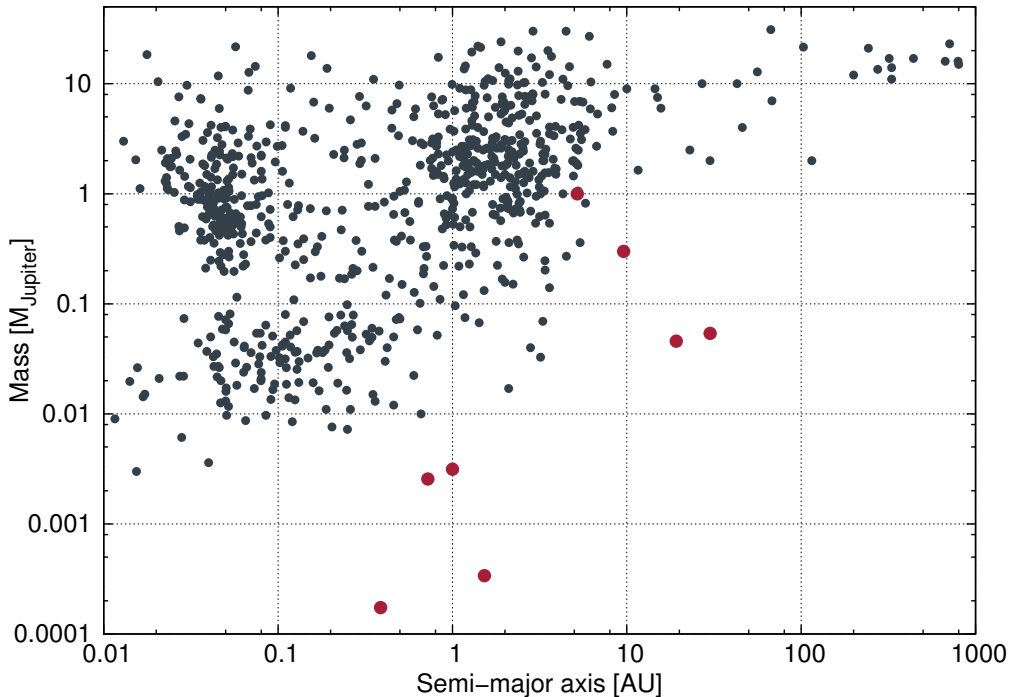


Figure 1.2: *The relationship between the mass and the semi-major axis of all extrasolar planets (anthracite) that have been discovered so far. For comparison the planets of our solar system (red) are depicted as well. Data taken from the Open Exoplanet Catalogue (Rein, 2012).*

us and the cosmic “delivery rooms” of planets, that even the largest telescopes cannot overcome. Additionally, the lifespan of a human being is much shorter than the timescale on which planet formation occurs. However, a clever combination of astronomical observations, laboratory experiments and computer simulations allows us to unravel the secrets of planet formation.

The birth of a new solar system begins with the collapse of a gigantic, interstellar cloud. Driven by the mutual gravitational attraction it shrinks to a fraction of its initial size. New stars form when the pressure and temperature in very dense clumps of matter becomes high enough for nuclear fusion (e.g. Shu et al., 1987). Owing to the conservation of angular momentum, the remaining matter begins to rotate around the center as the cloud collapses. The rotation causes the cloud to flatten out, which leads to the formation of an accretion disk around the young star (see Fig. 1.3), the so called protoplanetary disk.

An accretion disk has a diameter of roughly 100 AU. Observational data indicates that it contains a small amount (typically $\approx 1\%$) of sub-mm sized dust and ice grains (e.g. Williams and Cieza, 2011). Since these grains couple very well to the surrounding gas their relative velocities are small (e.g. Weidenschilling, 1977; Brauer et al., 2008). Collisions between grains will be hit & stick which leads to the formation of very fluffy, fractal aggregates (e.g. Kempf et al., 1999). This process is similar to the formation of dust bunnies under a bed. An example of such an aggregate generated within the scope of this thesis is depicted in Fig. 1.4.

As the aggregates grow larger, their motion increasingly decouples from the gas.

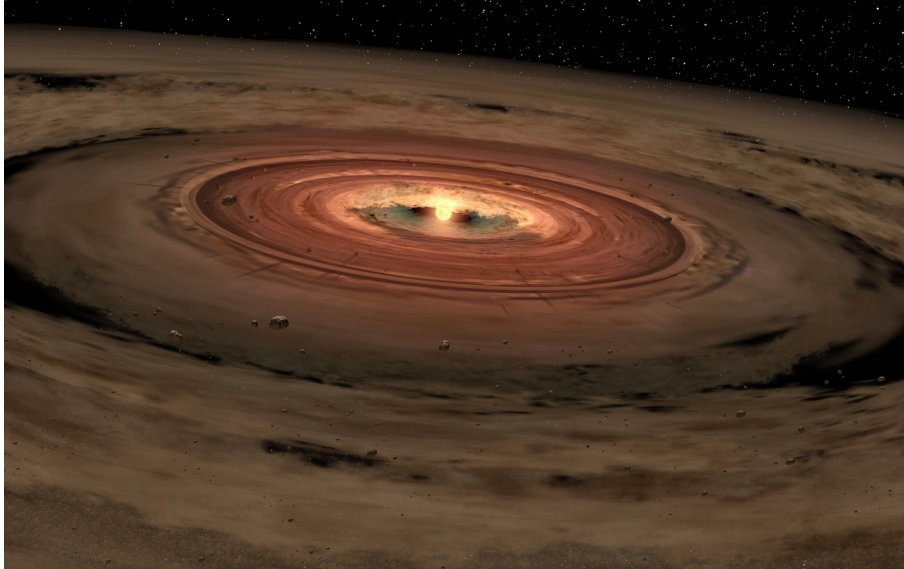


Figure 1.3: *Artist's impression of protoplanetary disk (Source: NASA)*

Aggregates of cm-size and above move on Keplerian orbits around the center. However, because of radial pressure support the gas rotates with sub-Keplerian speed. The velocity difference leads to friction which causes the aggregates to lose energy and spiral inwards. Unfortunately, it was shown that meter sized aggregates should fall into the star within just a few thousand years ([Weidenschilling, 1977](#)).

... to planetary embryos ...

Yet, the fast inward drift does not constitute the only impediment on the road to planet formation. As the motion of the aggregates decouples from that of the surrounding gas, their relative velocities increase as well. At some point, the collision velocities will be too high for hit & stick growth. Restructuring and fragmentation constitute the most prominent mechanisms of dissipating the excess kinetic impact energy. As a rule of thumb, it can be said that for porous aggregates colliding at intermediate velocities of the order of a meter per second restructuring and compression will be dominant, whereas fragmentation is the most likely outcome of high velocity collisions between compact targets. Compact targets colliding at intermediate velocities may also bounce off each other. However, it is not possible to draw sharp lines between those different regimes. Apart from the material the aggregates are composed of, a variety of factors such as the shape and internal structure of the aggregates, the collision velocity, and the impact parameter significantly influence the outcome of a collision. An extensive summary of laboratory experiments on collisions covering a wide parameter range is given by [Blum and Wurm \(2008\)](#) and [Güttler et al. \(2010\)](#).

Numerical simulations have been widely employed to study the collisional behavior of dust aggregates. Depending on the size of the aggregates, different methods have proven useful. For sub-mm sized aggregates, molecular dynamics simulations are a commonly used (e.g. [Dominik and Tielens, 1997](#); [Wada et al., 2007](#)). For larger



Figure 1.4: *Example of a fractal aggregate formed by low velocity collisions of micron sized dust grains. The whole aggregate consists of roughly 70000 individual grains.*

aggregates, one has to rely on a continuum approach such as smoothed particle hydrodynamics (SPH) (e.g. [Sirono, 2004](#); [Schäfer et al., 2007](#); [Geretshauser et al., 2011](#)).

Though the details are subjected to ongoing research it can be safely stated that fragmentation poses severe restrictions to the growth of larger bodies. Although laboratory experiments show collisional growth for cm-sized dust aggregates at impact velocities of up to 60 ms^{-1} ([Teiser and Wurm, 2009](#)), one can hardly imagine two massive, meter sized boulders to grow larger upon mutual collisions at a speed of 50 km/h.

Considering all these problems, it begs the question of why planetary systems form at all. Asteroids and other small bodies in the solar system, remnants from the time when the planets formed, provide us with valuable clues. Their craters bear witness to impacts of smaller objects (see [Fig. 1.5](#)). From space missions such as Galileo, we know that they are no solid bodies, but rather porous ([Wilson et al., 1999](#)). This might be the key to answer the question of planet formation, because porosity helps to dissipate excess kinetic impact energy. Thus, collisions of porous aggregates may result in net growth at impact velocities which would have shattered compact bodies to pieces.



Figure 1.5: *A mosaic of images of the asteroid Ida recorded by Galileo (Source: NASA/JPL).*

... and full grown planets

Bodies that have grown to kilometer size are referred to as planetesimals. They are sufficiently massive to allow gravity to play its part. Gravity assists the growth of larger bodies in several ways: first, gravitational focusing increases the collisional cross section, which boosts the collision rate. Secondly, self gravity enhances the strength of the planetesimals alleviating the mass loss from fragmentation. Third, it helps to reaccrete part of the ejecta generated by high velocity impacts. Thus, planetesimals may grow rapidly through mutual collisions (see Fig. 1.6).

At first, the planetesimals sweep up the smaller bodies in their vicinity. The more massive they become the faster they grow (e.g. [Greenberg et al., 1978](#); [Wetherill and Stewart, 1989](#)). When a few of them become massive enough, the oligarchic growth phase is entered ([Kokubo and Ida, 1998, 2002](#)). From now on, the most massive bodies, the oligarchs, will dominate the growth process and grow to about 0.1 Earth masses. In the final stage, oligarchs merge and sweep up or scatter out the remaining planetesimals. As a result, a limited number of Earth sized planets have formed. A more detailed summary of this stage of planet formation is given by [Goldreich et al. \(2004\)](#).

How gas giants form is still actively debated. There are two competing scenarios: In the core-accretion scenario proposed by [Pollack et al. \(1996\)](#), the formation of a gas giant starts with the formation of a massive core of roughly 10 Earth masses by the processes described above. Then, it is sufficiently massive to gravitationally accrete the surrounding gas. Initially, it grows in hydrostatic equilibrium. When a critical mass is exceeded, a phase of runaway gas accretion is entered. Growth stops when the supply of gas is exhausted. The lifetime of gas in the disk is roughly 10 Myrs ([Haisch et al., 2001](#)). However, it is not clear yet if the growth timescales of the core-accretion scenario satisfy this limit.

The gravitational instability scenario constitutes a different approach: gas giants form directly from clumps of matter collapsing due to their own gravity (e.g. [Boss, 1997](#)). This process is much faster than core-accretion. However, to become gravitationally unstable, disk have to be massive enough and must be able to cool efficiently

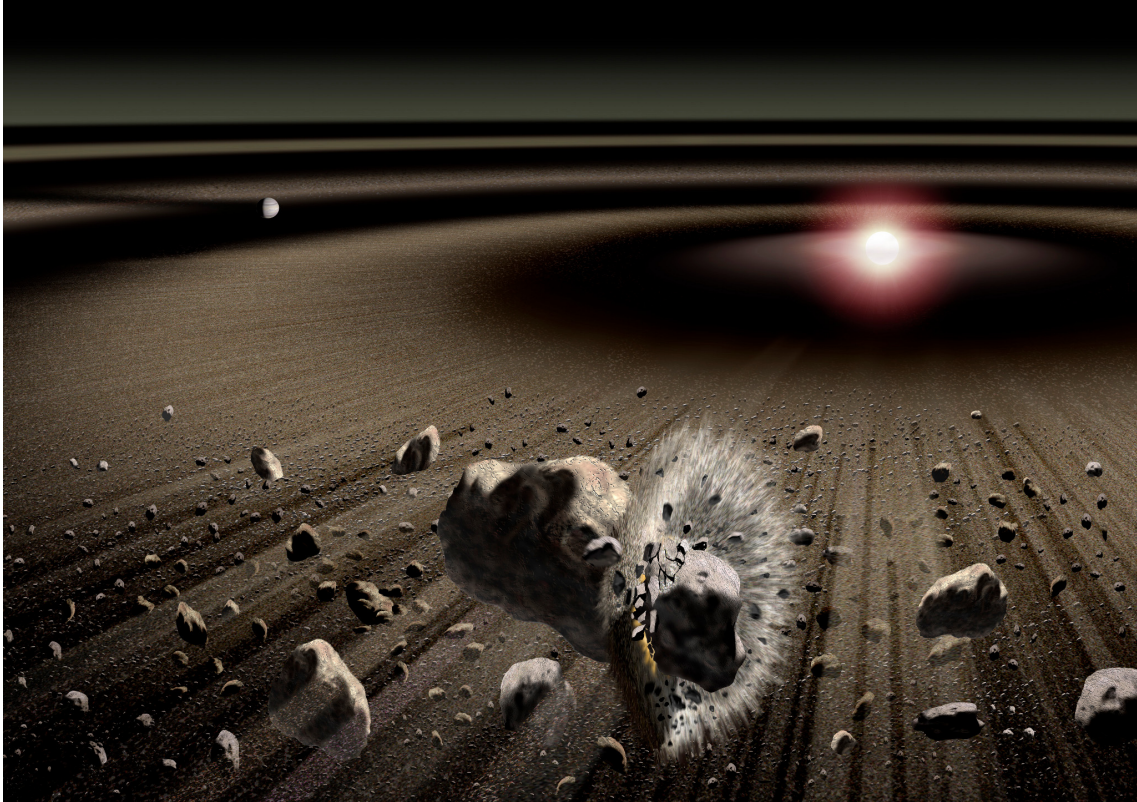


Figure 1.6: *Artist's impression of the collision of two larger boulders in the advanced stage of planet formation (Source: ISAS/JAXA).*

as well. Additionally, the formation of terrestrial planets cannot be explained by gravitational instability. Though [Goldreich and Ward \(1973\)](#) proposed that planetesimals could form similarly in a dense dust-sub-disk, it has later been shown that turbulence prevents the formation of a sufficiently dense dust sub-disk.

It is possible, however, that both core-accretion and gravitational instability could coexist. While it is believed that the terrestrial planets are formed by core-accretion, gravitational instability could explain the formation of gas giants at large distances from the central star where the growth timescales deduced from the core-accretion scenario exceed the lifetime of the disk.

As explained, many details regarding the growth from mm- to km-sized bodies are not fully understood yet. The aim of my thesis is to contribute to unraveling this stage of planet formation.

2 Work in context

The aim of this chapter is to describe in greater detail the connections between the content of this thesis and the current state of research. As already mentioned in Chapter 1, the growth from sub-mm to m-sized bodies is still not very well understood. The difficulty of unraveling this process originates from the complex interplay between the properties of the aggregates, the physics governing the collisions and the conditions in the surrounding disk. To this day, none of these three ingredients is entirely understood. However, in a hypothetical “master experiment of planetesimal formation” all three aspects must be put together.

In the scope of this thesis, a molecular dynamics (MD) approach is employed to address different open questions regarding the aggregate growth in protoplanetary disks. It features a detailed micro-mechanical interaction model that divides the interaction of two micron-sized spherical into four different types (see Fig. 2.1). The corresponding equations that describe these interaction types have been derived analytically (Johnson et al., 1971; Dominik and Tielens, 1995, 1996).

Much of the numerical approach is based on the pioneering work by Dominik and Tielens (1997). Later on, it was shown that except for one minor modification the same equations can be derived from corresponding potentials (Wada et al., 2007). This brings the advantage of being able to track the energy dissipation. For a more detailed description of the numerical approach the author refers to Seizinger et al. (2012) (see Sect. 3.1 of this thesis).

The main drawback of the molecular dynamics approach is the huge number of particles it requires to model larger aggregates. The computational cost renders the simulation of macroscopic aggregates impossible. To mitigate this problem the author developed a version that executes the numerical simulation on a graphics card (GPU). It exploits the massively parallel computing power provided by modern day GPUs. Compared to the single core CPU version it runs around 25 to 30 times faster. This allows to simulate collisions of aggregates composed of up to 10^6 particles within a reasonable amount of time.

2.1 Connections to SPH simulations

As briefly mentioned in Chapter 1, different size regimes require different numerical approaches. For bodies in the cm- to km-size regime smoothed particle hydrodynamics (SPH) simulations are often employed (e.g. Sirono, 2004; Schäfer et al., 2007; Geretschauser et al., 2011). However, the outcome of SPH simulations depends heavily on the assumed material parameters (Schäfer et al., 2007). Especially, it is important to know the relation between the compressive, tensile, and shear strength and the porosity of the material.

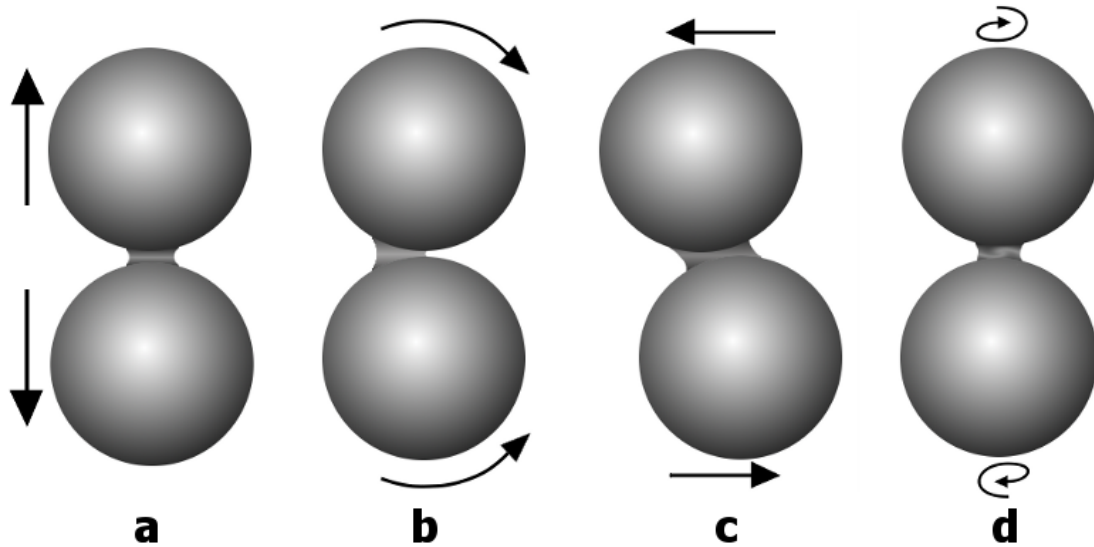


Figure 2.1: *The four types of particle interaction: Compression/Adhesion (a), Rolling (b), Sliding (c), and Twisting (d).*

To provide some of the required material parameters [Güttler et al. \(2009\)](#) measured the compressive strength relation in laboratory experiments and applied the results to SPH simulations. They suspected that there is a difference between slow (from now on referred to as quasi-static) and fast (from now on referred to as dynamic) compaction. However, laboratory experiments could only probe the static compaction regime. Based on this work, [Geretschauser et al. \(2010\)](#) conceived of two additional experiments to fully calibrate an SPH model that is capable of simulating silicate aggregates. While the compressive and tensile strength have been determined in laboratory experiments ([Blum and Schräpler, 2004](#); [Blum et al., 2006](#); [Güttler et al., 2009](#)), it is difficult to do the same for the shear strength.

So far, [Paszun and Dominik \(2008\)](#) performed numerical compression simulations that could reproduce earlier laboratory experiments by [Blum and Schräpler \(2004\)](#). However, their samples had been composed of as little as 300 monomers and it is questionable whether this number suffices to reach the continuum limit. Additionally, they were lacking the appropriate boundary conditions to model the setup of [Güttler et al. \(2009\)](#) which is more suitable for calibration purposes.

Thus, one part of this thesis was to perform simulations with a significantly larger number of monomers and appropriate boundary conditions. The aim was to determine the compressive, tensile, and shear strength as well as to study the difference between static and dynamic compaction with ab-initio numerical simulations.

2.2 Connections to laboratory experiments

Throughout the last years, the size regime between millimeters and decimeters has been explored in laboratory experiments. Though mimicking the conditions in protoplanetary disk proves difficult. Especially zero- (or at least micro-) gravity for an longer period of time is hard to achieve. For this reason some experiments have

been performed in drop-towers, parabolic flights, rockets, and even in space itself (Blum et al., 2000).

Performing experiments with porous aggregates similar to those of the first growth phase is further complicated by their low compressive and tensile strength (Blum and Schräpler, 2004; Güttler et al., 2009). It is very difficult to handle these aggregates without changing their structure or destroying them. Assessing the outcome of collisions on a microscopic scale requires expensive devices as well hard work. Very low or high impact velocities are difficult to achieve as well.

Nevertheless, laboratory experiments are worth the trouble. As experimental physicists conceived of ways to overcome those impediments, laboratory experiments provide theoretical models with invaluable input. Not only does the outcome of collisions experiments lay the foundations for theoretical studies on dust growth but they are crucial to calibrate numerical simulations. The latter is especially important within the context of my thesis and will be explained in greater detail in Sect. 2.1. So far, collisions experiments have been performed using a wide range of sizes, densities, impact velocities, etc. An overview is given by Blum and Wurm (2008) and Güttler et al. (2010).

In various laboratory experiments it was observed that mm- to cm-sized aggregates bounce off each other when colliding at intermediate velocities (e.g. Weidling et al., 2009; Heißelmann et al., 2010; Weidling et al., 2012; Jankowski et al., 2012). Remarkably, bouncing is observed for aggregates with relatively low volume filling factors of around 0.3. While similar behavior can be observed in SPH simulations (Geretschauser et al., 2010, e.g.), this does not apply to molecular dynamics (MD) simulations. In MD simulations, collisions result in bouncing only if the aggregates are considerably more compact (Wada et al., 2011). However, the aggregates used in the work of Wada et al. (2011) featured an artificial structure such as hexagonal close packing (HPC). Owing to the computational cost, the number of monomers their aggregates were composed of was limited to a few thousand. Exploiting the massive computing power provided by GPUs it is one part of this thesis to study the bouncing behavior of considerably larger aggregates with a more realistic internal structure.

2.3 Connections to theoretical studies

Unfortunately, it is impossible to watch the growth from micron-sized grains to kilometer-sized bodies in a laboratory experiment. However, the growth process can be modeled with computer simulations. The basic idea is to follow the collisional evolution of aggregates that feature properties such as the mass, density, or structure. Individual collisions are not resolved but their outcome is typically specified by recipes obtained from laboratory experiments or numerical simulations. The growth process can be modeled using the so called Smoluchowski equation (Smoluchowski, 1916). It requires a collision kernel that describes the outcome of a collision between two particles of different properties. For simple collision kernels such as perfect sticking it can be solved analytically.

For more realistic assumptions the Smoluchowski equation must be solved numerically. If only the mass of the particles is taken into account this can be done

with a grid code (e.g. [Birnstiel et al., 2010](#); [Windmark et al., 2012](#)). If the particles possess additional properties such as porosity or charge the computational costs of grid codes become a bottleneck. Alternatively, a Monte Carlo approach may be employed [Ormel et al. \(e.g. 2007\)](#). Using a Monte Carlo approach [Zsom and Dullemond \(2008\)](#) follow the collisional evolution of a swarm of representative particles. Their method was later used in a variety of works (e.g. [Zsom et al., 2010, 2011](#); [Drażkowska et al., 2013](#)).

Using the appropriate collision kernel is crucial for the outcome of the simulations. The collision kernels employed in the simulations have been based on the extrapolation of laboratory results. However, not all velocity or size regimes may be covered with laboratory experiments. Likewise, the problem of how much larger bodies suffer from erosion when they are bombarded with tiny but fast projectiles has not been quantified very well yet. Thus, numerical simulations may provide valuable insight into the erosion process and help to improve simulations of the growth process.

As mentioned in Sect 2.2, bouncing has not been well understood yet. Simulations show that the growth process could stall if macroscopic aggregates bounce off each other frequently ([Zsom et al., 2010](#)). Recently, several ways to overcome the so called “bouncing barrier” have been proposed ([Windmark et al., 2012](#); [Garaud et al., 2013](#)). Refining our understanding of the bouncing process is necessary to correctly estimate its influence on the growth of larger bodies.

3 Publications

In this chapter all publications that have been written in the context of this thesis are presented. All papers have been published in *Astronomy & Astrophysics* or the *Astrophysical Journal*.

In [Seizinger et al. \(2012\)](#), the micro-mechanical interaction model has been calibrated using laboratory experiments about the static compaction of porous dust aggregates. For this purpose suitable boundary conditions have been developed. After calibration, the difference between static and dynamic compression was studied. Based on this work, the tensile and shear strength has been determined in [Seizinger et al. \(2013b\)](#).

Meanwhile, in close connection to laboratory experiments the bouncing behavior was studied ([Schräpler et al., 2012](#)). This work sparked a broader exploration of the conditions required for bouncing ([Seizinger and Kley, 2013](#)). Within this work different methods of generating sample aggregates such as ballistic aggregation and migration were examined.

Recently, the interaction model has been extended by a new visco-elastic damping mechanism. After successfully calibrating the strength of the damping force, the erosion of larger dust aggregates has been studied ([Seizinger et al., 2013a](#)).

Compression behavior of porous dust agglomerates

A. Seizinger¹, R. Speith², and W. Kley¹

¹ Institut für Astronomie und Astrophysik, Eberhard Karls Universität Tübingen, Auf der Morgenstelle 10, 72076 Tübingen, Germany
e-mail: alexs@tat.physik.uni-tuebingen.de

² Physikalisches Institut, Eberhard Karls Universität Tübingen, Auf der Morgenstelle 14, 72076 Tübingen, Germany

Received 20 January 2012 / Accepted 11 March 2012

ABSTRACT

Context. The early planetesimal growth proceeds through a sequence of sticking collisions of dust agglomerates. Very uncertain is still the relative velocity regime in which growth rather than destruction can take place. The outcome of a collision depends on the bulk properties of the porous dust agglomerates.

Aims. Continuum models of dust agglomerates require a set of material parameters that are often difficult to obtain from laboratory experiments. Here, we aim at determining those parameters from ab initio molecular dynamics simulations. Our goal is to improve on the existing model that describe the interaction of individual monomers.

Methods. We use a molecular dynamics approach featuring a detailed micro-physical model of the interaction of spherical grains. The model includes normal forces, rolling, twisting and sliding between the dust grains. We present a new treatment of wall-particle interaction that allows us to perform customized simulations that directly correspond to laboratory experiments.

Results. We find that the existing interaction model by Dominik & Tielens leads to a too soft compressive strength behavior for uni- and omni-directional compression. Upon making the rolling and sliding coefficients stiffer we find excellent agreement in both cases. Additionally, we find that the compressive strength curve depends on the velocity with which the sample is compressed.

Conclusions. The modified interaction strengths between two individual dust grains will lead to a different behavior of the whole dust agglomerate. This will influence the sticking probabilities and hence the growth of planetesimals. The new parameter set might possibly lead to an enhanced sticking as more energy can be stored in the system before breakup.

Key words. planets and satellites: formation – methods: numerical – protoplanetary disks

1. Introduction

Unraveling the question of planetesimal formation is a crucial issue for the core accretion model of planet formation proposed by Pollack et al. (1996). To this day it remains unclear how dust and ice particles can grow several orders in magnitude from micron to kilometer sized objects. In the beginning micron sized dust grains (further referred to also as monomers or particles) may grow by low velocity, hit-and-stick collisions resulting in highly porous fractal aggregates (Kempf et al. 1999; Blum et al. 2000). As the aggregates grow larger their motion increasingly decouples from the surrounding gas leading to higher collision velocities (Weidenschilling 1977). With increasing impact energy colliding aggregates get compacted (Blum & Wurm 2000; Suyama et al. 2008; Wada et al. 2008; Paszun & Dominik 2009). At some point relative velocities become large enough that fragmentation is supposed to set in (e.g. Blum & Wurm 2008), which may limit the collisional growth of aggregates. Apart from fragmentation, radial drift and bouncing (e.g. Langkowski et al. 2008; Weidling et al. 2009; Güttler et al. 2010) may hamper the growth of planetesimals (Zsom et al. 2010). Despite these obstacles, experimental evidence indicates possible growth in high speed collisions (a few 10 m s^{-1}) through sticking and reaccretion of ejecta (Wurm et al. 2005; Teiser & Wurm 2009) or the sweep-up of smaller particles (Windmark et al. 2012). To understand the possible growth regimes requires material properties and simulations beyond the current data base.

In the context of planetesimal formation, collisions of micron sized aggregates have been studied theoretically using a

molecular dynamics approach (e.g. Dominik & Tielens 1997; Wada et al. 2007). Here, the motions of all grains that make up the aggregate are followed individually, considering suitable interaction forces. However, billions of such grains would be necessary to model meter-sized objects. For computational reasons it is therefore necessary in such cases to use continuum models to simulate collisions between macroscopic aggregates. Smooth Particle Hydrodynamics (SPH) constitutes such an approach (Sirono 2004; Schäfer et al. 2007; Geretshauser et al. 2010). However, the outcome of such simulations depends strongly on the underlying porosity model (Güttler et al. 2009). To simulate collisions of large dust boulders with SPH, several parameters describing the behavior of the material such as the compressive-, tensile-, and shear-strength must be known in advance.

To this day, only few attempts have been made to measure the required material parameter of porous dust aggregates in laboratory experiments. Blum & Schräpler (2004) studied the case of unidirectional compression, where a sample aggregate is compacted between two plates. While the bottom plate was fixed a certain load was applied to the top plate. To calculate the pressure the cross-section of the compressed aggregate had to be determined. Their samples were produced by random ballistic deposition (RBD) and featured an initial filling factor of 0.15. The maximum filling factor they could reach was limited to approximately 0.33 as grains began to flow outwards as the pressure in the center increased.

Later on, Güttler et al. (2009) used a similar approach to study the omnidirectional compression. Their sample was put

into a solid box and the load was applied by a movable piston on the top (see Fig. 3). As the grains could not escape the box they reached a significantly higher filling factor of roughly 0.58 upon compression. One advantage of this approach lies in the elimination of any uncertainty in the determination of the filling factor since the volume currently occupied by the sample is unambiguous.

The compressive strength of porous dust aggregates was determined numerically by [Paszun & Dominik \(2008\)](#) using a molecular dynamics approach based on an interaction model by [Dominik & Tielens \(1995, 1996\)](#). Yet, they only modeled the unidirectional compression and their simulations were limited to very few particles (≈ 300). Using similar material and model parameters the model has been applied to explore the growth regimes of dust agglomerates under protoplanetary conditions ([Suyama et al. 2008](#); [Wada et al. 2009, 2011](#); [Ormel et al. 2009](#)).

In this work we step back again and present a method to obtain the continuum material parameter of porous particle agglomerates, in particular the compressive strength curve, from ab initio simulations using a molecular dynamics approach. Our approach is based on the model by [Dominik & Tielens \(1995, 1996\)](#) using extensions by [Wada et al. \(2007\)](#). To test the applicability of the model we perform customized simulations of both, omni- and unidirectional compression, with a much greater number of particles on the order of 10^4 . As we will see, modifications of the model are required to properly reproduce the experimental results from [Güttler et al. \(2009\)](#). Having calibrated our model to the case of the slow compression as measured by [Güttler et al. \(2009\)](#) we will subsequently present new results on how the compressive behavior changes with increasing compression speed.

First, we briefly summarize the underlying physical model and present our extensions in Sect. 2. Our numerical setup is explained in Sect. 3. In Sect. 5, we first describe the calibration of our model. Afterwards, we present our results of studying the dynamic compression and provide simple analytical approximations describing the dependence of the compressive strength on the compression speed.

2. Interaction model

The agglomerates used in our simulations are composed of spherical monomers of equal size. To describe the interaction between individual monomers we adopt the physical model that has been presented by [Dominik & Tielens \(1997\)](#). In this model elastic grains may establish adhesive contacts when touching each other. Upon deformation of these contacts kinetic energy is dissipated. The forces and torques acting upon the monomers can be derived from corresponding potentials ([Wada et al. 2007](#)).

2.1. Particle-particle interaction

In [Dominik & Tielens \(1997\)](#) the interaction between two spherical particles is divided into four types (see Fig. 1):

1. compression/adhesion;
2. rolling;
3. sliding;
4. twisting.

In accordance with [Wada et al. \(2007\)](#) the following notation will be used in this work: r_i denotes the radius of a monomer i , γ_i the surface energy per area, E_i the Young's modulus, ν_i the

Table 1. Material parameters.

Physical property	Silicate
Particle radius r (in μm)	0.6
Density ρ (in g cm^{-3})	2.65
Surface energy γ (in mJ m^{-2})	20
Young's modulus E (in GPa)	54
Poisson number ν	0.17
Critical rolling length ξ_{crit} (in nm)	2

Poisson's ratio, and G_i the shear modulus. Furthermore, the reduced radius R is given by

$$R_{i,j} = \frac{r_i r_j}{r_i + r_j}$$

and

$$E_{i,j}^* = \left(\frac{1 - \nu_i^2}{E_i} + \frac{1 - \nu_j^2}{E_j} \right)^{-1},$$

$$G_{i,j}^* = \left(\frac{2 - \nu_i^2}{G_i} + \frac{2 - \nu_j^2}{G_j} \right)^{-1}.$$

Note that for simplification all monomers in our simulations feature the same properties.

2.1.1. Material parameters

The basis of our simulations are the material parameters of silicate as summarized in Table 1. With the exception of the surface energy γ these values comply with [Paszun & Dominik \(2008\)](#), where they used $\gamma = 25 \text{ mJ/m}^2$. These parameters are also in reasonable agreement with experimental data as quoted by [Blum & Schräpler \(2004\)](#); [Güttler et al. \(2009\)](#). In this work we use a slightly lower value of $\gamma = 20 \text{ mJ/m}^2$ which agrees with recent measurements of [Gundlach et al. \(2011\)](#).

2.1.2. Compression/adhesion

The particle interaction in the normal direction has been developed by [Johnson et al. \(1971\)](#) (often referred to as JKR theory). They extend the Hertzian theory by taking adhesion due to surface forces into account.

To very briefly summarize their model let us first note that the compression length δ of two monomers, which are in contact with each other and located at \mathbf{x}_1 and \mathbf{x}_2 , is defined by

$$\delta = r_1 + r_2 - \|\mathbf{x}_1 - \mathbf{x}_2\|, \quad (1)$$

where $\|\mathbf{u}\|$ denotes the norm of the vector \mathbf{u} . The radius a of the corresponding contact area can be obtained by

$$\frac{\delta}{\delta_0} = 3 \left(\frac{a}{a_0} \right)^2 - 2 \left(\frac{a}{a_0} \right)^{1/2}, \quad (2)$$

where δ_0 and a_0 denote the equilibrium compression length and contact radius, respectively, where the repulsive and attractive normal forces are equal. It applies

$$\delta_0 = \frac{a_0^2}{3R},$$

$$a_0 = \left(\frac{9\pi\gamma R^2}{E^*} \right)^{1/3}.$$

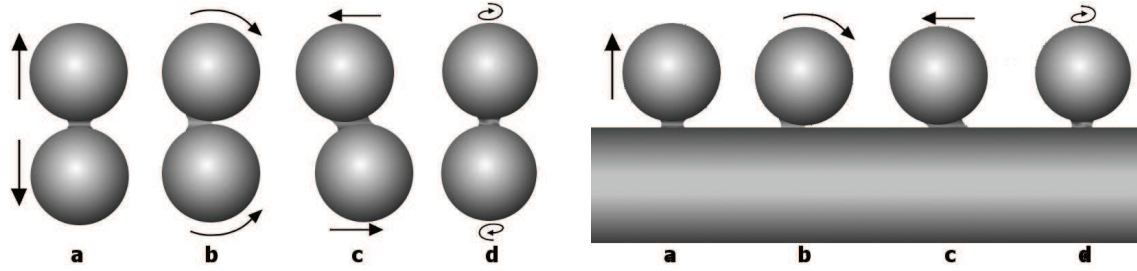


Fig. 1. The four types of particle interaction: compression/adhesion **a**), Rolling **b**), Sliding **c**), and Twisting **d**). The *left panel* depicts particle-particle interactions while on the *right* the corresponding particle-wall version is displayed.

The force acting upon the monomers is

$$F = 4F_c \left[\left(\frac{a}{a_0} \right)^3 - \left(\frac{a}{a_0} \right)^{3/2} \right], \quad (3)$$

where $F_c = 3\pi\gamma R$ is the force needed to break the contact.

A new contact is established if two freely moving particles touch each other, which means $\delta = 0$. However, once a contact has formed it will not break until the compression length exceeds a certain threshold $\delta_c = (9/16)^{1/3} \delta_0$. Thus, contacts may be stretched out a little bit before they finally break.

2.1.3. Sticking velocity

On contact formation or breaking there is a jump in the potential corresponding to the JKR force (see [Wada et al. 2007](#)), which reflects the dissipation of kinetic energy upon contact formation or breaking. [Chokshi et al. \(1993\)](#) proposed that this energy dissipation is caused by the excitation of elastic waves. From this energy dissipation one can calculate the maximum velocity v_{stick} at which particles stick on head-on impacts in JKR-theory

$$v_{\text{stick}} = 1.07 \frac{\gamma^{5/6}}{E^{*1/3} R^{5/6} \rho^{1/2}}. \quad (4)$$

For micron-sized SiO_2 grains, we obtain velocities on the order of 0.1 m s^{-1} . However, laboratory experiments by [Poppe et al. \(2000\)](#) yield a significantly higher sticking velocity of roughly 1.2 m s^{-1} for similar sized particles. To overcome this discrepancy, [Paszun & Dominik \(2008\)](#) introduced another damping mechanism that dissipated additional kinetic energy upon the contact creation and thus increased the sticking velocity to match the laboratory experiments.

Since the sticking velocity has to be increased by approximately one order of magnitude a significant amount of kinetic energy has to be dissipated aside from JKR-theory. Dissipating the kinetic impact energy all at once leads to a significant change of the relative velocity between the colliding particles. As they may be in contact with other particles as well, significantly modifying the velocity of one particle during one integration step may introduce numerical hazards. For low collision velocities (the compression velocity used by [Paszun & Dominik 2008](#), was 0.05 m s^{-1}) the additional damping is low and therefore this problem does not arise. However, since in this work we also want to study the dynamic compression behavior at high velocities we choose a different approach to adjust the sticking velocity as explained in the next section.

2.1.4. Normal oscillations

The normal force may be both attractive or repulsive depending on the current compression length δ . When two particles come too close to each other they are repelled, whereas they get attracted to each other due to adhesive surface forces while the contact is stretched out. This leads to oscillations of two monomers in the normal direction of a contact (from now on referred to as normal oscillations). In reality, one would expect that these oscillations are eventually damped away. For instance [Brilliantov et al. \(2007\)](#) proposed a viscoelastic damping mechanism.

From a numerical point of view these normal oscillations constitute a major nuisance. Not only may they artificially heat up aggregates ([Paszun & Dominik 2008](#)) but most importantly they need to be properly resolved in time. For micron-sized SiO_2 grains the typical timescale of these oscillations is on the order of 10 ns. Therefore our integration timestep is limited to $\approx 0.1\text{--}0.3$ ns.

[Paszun & Dominik \(2008\)](#) tackle the problem of artificial heating by introducing an additional, weak damping mechanism which has hardly any influence on the sticking velocity but eventually damps away normal oscillations. In this work we follow a similar approach. As before we consider two monomers located at \mathbf{x}_1 and \mathbf{x}_2 that are in contact with each other. The contact normal \mathbf{n}_c is

$$\mathbf{n}_c = \frac{\mathbf{x}_1 - \mathbf{x}_2}{\|\mathbf{x}_1 - \mathbf{x}_2\|}. \quad (5)$$

The relative velocity v_{rel} in normal direction of the contact is then given by

$$v_{\text{rel}} = (\mathbf{v}_1 - \mathbf{v}_2) \cdot \mathbf{n}_c, \quad (6)$$

where $\mathbf{v}_1, \mathbf{v}_2$ denote the velocity of particle 1 and 2, respectively. The viscous damping force \mathbf{F}_{damp} is

$$\mathbf{F}_{\text{damp}} = -\kappa v_{\text{rel}} \mathbf{n}_c, \quad (7)$$

where κ is a damping constant determining the strength of the damping. We use $\kappa = 1 \times 10^{-6} \text{ g/s}$.

2.1.5. Rolling, sliding, and twisting

The forces and torques resulting from the tangential motion of the contact area have been formulated by [Dominik & Tielens \(1995, 1996\)](#). So called ‘‘contact pointers’’ ([Dominik & Nübold 2002](#)) provide a convenient way to track the evolution of the contact area. They are unit vectors that initially point from the center of the particle to the center of the contact area. Due to

the rotation of the particles their orientation changes over time (Dominik & Nübold 2002). Contact pointers are used to define the rolling, sliding, and twisting displacement which quantify how much rolling, sliding, or twisting of a contact has occurred.

Using these displacements, Wada et al. (2007) derived the forces and torques which agree with Dominik & Tielens (1995, 1996), from corresponding potentials. All three types of interaction remain elastically as long as the displacements do not exceed certain thresholds (from now on referred to as critical displacements).

Let \mathbf{n}_1 and \mathbf{n}_2 be the corresponding contact pointers describing the contact. The rolling displacement ξ , sliding displacement ζ , and twisting displacement ϕ are then defined by:

$$\xi = R(\mathbf{n}_1 + \mathbf{n}_2), \quad (8)$$

$$\zeta = r_1\mathbf{n}_1 - r_2\mathbf{n}_2 - (r_1\mathbf{n}_1 \cdot \mathbf{n}_c - r_2\mathbf{n}_2 \cdot \mathbf{n}_c)\mathbf{n}_c, \quad (9)$$

$$\phi = \mathbf{n}_c(t) \int_{t_0}^t (\omega_1(t') - \omega_2(t')) \cdot \mathbf{n}_c(t') dt', \quad (10)$$

where t_0 denotes the time when the contact has been established.

For the rolling motion, the forces \mathbf{F}_r and torques \mathbf{M}_r acting upon particle 1 due to being in contact with particle 2 are

$$\mathbf{F}_r = 0, \quad (11)$$

$$\mathbf{M}_r = -Rk_r\mathbf{n}_1 \times \xi. \quad (12)$$

For the sliding interaction, the forces and toques are given by

$$\mathbf{F}_s = -k_s \zeta \frac{(r_2\mathbf{n}_2 - r_1\mathbf{n}_1) \cdot \mathbf{n}_c}{\|\mathbf{x}_1 - \mathbf{x}_2\|}, \quad (13)$$

$$\mathbf{M}_s = -r_1k_s\mathbf{n}_1 \times \zeta. \quad (14)$$

And for the twisting interaction it applies

$$\mathbf{F}_t = 0, \quad (15)$$

$$\mathbf{M}_t = -k_t\phi. \quad (16)$$

The constants k_r , k_s , and k_t are given by

$$k_r = \frac{4F_c}{R}, \quad (17)$$

$$k_s = 8a_0G^*, \quad (18)$$

$$k_t = \frac{16}{3}Ga_0^3. \quad (19)$$

2.1.6. Inelastic interaction

As already mentioned before, inelastic motion sets in when the displacements exceed a critical displacement ξ_{crit} , ζ_{crit} , or ϕ_{crit} . Physically this corresponds to energy being dissipated upon relocation of the contact area. The critical sliding and twisting displacements have been derived theoretically (Dominik & Tielens 1996) as

$$\zeta_{\text{crit}} = \frac{2-\nu}{16\pi}a_0,$$

$$\phi_{\text{crit}} = \frac{1}{16\pi}.$$

The value of the critical rolling displacement ξ_{crit} is still debated. At first, Dominik & Tielens (1997) assumed ξ_{crit} close to inneratomic distances and chose $\xi_{\text{crit}} = 0.2$ nm. However, subsequent laboratory experiments by Heim et al. (1999) indicate a much higher value of $\xi_{\text{crit}} = 3.2$ nm for spherical SiO₂ grains of 1.9 μm in diameter. In this work we follow Paszun & Dominik (2008) and set $\xi_{\text{crit}} = 2$ nm for 1.2 μm sized grains.

When a displacement exceeds its critical value it will be restored to the elastic limit. If for instance the rolling displacement exceeds its critical value $\|\xi\| > \xi_{\text{crit}}$, the contact pointers will be corrected $\mathbf{n}_1 \rightarrow \mathbf{n}_1^c$, $\mathbf{n}_2 \rightarrow \mathbf{n}_2^c$ and thus $\xi \rightarrow \xi^c$ such that $\|\xi^c\| = \xi_{\text{crit}}$. This modification of the contact pointers reflects a change of the corresponding potential energy. Therefore, we can keep track of the amount of dissipated energy. For further details on how the inelastic motion is applied we refer to Wada et al. (2007).

2.2. Particle-Wall interaction

To study the compression of a sample aggregate it is necessary to constrain the motion of the monomers using suitable boundary conditions. In the corresponding experiments the sample has been put in a solid box with a movable piston on top (see Güttler et al. 2009, Fig. 2). In our simulations we model the experimental setup by putting the sample aggregate into a box of fixed walls. During the simulation the top wall is moving downwards with constant speed in order to compress the sample (see Fig. 2).

We assume that the monomers may interact with a wall in a similar way as they interact with other grains. In accordance with the particle-particle interaction we derive the corresponding forces and torques following the approach presented by Wada et al. (2007). For this purpose we assume that the wall can be described as a very huge particle in the limit $r_{\text{wall}} \rightarrow \infty$.

2.2.1. Compression

The force of the particle-wall interaction in normal direction is very similar to the case of the particle-particle interaction. The compression length δ is given by

$$\delta = r - d,$$

where r is the radius of the monomer and d denotes the distance between the surface of the wall and the center of the grain. Given a point \mathbf{p} located on the surface of the wall and the surface normal \mathbf{n}_w , we can easily obtain d by

$$d = |(\mathbf{x} - \mathbf{p}) \cdot \mathbf{n}_w|,$$

where \mathbf{x} denotes the position of the particle. The force in normal direction can then be calculated using Eq. (3). Note that here the reduced radius R is different to the case of particle-particle interaction. In the limit of $r_{\text{wall}} \rightarrow \infty$ the reduced radius R equals the radius r of a monomer:

$$R = \lim_{r_{\text{wall}} \rightarrow \infty} \frac{r r_{\text{wall}}}{r + r_{\text{wall}}} = r.$$

2.2.2. Rolling

Keeping in mind that $R = r$, the torque \mathbf{M}_r acting on the particle caused by rolling along the surface of the wall is given by

$$\mathbf{M}_r = k_{r,\text{wall}}r^2\mathbf{n}_1 \times \mathbf{n}_w, \quad (20)$$

where $k_{r,\text{wall}}$ is equivalent to the rolling constant k_r given in Eq. (17) taking the different reduced radius of the particle-wall interaction into account. \mathbf{n}_w denotes the surface normal of the wall. Note that it is important on which side of the wall the particle is located with respect to the direction of \mathbf{n}_w . In the simulation we must either ensure that the particles remain on the positively oriented side all the time or check on which side of

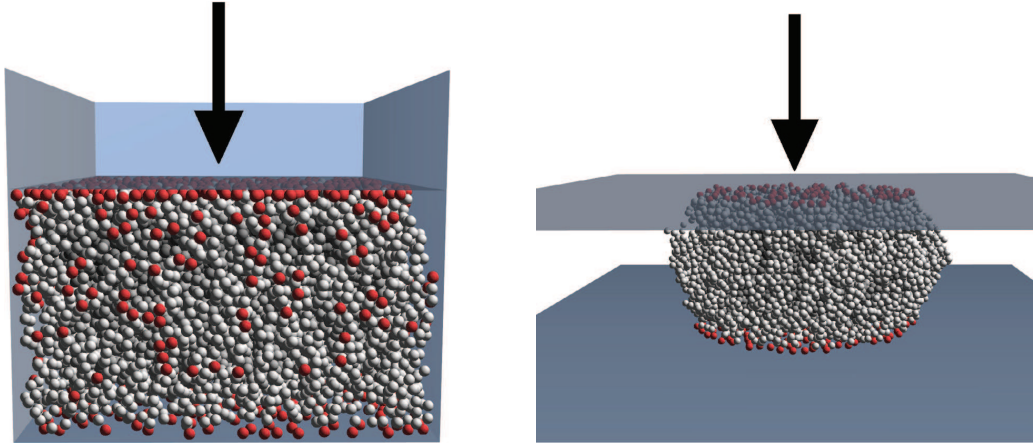


Fig. 2. Setup of the numerical simulations to obtain material parameter for porous dust agglomerates. *Left:* omnidirectional compression, while the top wall is moving downwards at constant speed, the sample is enclosed in a box with fixed walls on all sides. *Right:* unidirectional compression, as the sample is getting compressed between two walls, particles can leave the initial volume to the sides. Particles colored red are actually in contact with the walls.

the wall the particle is located and correct the sign of Eq. (20) if necessary.

To model the motion of a particle which is rolling inelastically over a wall we use a similar approach as for the inelastic particle-particle interaction. Taking $r_2 \rightarrow \infty$ into account, the correction of the contact pointers is then given by

$$\mathbf{n}_1^c = \mathbf{n}_1 - \frac{\alpha}{r} \Delta \boldsymbol{\xi}, \quad (21)$$

$$\mathbf{n}_2^c = \mathbf{n}_2 = \mathbf{n}_w, \quad (22)$$

where α is a correction factor derived in detail in Wada et al. (2007) and $\Delta \boldsymbol{\xi}$ is given by

$$\Delta \boldsymbol{\xi} = \boldsymbol{\xi} \left(1 - \frac{\xi_{\text{crit}}}{\|\boldsymbol{\xi}\|} \right). \quad (23)$$

The contact pointer \mathbf{n}_2 of the “wall particle” is equivalent to the normal vector \mathbf{n}_w of the wall and is not modified during the inelastic rolling motion.

2.2.3. Sliding

To describe the sliding motion of a particle on a wall it is not suitable to start with Eq. (9) and assume that $\mathbf{n}_c \rightarrow \mathbf{n}_w$ and $\mathbf{n}_2 \rightarrow \mathbf{n}_w$. Therefore we choose a different approach that takes into account how far the contact has slid from the location where it has initially formed.

Let \mathbf{p} denote the position, where the surface of the particle touched the wall when establishing the contact. For any later time, the center of the contact area is given by $\mathbf{x} + r\mathbf{n}_1$, where \mathbf{x} is the current position of the particle. We define

$$\boldsymbol{\zeta}_0 = \mathbf{x} + r\mathbf{n}_1 - \mathbf{p}.$$

The sliding displacement is then given by

$$\boldsymbol{\zeta} = \boldsymbol{\zeta}_0 - (\boldsymbol{\zeta}_0 \cdot \mathbf{n}_w) \mathbf{n}_w. \quad (24)$$

To model the inelastic wall sliding we modify the initial center of the contact area \mathbf{p} . If $\|\boldsymbol{\zeta}\| > \zeta_{\text{crit}}$, we apply the correction

$$\mathbf{p}^c = \mathbf{p} + \left(1 - \frac{\zeta_{\text{crit}}}{\|\boldsymbol{\zeta}\|} \right) \boldsymbol{\zeta}. \quad (25)$$

2.2.4. Twisting

The torque caused by the twisting motion is calculated in the same way as if two particles are in contact. Starting with the twisting displacement $\boldsymbol{\phi}$ given in Eq. (10) we obtain

$$\boldsymbol{\phi}_{\text{wall}} = \mathbf{n}_c \int_{t_0}^t (\boldsymbol{\omega}_1(t')) \cdot \mathbf{n}_c(t') dt', \quad (26)$$

under the assumption that the wall does not rotate. The torque is then given by

$$\mathbf{M}_{\text{t,wall}} = -k_{\text{t,wall}} \boldsymbol{\phi}_{\text{wall}}, \quad (27)$$

where $k_{\text{t,wall}} = k_t$. Here we assume that particles may twist elastically around the same angle for both the particle-particle and particle-wall interaction. According to test simulations where we measured the relative importance of the different wall interaction dissipation channels, inelastic wall twisting is of only minor importance.

3. Setup

In order to calibrate the model and to compare simulations in detail with experimental results we focus here on two different numerical experiments that follow closely the experimental setup. Specifically, we will deal with agglomerates enclosed in a box and aggregates confined between two plates as depicted in Fig. 2.

3.1. Sample generation

In accordance with the mentioned laboratory experiments by Blum & Schröpfer (2004); Güttler et al. (2009), our samples are produced by random ballistic deposition (RBD), which means that single grains are successively poured down on the existing aggregate impacting from the same direction. In order to prevent any restructuring upon impact the impact velocity of a monomer hitting the sample is kept very low. The resulting samples feature a filling factor ϕ between 0.12–0.15. Filling factors of 0.12–0.14 result from the fluffier surface and are therefore only observed

for small samples. As the size of the samples increases this surface effect becomes negligible and the filling factor converges to 0.15 which agrees well with the dust cakes used in the corresponding laboratory experiments and with numerical studies by [Watson et al. \(1997\)](#).

3.2. Measurements

3.2.1. Pressure

In the numerical (and laboratory) experiments a box-shaped sample is enclosed between walls that constrain the motion of the grains (see Fig. 2). Then, the top wall is being moved downwards at a constant speed until the filling factor exceeds a certain threshold ϕ_{crit} . Typically, ϕ_{crit} is set to 0.7. As the top wall is moving downwards the volume of the sample decreases and it is increasingly more compressed. The total force F_w acting upon the top wall is calculated by summarizing the forces F_i exerted on the wall by grains that are currently in contact with it, where only the component in normal direction n_w to the wall is taken into account

$$F_w = n_w \cdot \left(\sum_i F_i \right).$$

The pressure P is then given by

$$P = \frac{F_w}{A},$$

where A denotes the base size of the box.

If there are only a few particles in contact with the wall, F_w may change considerably from one integration step to the next due to the normal oscillations of the particle-wall contact (see Sect. 2.1.4). Since these vibrations occur on a timescale of nanoseconds whereas the compression timescale is typically orders of magnitudes higher, it is reasonable to average over several integration steps (covering a few normal particle oscillations) to reduce the noise in the pressure determination. Typically, we averaged over 100 integration steps in this work.

3.2.2. Filling factor

The volume filling factor ϕ is defined as

$$\phi = \frac{V_{\text{mat}}}{V_{\text{tot}}}, \quad (28)$$

where $V_{\text{mat}} = 4/3\pi r^3 N$ denotes the volume of N particles of radius r and V_{tot} is the volume that the aggregate currently occupies. Calculating the filling factor is trivial in the case of omnidirectional compression (see Fig. 2, left panel) as $V_{\text{tot}} = Ah$ for a box with base size A and current height h .

However, in the uni-directional case (Fig. 2, right panel) there are no side walls containing the aggregate, and particles will leave the initial volume. They flow to the sides as the top wall is moving downwards. This complicates the determination of V_{tot} in the numerical as well as experimental setup. In the following we assume that the volume the aggregate is currently occupying is given by its projected cross section A_{proj} and the current height h of the aggregate, which equals the distance between the top and the bottom wall. A_{proj} is obtained by projecting the aggregate in the plane of the top/bottom wall.

3.3. Previous work

A first attempt to determine the compressive strength numerically has been presented by [Paszun & Dominik \(2008\)](#). With the exception of the damping of the normal interaction (see Sects. 2.1.3 and 2.1.4) they used the same particle interaction model that we use here. However, instead of flat walls they used two huge particles with radii much bigger than the dust grains to model the boundary conditions. The sample was put between the “wall particles” and the upper particle was being moved downwards at constant speed while the force acting on this “wall particle” was stored for later analysis. Since the motion of the grains has only been constrained in the vertical direction, grains could dodge to the sides as the pressure increased. Thus, an increase of the initial cross section of the aggregate was observed during the compression that led to a significant uncertainty in the determination of the volume the aggregate occupied at a certain point of time. Since the number of monomers was also limited to very small numbers (≈ 300) it is questionable if the results hold in the continuum limit.

[Paszun & Dominik \(2008\)](#) confined themselves to the case of unidirectional compression. To our knowledge, the case of omnidirectional compression has not been simulated so far for this material. The compressive strength was only determined for a compression speed of 0.05 m s^{-1} . A possible dependency of the compression behavior on the speed of the compression has not been studied before.

4. Numerical method

To integrate the equations of motion we use a second order, symplectic Leap-Frog scheme. The main reason behind this choice lies in the fact that the forces and torques have to be determined only once during each integration step. Likewise, the evolution of the contact pointers and the twisting displacement (see Eq. (10)) is calculated with second order accuracy.

The timestep is limited by the oscillations in direction of the contact normal force (see Sect. 2.1.4) as well as the oscillations in the tangential plane of the contact caused by the sliding force. As already mentioned the normal oscillation period is on the order of 10 ns.

The period of the oscillations in the tangential plane can be obtained in the following way: [Wada et al. \(2007\)](#) derive the sliding force from the corresponding sliding potential U_s

$$U_s = \frac{1}{2} k_s \|\zeta\|^2. \quad (29)$$

We can get an estimate of the oscillation period T by

$$T = \frac{2\pi}{\omega} = 2\pi \sqrt{\frac{m}{k_s}}, \quad (30)$$

where ω denotes the corresponding angular frequency of the oscillation and m is the mass of a monomer. For the material parameters given in Table 1 we obtain $T = 12.8 \text{ ns}$. Applying the sliding modifier $m_s = 2.5$ (see Sect. 5.1) the tangential oscillation period decreases to $T = 7.83 \text{ ns}$, which limits our timestep to 0.3 ns.

5. Results

Calibration experiments using a continuum SPH-code indicate that the compressive strength of a porous dust aggregate depends on how fast the compaction takes place

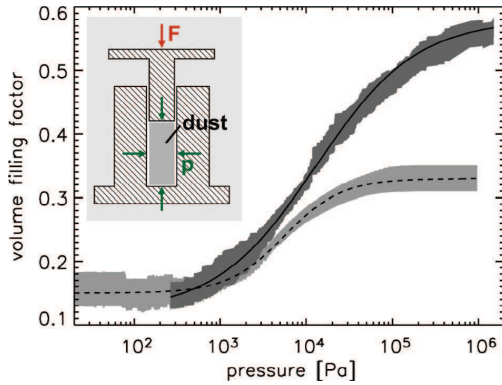


Fig. 3. The compressive strength (filling factor ϕ versus pressure p) as obtained from experiments. The dark shaded region with the solid line fit refer to the omnidirectional compression experiment performed by Güttler et al. (2009) whereas the light shaded region and the dashed line fit were obtained for unidirectional compression by Blum & Schröppler (2004). The small image on the top left depicts the experimental setup of the omni-directional compression experiment. (Figure taken from Güttler et al. 2009.)

(Güttler et al. 2009; Geretshauer et al. 2010). So far, in laboratory experiments the compressive strength could only be determined for a slow quasi-static compression process, where the compressed aggregate had been given sufficient time for relaxation (in the following referred to as static compression) (Güttler et al. 2009).

The static compression provides us with the possibility to check how well our model is able to describe the compression behavior of porous dust aggregates. In the first step we will therefore use the case of the omnidirectional static compression to calibrate our molecular dynamics model. Afterwards we will increase the speed of the top wall. At a sufficiently high speed the relaxation of the aggregate will not be possible any longer (from now on referred to as dynamic compression).

5.1. Calibration of our model

To model the quasi-static compression the speed v_{wall} at which the top wall is moving downwards should be as low as possible. As the time required to reach a certain filling factor is inversely proportional to v_{wall} , the runtime of the simulation constitutes a lower limit of v_{wall} . Paszun & Dominik (2008) considered $v_{\text{wall}} = 5$ cm/s to be low enough to model static compression. However, we observe that the curves still change when using even lower velocities (see Fig. 6 below). To model the case of static compression we set $v_{\text{wall}} = 1$ cm/s. To ensure it is a reasonable choice we checked lower velocities down to $v_{\text{wall}} = 0.2$ m s⁻¹ but observed only a tiny deviation of the resulting curves.

Depending on the number of particles we use, the diameter of our sample aggregates is roughly 40–60 μm which is about $\times 10^3$ times smaller than the samples used in the laboratory experiments. While the sample is getting compacted the particles on the edges of the sample must overcome the sliding resistance of the side wall. Owing to the small diameter of the sample this has a significant influence on the resulting force on the top wall. To mitigate this effect we reduce the strength of the rolling, sliding, and twisting interaction between particles and the side walls by a factor of 1000.

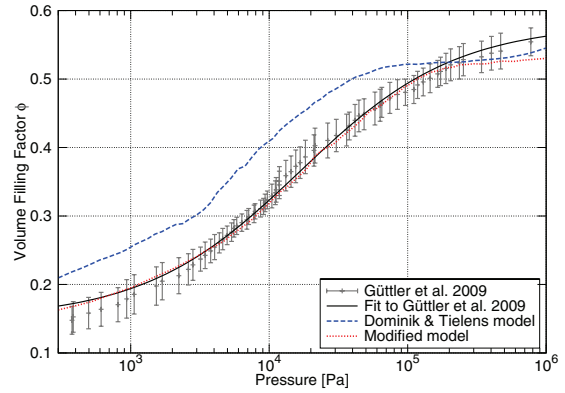


Fig. 4. Compressive strength for omnidirectional compression of cubical aggregates. The result of the unaltered interaction model is compared to our improved model. The black line represents a fit to experimental data obtained from Güttler et al. (2009).

The results of the corresponding laboratory experiment are shown in Fig. 3. The solid black curve is a good fit to the omnidirectional experimental data (see Fig. 4 and dark shaded area in Fig. 3) and is given by

$$\phi(P) = \phi_2 - \frac{\phi_2 - \phi_1}{\exp\left(\frac{\log_{10} P - \log_{10} p_m}{\Delta}\right) + 1} \quad (31)$$

Using $\phi_1 = 0.15$ and $\phi_2 = 0.58$ we obtain $p_m = 16.667$ kPa and $\Delta = 0.562$. The black curve shown in Fig. 4 depicts this fit.

The results of the unidirectional experiments, also displayed in Fig. 3, have been fitted by Blum & Schröppler (2004) using a similar curve with $\phi_1 = 0.15$, $\phi_2 = 0.33$, $p_m = 5.6$ kPa, and $\Delta = 0.33$.

5.2. Omnidirectional compression

5.2.1. Quasi-static case

In Fig. 4, we compare the experimental fitting curve to results from our simulations of box-shaped samples featuring approximately 11 000 particles and an edge length of about 40 μm . All curves have been obtained from averaging the results of six independent runs with samples having statistically equal bulk properties.

Obviously, simulations using the Dominik and Tielens model do not reproduce the experimental data very well. For low pressures the blue dashed curve in Fig. 4 lies significantly above the solid black one, i.e. applying the same pressure the sample has been compressed to a higher filling factor in the simulations than compared to the experiments. In order to make it harder to compress an aggregate we tried to increase the stiffness of the aggregates by modifying the particle interaction.

To our knowledge the equations describing the rolling and sliding interaction have not been experimentally tested yet, whereas the pull-off force of the normal interaction has been measured using atomic force microscopy (Heim et al. 1999). Thus, we vary the strength of the rolling and sliding interaction. For this purpose we simply multiply the constants k_r and k_s (see Eqs. (17) and (18)) with correction factors that we further refer to as rolling/sliding modifiers m_r and m_s . This constitutes a straightforward approach to increase the stiffness of monomer

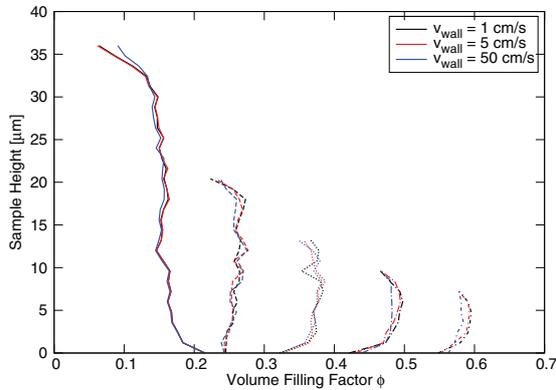


Fig. 5. Snapshots of the vertical profile of the aggregate's filling factor averaged horizontally. Shown are results at 5 evolutionary times using 3 different speeds. The left (solid) curves represent the initial state at $t = 0$. As the top wall moves slowly downwards the aggregate is compacted almost homogeneously as is indicated by the nearly vertical curves. At the top and bottom of the box wall effects produce a slight deviation.

chains. In fact, we also modified the strength of the twisting interaction but found that it had very little to no impact on the compressive curve. Therefore we do not alter twisting in this work.

Choosing $m_r = 8$ and $m_s = 2.5$, we obtain the red-dotted curve in Fig. 4. All in all, our modified interaction model is able to reproduce experimental results much better than the original version. In particular, for pressures below 100 kPa we observe a very good agreement with experimental data. However, we observe a deviation for pressures above 300 kPa. In our simulations a pressure of more than 1 MPa is required to further compress aggregates when a filling factor of about $\Phi = 0.52$ is reached.

In the quasi-static case the aggregate is given sufficient time to restructure and counteract the pressure exerted on the walls. Thus, we expect the filling factor increases homogeneously in the sample. In Fig. 5 the vertical profile of the filling factor is plotted for different stages of the compression process. To determine the filling factor profile, the sample is split vertically into equidistant intervals with the length of one particle diameter. Then, the average filling factor is calculated for each interval. Note that the fractal structure resulting in a filling factor of $\phi = 0.15$ in the bulk part of RBD-generated aggregates is not present at the bottom of the aggregate. Therefore the filling factor there exceeds the average value of $\phi = 0.15$.

During the compression process several snapshots of the filling factor profile have been taken. As expected the filling factor increases almost homogeneously for slow compression speeds. Keep in mind that it requires higher pressure to compact particles close to a wall since neighbouring particles have to be pushed away. Therefore the filling factor of the particle layers close to the top or bottom wall is lower compared to the rest of the aggregate for highly compacted aggregates. This effect causes the crescent shaped curves observed for highly compacted aggregates in Fig. 5.

The corresponding compressive strength curve for these low velocities is shown in Fig. 6. For compression speeds of 5 cm/s and below the differences to the quasi-static case remain small. For higher velocities we observe an increasing deviation from the quasi-static curve. Thus, the results from Güttler et al. (2009) cannot be applied for higher velocities.

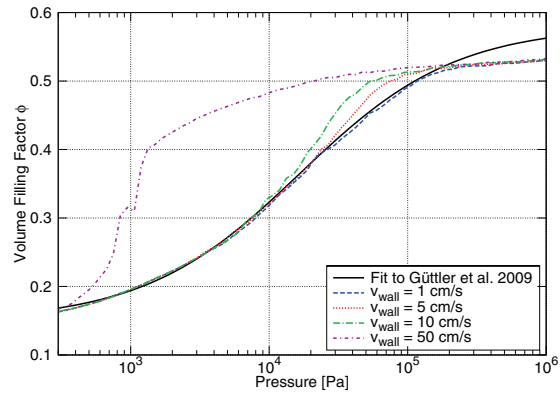


Fig. 6. Compressive strength for low velocity omnidirectional compression.

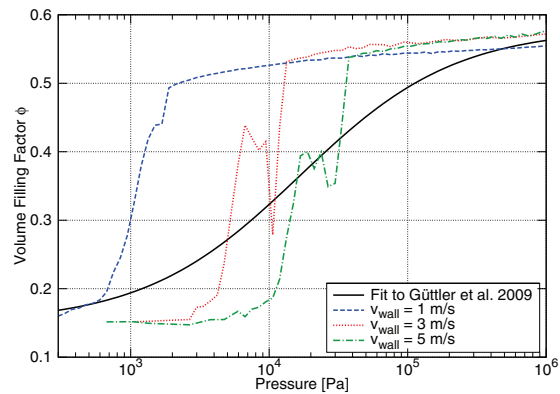


Fig. 7. Dynamic omnidirectional compression with v_{wall} between $1-5 \text{ m s}^{-1}$.

5.2.2. Dynamic case

In a second step, we studied the influence of large compression speeds. If the compression speed exceeds around 1 m s^{-1} the compression behavior changes considerably. The required simulation time is inversely proportional to the compression speed. Therefore we use a higher number of particles for compression experiments with wall speeds above 1 m s^{-1} . The box-shaped samples are composed of about 40 000 particles and feature a base length and height of $\approx 60 \mu\text{m}$. Compared to the quasi-static case the shape of the curves changes drastically, see Figs. 7 and 8. Instead of a smooth transition, three distinguished regimes emerge: the filling factor does not increase until a certain critical pressure is reached. Then, only a small additional pressure is required to compact the aggregate. When the aggregate is close to its final compaction the pressure again increases sharply.

This can be easily explained by looking at Fig. 9. When the compression speed exceeds a value of 1 m s^{-1} the aggregate is compacted inhomogeneously. The compression occurs too fast to allow the propagation of the top pressure through the entire sample. We clearly see the emergence of a very dense layer right beneath the top wall. This compact layer propagates downwards at the speed of the wall similar to a snowplough clearing freshly fallen snow. While pushing the dense layer downwards

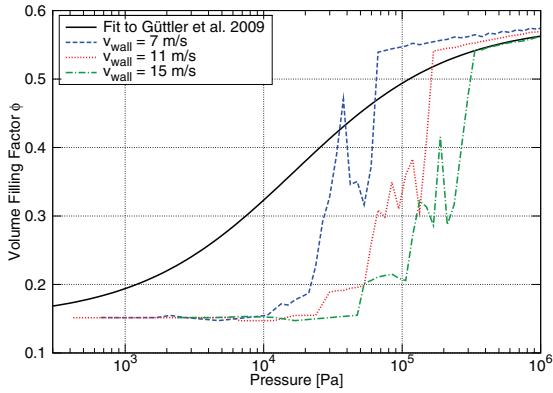


Fig. 8. Dynamic omnidirectional compression with v_{wall} between 7–15 m s^{-1} .

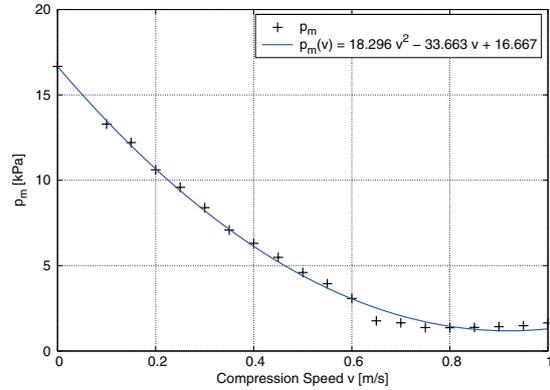


Fig. 10. Dependence of the fit parameter p_m of Eq. (31) on the compression speed v in the quasi static regime of $v \leq 1 \text{ m s}^{-1}$.

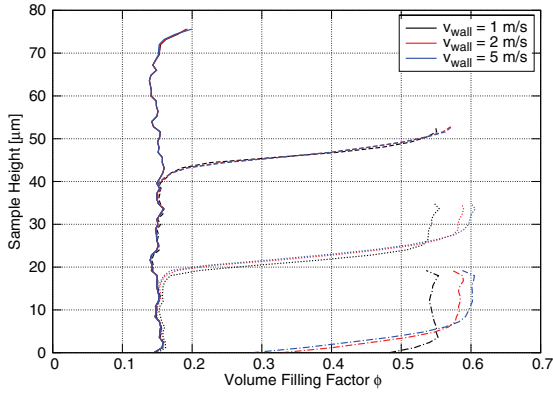


Fig. 9. Snapshots of the vertical profile of the filling factor. As the top wall moves downwards rapidly the compaction of the lower parts of the aggregate is lagging behind. The color indicates the compression speed whereas the line type indicates the position of the top wall. The solid lines show the filling factor profile of the initial uncompressed sample.

the pressure remains constant. After it reaches the bottom of the sample the pressure required to compress the sample a little bit further increases drastically. The sharp spikes shown in Figs. 7 and 8 result from the highly compacted layer reaching the bottom of the sample. The density wave is reflected from the bottom causing heavy fluctuations of the pressure on the top and bottom wall.

By comparing the filling factor profile during the compression to the initial one we can determine at which speed v_p the compaction is propagating downwards through the sample. For this purpose we measure the height where the initial and current filling factor profile deviate from each other and use the time that has passed since the start of the simulation to calculate the speed. Averaging over six different samples we obtain $v_p = 6.98 \pm 0.16 \text{ m s}^{-1}$.

To provide continuum-simulations with a simple recipe for the dynamic compressive strength we performed simulations using compression speeds up to 25 m s^{-1} . A few examples are shown in Figs. 7 and 8. For every compression speed we determine a fit curve similar to Eq. (31), where p_m and Δ serve as fitting parameters. Thus, we obtain values of p_m and Δ for different

compression speeds. In the last step we determine for each parameter an analytic approximation describing the dependency on the compression speed.

We observe different behavior between the quasi-static case for low velocities and the dynamic case for higher velocities. In the beginning, p_m decreases which means that the sample can be compressed more easily. This can be explained by the fact, that the aggregate is given less time to restructure and counteract the external pressure exerted on it by the wall. However, this effect will be reversed when the compression speed exceeds a critical value of $v_{\text{crit}} \approx 0.9 \text{ m s}^{-1}$. In the dynamic regime, it gets considerably harder to compress the sample with increasing velocity of the wall. Therefore it is helpful to distinguish between the two regimes.

In Fig. 10 the dependence of p_m on the compression speed v is shown for values of $v \leq 1 \text{ m s}^{-1}$. Using the ansatz $p_m(v) = av^2 + bv + c$ we obtain

$$p_m(v) = (18.296 v^2 - 33.663 v + 16.667) \text{ kPa}, \quad (32)$$

where the compression speed v is given in m s^{-1} .

In Fig. 11 the dependence of p_m on the compression speed v is shown for values of $v \geq 1 \text{ m s}^{-1}$. To find a simple analytic approximation we choose a power law of the form $p_m(v) = av^b + c$ and we obtain

$$p_m(v) = (1.340 v^{1.93} + 0.307) \text{ kPa}. \quad (33)$$

The fitted parabola describes the data points well. As the exponent of 1.93 is close to 2, we determine a second fit where the exponent was set to 2 and get

$$\tilde{p}_m(v) = (1.087 v^2 + 0.560) \text{ kPa}. \quad (34)$$

Similarly, for the parameter Δ (see Fig. 12) we obtain

$$\Delta(v) = (v + 1.598)^{-1.997} + 0.170. \quad (35)$$

5.3. Unidirectional compression

Additionally, we simulated the unidirectional compression of cylindrical samples of different sizes using the non modified model. The results are shown in Fig. 13 where again each curve is obtained by averaging the results for six different samples of

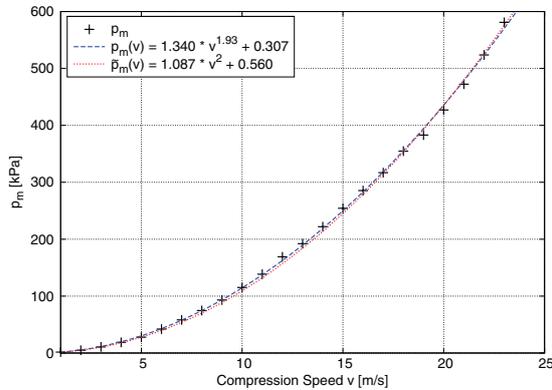


Fig. 11. Dependence of the fit parameter p_m of Eq. (31) on the compression speed v in the dynamic regime of $v \geq 1 \text{ m s}^{-1}$.

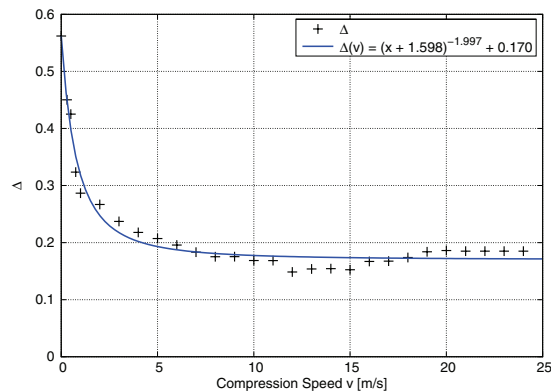


Fig. 12. Dependence of the fit parameter Δ of Eq. (31) on the compression speed.

equal size. To compare our results to [Paszun & Dominik \(2008\)](#) the speed of the top wall was set to $v_{\text{wall}} = 5 \text{ cm/s}$. Apparently there is a noticeable discrepancy between our simulations and the laboratory results. As in the case of omnidirectional compression, the pressure required to reach a certain filling factor is significantly lower in our simulations.

As we can see in [Fig. 13](#) the deviation for pressures above 10 kPa becomes more apparent if we increase the size of the samples. As [Paszun & Dominik \(2008\)](#) compressed very small samples using only about 300 particles this may be the reason why their results showed better agreement with laboratory results for higher pressures. However, their compressive strength curve was also shifted in the same direction as in this work.

Afterwards we tested the modified model with the same $m_r = 8$ and $m_s = 2.5$ as found above. As it is shown in [Fig. 14](#) (red dotted curve), the modified model agrees very well with the experimental results for pressures below 10^4 Pa . However, we still end up with considerably higher filling factors. A possible explanation is given by the fact that the size of the samples used in the laboratory experiments was on the order of centimeters and thus about 2000 times larger than our samples. [Blum & Schr apler \(2004\)](#) measured that the projected cross section increased by a factor of 1.6 during the compression process. To reach similar pressures in our simulations the sample has to be compressed until its height is only about two times the diameter

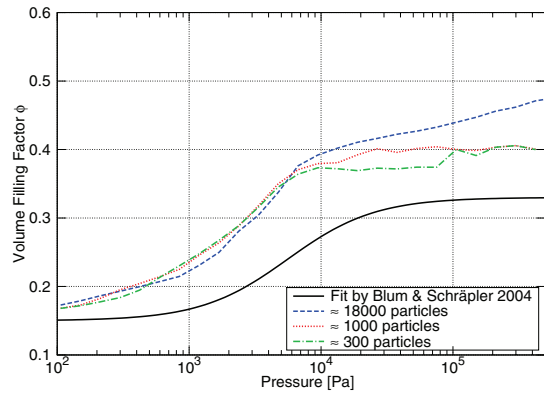


Fig. 13. Compressive strength for unidirectional compression of cylindrical aggregates of different size using the original Dominik & Tielens model. The black line has been obtained from experiments by [Blum & Schr apler \(2004\)](#).

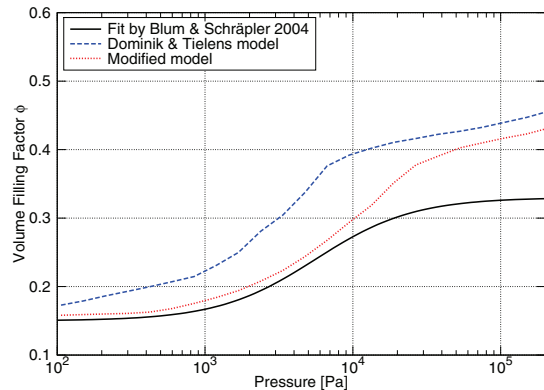


Fig. 14. Unidirectional compression of cylindrical aggregates using the modified model with 18 000 particles. The black line has been obtained from experiments by [Blum & Schr apler \(2004\)](#).

of a single monomer where the cross section increased roughly by a factor of 4. Due to the larger diameter of the laboratory samples it is harder for monomers in the center to flow in the outward direction.

6. Conclusions

We have performed molecular dynamics simulations to study the compressive strength of dust agglomerates which plays an important role in determining the outcome of mutual collisions. Using a special setup for the simulations we were able to compare our results in detail to the outcome of dedicated laboratory experiments.

Our simulations using the frequently applied interaction model by [Dominik & Tielens \(1997\)](#) indicate that real aggregates composed of micron sized silicate grains feature a greater stiffness. Since the primary bulk properties of material used for the individual monomers are known experimentally very well (see [Table 1](#)), we decided to vary the force constants (k_r and k_s) for rolling and sliding. Indeed, the higher stiffness can be accommodated by an increase of $m_r = 8$ and $m_s = 2.5$ (for k_r and k_s , respectively) in comparison to the quoted values

in Eqs. (17) and (18). After modifying the interaction model as described in Sect. 5.1, we have been able to reproduce the experimental results much better, and found very good agreement for both, unidirectional and omnidirectional compression. This work reveals the importance of the rolling and sliding interaction for the restructuring of aggregates. As these interactions currently lack experimental testing we feel it desirable to study in particular the rolling and sliding of micron sized grains in laboratory experiments.

We have also studied the influence of the wall speed on the compression behavior. If an aggregate is compressed slowly the filling factor increases homogeneously and the pressure needed to further compact the aggregate increases with increasing filling factor. For higher compression velocities a compacted layer emerges underneath the moving wall, similar to the shovel of a snow plow, when pushing away snow. Once this layer has formed the pressure remains nearly constant until the layer has reached the bottom of the sample. The transition from the static towards the dynamic case occurs at compression speeds on the order of 1 m s^{-1} . Since impact velocities of typical collisions of planetesimals lie within the range of $1\text{--}10 \text{ m s}^{-1}$ the dynamic compression behavior must be taken into account when simulating such collisions.

To determine the impact of the rescaling of the rolling and sliding forces on the very early phases in the planetesimal formation process, we plan to perform detailed collision simulations for a wide set of collision parameter. This will allow us to calculate *ab initio* the division between bouncing, sticking and fragmentation. This has recently been under experimental and theoretical scrutiny (Zsom et al. 2010; Geretshausen et al. 2011). It is hard to estimate the consequences of the new (stiffer) parameter set on the outcome of agglomerate collisions. We suspect that this can possibly lead to an enhanced sticking as more energy can be stored in the system before it breaks. Using a much larger particle number than previously will allow us to determine more accurately important bulk parameters such as the sound speed.

Acknowledgements. A. Seizinger acknowledges the support through the German Research Foundation (DFG) grant KL 650/16. Very helpful discussions with Carsten Güttler and Jürgen Blum from the experimental laboratory astrophysics group at Braunschweig, as well as with Carsten Dominik, Hidekazu Tanaka and Ralf Geretshausen are gratefully acknowledged. The authors acknowledge support through DFG grant KL 650/7 within the collaborative research group FOR 759 *The formation of planets*.

References

- Blum, J., & Wurm, G. 2000, *Icarus*, 143, 138
 Blum, J., & Wurm, G. 2008, *ARA&A*, 46, 21
 Blum, J., & Schräpler, R. 2004, *Phys. Rev. Lett.*, 93, 115503
 Blum, J., Wurm, G., Kempf, S., et al. 2000, *Phys. Rev. Lett.*, 85, 2426
 Brilliantov, N. V., Albers, N., Spahn, F., & Pöschel, T. 2007, *Phys. Rev. E*, 76, 051302
 Chokshi, A., Tielens, A. G. G. M., & Hollenbach, D. 1993, *ApJ*, 407, 806
 Dominik, C., & Nübold, H. 2002, *Icarus*, 157, 173
 Dominik, C., & Tielens, A. G. G. M. 1995, *Philos. Mag. A*, 72, 3, 783
 Dominik, C., & Tielens, A. G. G. M. 1996, *Philos. Mag. A*, 73, 5, 1279
 Dominik, C., & Tielens, A. G. G. M. 1997, *ApJ*, 480, 647
 Geretshausen, R. J., Speith, R., Güttler, C., Krause, M., & Blum, J. 2010, *A&A*, 513, A58
 Geretshausen, R. J., Meru, F., Speith, R., & Kley, W. 2011, *A&A*, 531, A166
 Gundlach, B., Kiliyas, S., Beitz, E., & Blum, J. 2011, *Icarus*, 214, 717
 Güttler, C., Krause, M., Geretshausen, R. J., Speith, R., & Blum, J. 2009, *ApJ*, 701, 130
 Güttler, C., Blum, J., Zsom, A., Ormel, C. W., & Dullemond, C. P. 2010, *A&A*, 513, A56
 Heim, L.-O., Blum, J., Preuss, M., & Butt, H.-J. 1999, *Phys. Rev. Lett.*, 83, 3328
 Johnson, K., Kendall, K., & Roberts, A. 1971, *Proc. Roy. Soc.*, 324, 301
 Kempf, S., Pfalzner, S., & Henning, T. K. 1999, *Icarus*, 141, 388
 Langkowski, D., Teiser, J., & Blum, J. 2008, *ApJ*, 675, 764
 Ormel, C. W., Paszun, D., Dominik, C., & Tielens, A. G. G. M. 2009, *A&A*, 502, 845
 Paszun, D., & Dominik, C. 2008, *A&A*, 484, 859
 Paszun, D., & Dominik, C. 2009, *A&A*, 507, 1023
 Pollack, J. B., Hubickyj, O., Bodenheimer, P., et al. 1996, *Icarus*, 124, 62
 Poppe, T., Blum, J., & Henning, T. 2000, *ApJ*, 533, 454
 Schäfer, C., Speith, R., & Kley, W. 2007, *A&A*, 470, 733
 Sirono, S.-I. 2004, *Icarus*, 167, 431
 Suyama, T., Wada, K., & Tanaka, H. 2008, *ApJ*, 684, 1310
 Teiser, J., & Wurm, G. 2009, *MNRAS*, 393, 1584
 Wada, K., Tanaka, H., Suyama, T., Kimura, H., & Yamamoto, T. 2007, *ApJ*, 661, 320
 Wada, K., Tanaka, H., Suyama, T., Kimura, H., & Yamamoto, T. 2008, *ApJ*, 677, 1296
 Wada, K., Tanaka, H., Suyama, T., Kimura, H., & Yamamoto, T. 2009, *ApJ*, 702, 1490
 Wada, K., Tanaka, H., Suyama, T., Kimura, H., & Yamamoto, T. 2011, *ApJ*, 737, 36
 Watson, P. K., Mizes, H., Castellanos, A., & Pérez, A. T. 1997, *Powders & Grains*, 109
 Weidenschilling, S. J. 1977, *MNRAS*, 180, 57
 Weidling, R., Güttler, C., Blum, J., & Brauer, F. 2009, *ApJ*, 696, 2036
 Windmark, F., Birnstiel, T., Güttler, C., et al. 2012, *A&A*, 540, A73
 Wurm, G., Paraskov, G., & Krauss, O. 2005, *Icarus*, 178, 253
 Zsom, A., Ormel, C. W., Güttler, C., Blum, J., & Dullemond, C. P. 2010, *A&A*, 513, A57

THE PHYSICS OF PROTOPLANETESIMAL DUST AGGLOMERATES. VII. THE LOW-VELOCITY COLLISION BEHAVIOR OF LARGE DUST AGGLOMERATES

RAINER SCHRÄPLER¹, JÜRGEN BLUM¹, ALEXANDER SEIZINGER², AND WILHELM KLEY²

¹Institut für Geophysik und extraterrestrische Physik, University of Braunschweig Mendelssohnstr. 3, D-38106 Braunschweig, Germany; r.schraepler@tu-bs.de

²Institut für Astronomie und Astrophysik, University of Tübingen Auf der Morgenstelle 10, D-72076 Tübingen, Germany
Received 2012 March 30; accepted 2012 August 14; published 2012 September 24

ABSTRACT

We performed micro-gravity collision experiments in our laboratory drop tower using 5 cm sized dust agglomerates with volume filling factors of 0.3 and 0.4, respectively. This work is an extension of our previous experiments reported in Beitz et al. to aggregates of more than one order of magnitude higher masses. The dust aggregates consisted of micrometer-sized silica particles and were macroscopically homogeneous. We measured the coefficient of restitution for collision velocities ranging from 1 cm s⁻¹ to 0.5 m s⁻¹, and determined the fragmentation velocity. For low velocities, the coefficient of restitution decreases with increasing impact velocity, in contrast to findings by Beitz et al. At higher velocities, the value of the coefficient of restitution becomes constant, before the aggregates break at the onset of fragmentation. We interpret the qualitative change in the coefficient of restitution as the transition from a solid-body-dominated to a granular-medium-dominated behavior. We complement our experiments by molecular-dynamics simulations of porous aggregates and obtain a reasonable match to the experimental data. We discuss the importance of our experiments for protoplanetary disks, debris disks, and planetary rings. This work is an extension to the previous work of our group and gives new insight into the velocity dependency of the coefficient of restitution due to improved measurements, better statistics, and a theoretical approach.

Key words: methods: laboratory – methods: numerical – planets and satellites: formation – planets and satellites: rings – protoplanetary disks

Online-only material: color figures

1. INTRODUCTION

There is observational evidence that cm-sized particles exist in protoplanetary disks (PPDs; see, e.g., Wilner et al. 2005). A recent model of protoplanetary-dust growth, based on laboratory experiments, has shown that cm-sized particles can be formed by direct collisional sticking (Güttler et al. 2010; Zsom et al. 2010). Güttler et al. (2010) also found that collisional compaction can lead to filling factors of up to 0.57. Compaction in fragmenting collisions with mass transfer was also found by Kothe et al. (2010), who confirmed the model by Güttler et al. (2010).

If there were even larger solid particles available in PPDs, then the growth could commence through a fragmentation-coagulation cycle, leading to dust-aggregate sizes in the planetesimal size range (Windmark et al. 2012). As the dust growth in PPDs starts with (sub-) μm dust grains, it is natural to assume that the resulting macroscopic bodies are agglomerates of the microscopically small dust grains. Many bodies in debris disks and planetary rings are also expected to consist of such granular material. Therefore, it is interesting and important to know the collision behavior of very large dust aggregates. A first approach to the $>\text{cm}$ size range was established by Beitz et al. (2011), who investigated collisions among 2 cm sized dust aggregates. Here, we present follow-up experiments with 5 cm sized dust aggregates, which are more than an order of magnitude larger in mass.

In Sections 2 and 3, we describe our experimental approach and the experimental results. Section 4 explains the numerical model used to understand the physics in dust-aggregate collisions, and Section 5 gives some astrophysical applications for low-velocity collisions of granular bodies. Finally, Section 6 summarizes our results.

2. EXPERIMENTAL APPROACH

In this section, we describe the experimental methods applied for the determination of the coefficient of restitution and the fragmentation threshold of 5 cm sized dust agglomerates.

2.1. Preparation of the Dust Agglomerates

The dust material for the production of large aggregates was pure SiO₂ powder, consisting of 0.1–10 μm sized irregular grains. Owing to the fact that direct growth can commence through the millimeter-size range where a new growth process (e.g., fragmentation with mass transfer) occurs, we expect that large dust agglomerates in PPDs possess a hierarchic structure and are agglomerates of agglomerates. Therefore, prior to compression into large dust aggregates, the dust powder was being sieved through a mesh with a width of 0.5 mm to avoid larger aggregates. As shown by Weidling et al. (2012), the sieving process produces dust agglomerates with a filling factor of 0.35. The sieved dust was then filled into a hollow steel cylinder with 5 cm diameter and was then slowly compressed with a brass piston. The volume filling factor of the compressed dust aggregates was adjusted by filling the cylinder with a defined dust mass m and by compressing the sample to a pre-determined height of 5 cm. After the compression, the bottom of the steel cylinder was removed and the dust agglomerate was pushed out of the cylinder using the piston.

2.2. Morphology of the Dust Agglomerates

To examine the inner structure of our dust agglomerates, we performed X-ray tomography (XRT) measurements. Figure 1 shows a plane perpendicular to the cylinder axis of 5 cm diameter and also granularity, which represents the original sieved dust

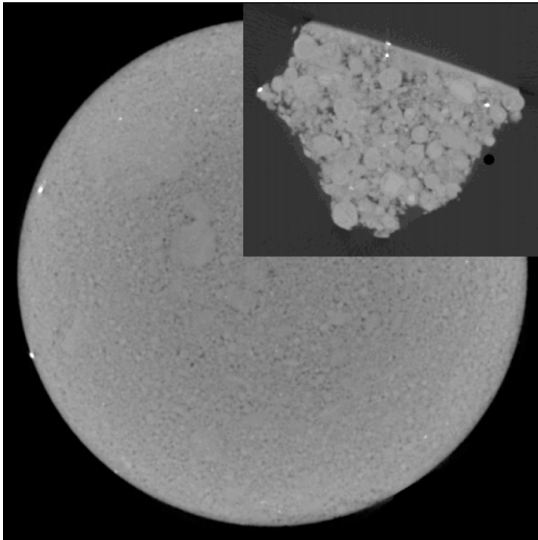


Figure 1. Reconstruction of an XRT image showing a radial slice perpendicular to the cylinder axis in the center of the dust agglomerate (window size: 5.9 cm \times 5.9 cm). Inset: cutout of a piece of the dust agglomerate, including the cylinder mantle (window size: 0.63 cm \times 0.54 cm).

aggregates. This sub-structure is not visible in some areas of a few millimeters in radius. We think that this is caused by slightly inhomogeneous compression. To increase the resolution of the XRT, we cut a millimeter-sized piece out of a larger dust aggregate, which included the cylinder mantle, and repeated the XRT measurements with a voxel size of $17\ \mu\text{m} \times 17\ \mu\text{m} \times 17\ \mu\text{m}$. In the inset of Figure 1, a cut through the center of the sample is displayed, with the former cylinder mantle at the top of the inset picture. On the cylinder mantle, the agglomerate-of-agglomerates structure is not present. The material has obviously formed a slightly densified mantle of about $85\ \mu\text{m}$ thickness with a filling factor of 0.35. We do not think that this slight density increase of about 10% has a considerable effect on the impact behavior of the dust agglomerates.

Figure 2 shows the density distribution inside the dust agglomerate. In the top graph, the mean density of planes perpendicular to the cylinder axis is shown over the full height of the agglomerate. The median volume filling factor of the dust agglomerate is ~ 0.3 . At the top 6 mm of the dust-agglomerate cylinder, the mean density is increased to a filling factor of up to 0.38. This is the place where the piston has pushed against the agglomerate during compression. In the lower 5 mm of the dust aggregate, the density of the agglomerate rapidly decreases to a volume filling factor of about 0.15. The lower graph of Figure 2 shows the radial density distribution averaged over the azimuth and over 20% of the cylinder height for each curve. The upper curve was averaged over the upper 20% of the dust agglomerate. The three curves in the center were averaged over the central 20%–40%, 40%–60%, and 60%–80% slices of the dust agglomerate. Keep in mind that these three curves have basically the same values and overlap in Figure 2. The lower curve was averaged over the lower 20% of the dust-agglomerates height. The lower graph of Figure 2 shows that the density of the central part of the dust agglomerate increases slightly from the axis to the mantle by about 5% in a volume filling

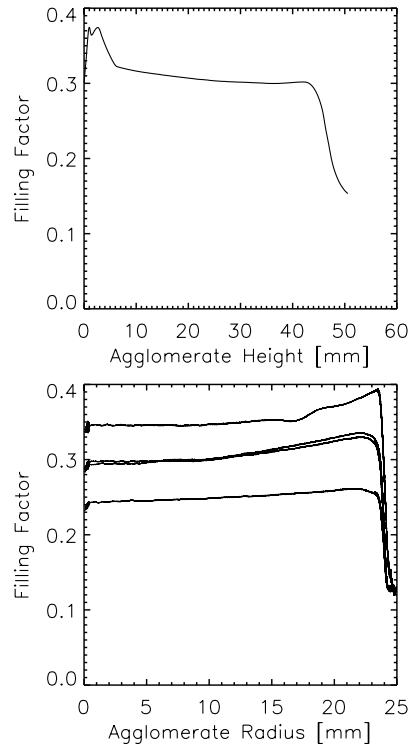


Figure 2. Volume filling factors derived from the XRT measurements of a dust agglomerate. Top graph: the mean density of planes perpendicular to the cylinder axis as a function of the height of the dust agglomerate. Bottom graph: the radial density distribution averaged over the azimuth and 20% of the dust-cylinder height for five vertical positions of the dust agglomerate. The uppermost curve belongs to the top part of the dust aggregate, the three center curves (partly overlapping) belong to its central parts, and the lower curve represents the lower portion of the dust agglomerate.

factor. Here, the top and bottom curves are of no particular importance because the dust agglomerates collide close to their midplanes. Within the accuracy of the XRT measurements (~ 10 – $100\ \mu\text{m}$), only slightly densified material on the dust-agglomerate’s cylinder mantle is found, which we believe does not dramatically influence the collisional outcome.

2.3. Collision Experiments

The collision experiments using the dust aggregates described above are performed in our 1.5 m laboratory drop tower described in Beitz et al. (2011). The agglomerates were placed above each other with their symmetry axes rotated by 90° (see Figure 3, top). Each dust agglomerate is supported by two brackets, which can be rapidly pulled away by solenoid magnets. The upper dust agglomerate is released slightly earlier than the lower one (see Figure 3). The time difference Δt between the release of the upper and lower dust agglomerate results in a relative velocity $v = g\Delta t$ between the two bodies, where $g = 9.8\ \text{m s}^{-2}$ is the surface acceleration of the Earth. As the drop tower is evacuated to a residual gas pressure of 100 Pa, air drag can be neglected during the $\sim 0.5\ \text{s}$ free-fall time.

The resulting impacts are observed by two cameras (one high-speed camera, one camera with a normal frame rate) with



Figure 3. Top: the two dust agglomerates shortly after release and before the collision. Both release mechanisms are fully open. Bottom: the two dust agglomerates fragment shortly after impact.

90° angular distance. The cameras, which are outside the drop tower, are released such that they fall in the center-of-mass frame of the two dust aggregates.

The release mechanisms of the two dust agglomerates cause a slight rotation of the two bodies. Furthermore, the collisions were not always perfectly central, which also causes rotation. To account for these effects, we calculated the coefficient of restitution from the ratio of the square root of the total kinetic energies of the two dust agglomerates in their center-of-mass frame before and after the collision,

$$e = \left(\frac{m^* v_2^2 + I(\omega_{21}^2 + \omega_{22}^2)}{m^* v_1^2 + I(\omega_{11}^2 + \omega_{12}^2)} \right)^{\frac{1}{2}}. \quad (1)$$

Here, v_1 and v_2 are the relative translational velocities of the two dust aggregates before (index 1) and after (index 2) the

collision; ω_{11} , ω_{12} , ω_{21} , and ω_{22} are the mutually perpendicular angular velocity components of the colliding cylinders (the first index refers to before and after the collision, the second index describes which of the agglomerates is meant); and $m^* = m/2$ and I are the reduced mass and the moment of inertia of the two dust aggregates. Please note that we only consider rotation of the dust cylinders around axes perpendicular to their symmetry axis. The rolling motion of the agglomerate as well as the rotations of the agglomerate in the third possible direction were measured and found negligible. They are very small because of the impact and release geometry of the agglomerates. The effective relative velocity, including rotation effects, of the agglomerates prior to the collision is then given by

$$v_{\text{eff}} = \left(\frac{m^* v_1^2 + I(\omega_{11}^2 + \omega_{12}^2)}{m^*} \right)^{\frac{1}{2}}. \quad (2)$$

This rotation of the dust aggregates is only important at the very lowest impact velocities; at higher relative velocities, the rotational motion prior to the impact is negligible with respect to the rotation after the impact.

At velocities lower than $\sim 10 \text{ cm s}^{-1}$, the statistical scattering of the single measurement was very high. This was due to the fact that the free fall time of the dust aggregates was limited to $\sim 0.5 \text{ s}$. At 1 cm s^{-1} impact velocity and a free fall time of 0.5 s , the maximal distance before and after the impact is only 2.5 mm . This is, from both the preparatory point of view and for data-analysis reasons, a limiting value so that lower impact velocities were not achievable. Therefore, more experiments have been performed at the lower velocities to get a reasonable mean value for the coefficient of restitution.

3. EXPERIMENTAL RESULTS

In this section, we will present our data on the low-velocity coefficients of restitution as well as on the fragmentation velocities of dust aggregates of two different volume filling factors.

3.1. Coefficient of Restitution

In Figure 4, the coefficient of restitution of our 5 cm sized cylindrical agglomerates, according to the definition in Equation (1), is plotted as a function of the effective impact velocity, according to Equation (2), for volume filling factors of $\phi = 0.3$ and $\phi = 0.4$, respectively. Each data point is the mean of four measurements; the error bars denote the 2σ error of the mean value.

We can clearly distinguish different velocity regions. (1) At the very lowest velocities ($v_{\text{eff}} \lesssim 4 \text{ cm s}^{-1}$), the coefficient of restitution follows the solid-state model by Thornton & Ning (1998) within the measurement uncertainties as shown by the error bars in Figure 4 (see Section 4.1). (2) At higher velocities ($4 \text{ cm s}^{-1} \lesssim v_{\text{eff}} \lesssim 6 \text{ cm s}^{-1}$ for a filling factor of 0.3 and $4 \text{ cm s}^{-1} \lesssim v_{\text{eff}} \lesssim 10 \text{ cm s}^{-1}$ for a filling factor of 0.4), the coefficient of restitution decreases steeply to values of $e = 0.2$ for $\phi = 0.3$ and $e = 0.3$ for $\phi = 0.4$, respectively. (3) The coefficient of restitution remains constant even for higher velocities. (4) Until fragmentation dominates for $v_{\text{eff}} > \sim 10 \text{ cm/s}$ (see Section 3.2).

The coefficient of restitution was measured by considering translational and rotational velocity changes. Because translational and rotational velocities are transformed into one another, depending on the impact parameter, it is not possible to split the

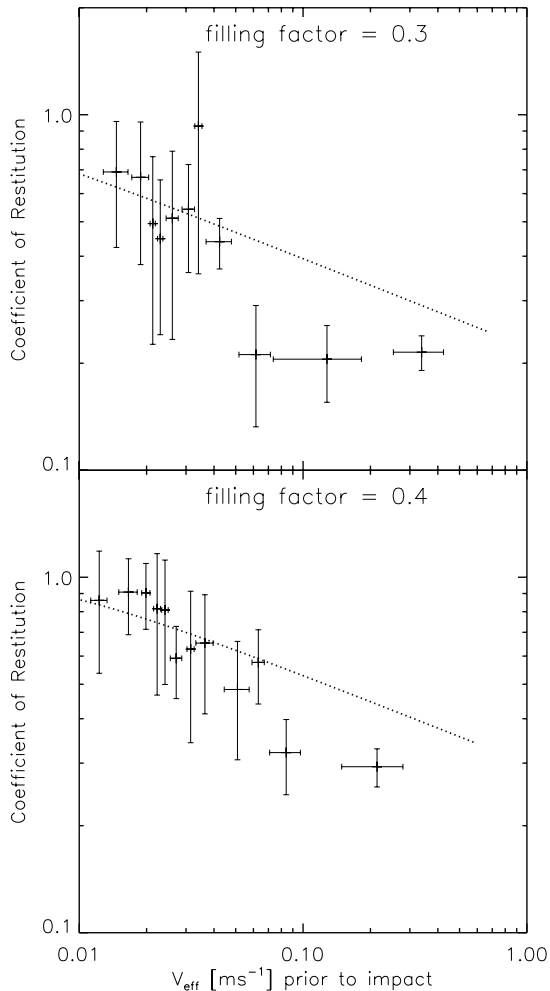


Figure 4. Coefficient of restitution as a function of the effective impact velocity for 5 cm sized dust agglomerates of 30% volume filling factor (upper graph) and 40% volume filling factor (lower graph), respectively. Each data point is the mean value of four measurements; the error bars denote the 2σ uncertainties of the mean values. The dotted line shows a power law with a slope of $-1/4$, following the solid-state model by Thornton & Ning (1998; see Section 4.1).

coefficient of restitution into components of rotation and translation. To show the contribution of rotation in our measurements, we display in Figure 5 the ratio of the translational velocity to the effective velocity prior to the impact as well as the ratio of the coefficients of restitution with and without the consideration of rotation over the effective impact velocity. We use the same averaging process as in Figure 4. Figure 5 shows that the rotational contribution in our measurements is below 40% over all velocities and that the influence of rotation on the coefficient of restitution increases with decreasing impact velocity. However, the data also show that the different regimes of the coefficient of restitution (see above) are not caused by rotation effects.

In contrast to our result, Beitz et al. (2011) found no obvious correlation between the coefficient of restitution and impact velocity. Unlike in our experiments, they used smaller spherical

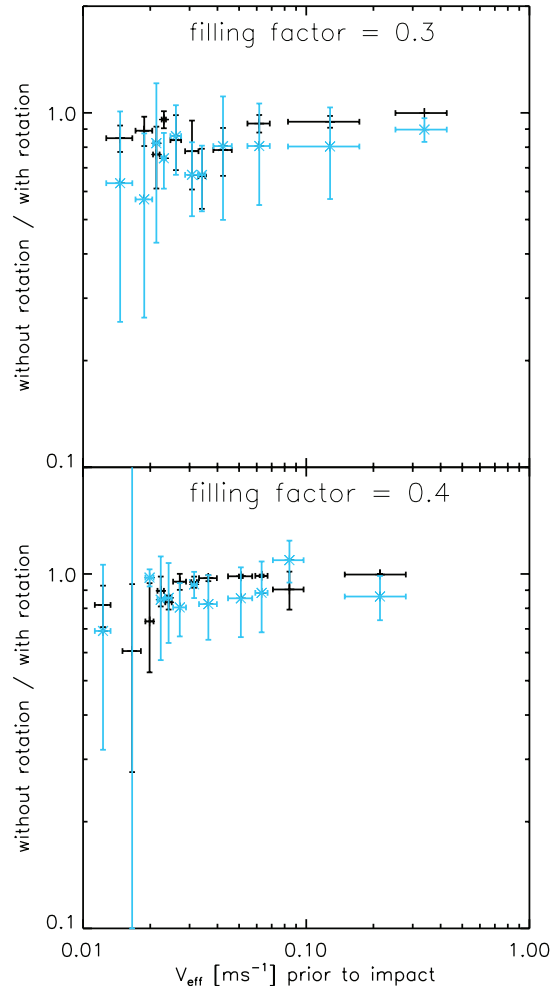


Figure 5. Ratio of the effective reduced velocity (including rotation) to linear velocity prior to impact (+) and the ratio of the coefficient of restitution including rotational effects to the coefficient of restitution with neglected rotation (*).

(A color version of this figure is available in the online journal.)

dust agglomerates made from monodisperse spherical grains. We used cylindrical agglomerates because we were not able to produce homogeneous crack-free spherical dust agglomerates. Our polydisperse irregular SiO_2 grains possess smaller contact forces between the monomer particles than the monodisperse spherical grains of Beitz et al. (2011). This and the smaller filling factor in our experiments ease collisional compression and reduce the effect of randomly jammed packings during collision (see, e.g., Torquato & Stillinger 2010). Jammed packings are stronger at higher compression velocities and increase the rigidity of an agglomerate, and therewith decrease the contact area of the colliding agglomerates. According to the model by Thornton & Ning (1998), this should increase the coefficient of restitution. Therefore, it is possible that jamming occurred in the experiments by Beitz et al. (2011), due to their higher

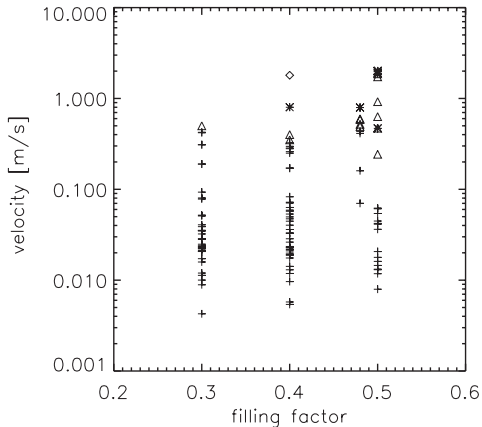


Figure 6. Possible outcomes in collisions among 5 cm sized dust aggregates for different volume filling factors between $\phi = 0.3$ and $\phi = 0.48$. A + denotes bouncing, Δ stands for the fragmentation of one of the two dust aggregates, * and \diamond describe the fragmentation of both dusty bodies, the latter with a maximum fragment mass smaller than half of the projectile mass. For comparison, the data from Beitz et al. (2011) for 2 cm sized spherical dust aggregates with $\phi = 0.5$, using spherical $1.5 \mu\text{m}$ sized SiO_2 monomers, are also shown

filling factor and monodisperse spherical grains, which is more pronounced at higher collisional velocities.

3.2. Fragmentation Velocity

Above a certain impact velocity, one or both of the colliding dust aggregates fragment so that the determination of the coefficient of restitution becomes meaningless. We measured the outcome of collisions among the 5 cm sized dust aggregates with volume filling factors of $\phi = 0.3$, $\phi = 0.4$, and $\phi = 0.48$ for velocities up to 200 cm s^{-1} and plotted the collision results in Figure 6. The + signs denote bouncing, Δ stands for the fragmentation of one of the two dust aggregates, whereas * and \diamond describe the fragmentation of both dusty bodies (in the latter case, with a maximum fragment mass smaller than half of the projectile mass). For comparison, we added the data from Beitz et al. (2011) for 2 cm sized spherical dust aggregates with $\phi = 0.5$, using spherical $1.5 \mu\text{m}$ sized SiO_2 monomers. Within the scatter of data, the threshold between bouncing and single-aggregate fragmentation seems to be independent of the volume filling factor at $v_{\text{frag}} = 40 \pm 10 \text{ cm s}^{-1}$. This is about a factor of two higher than the fragmentation threshold found by Beitz et al. (2011) and might be due to different geometry (spheres versus cylinders), different monomer morphologies and sizes (irregular polydisperse versus spherical monodisperse), dust-aggregate size (5 cm versus 2 cm), or volume filling factor ($\phi \leq 0.48$ versus $\phi = 0.5$).

4. MODELING DUST-AGGREGATE COLLISIONS

4.1. Continuum Theories

Assuming that at low velocities dust agglomerates behave like solid bodies, we can apply the theory of Thornton & Ning (1998) for the derivation of the impact-velocity dependence of the coefficient of restitution. At larger velocities, we assume that the granular material gets more and more mobilized and begins to fluidize so that a solid-state theory is no longer applicable. The model by Thornton & Ning (1998) relies on two threshold

Table 1
Material Parameters of the Individual Monomers Used in the Molecular Dynamics Simulations.

Physical Property	Silicate
Particle radius r (in μm)	0.6
Density ρ (in g cm^{-3})	2.65
Surface energy γ (in mJ m^{-2})	20
Young's modulus E (in GPa)	54
Poisson number ν	0.17
Critical rolling length ξ_{crit} (in nm)	2

velocities, the transition velocity between sticking and bouncing and the transition velocity between elastic and plastic material effects, v_y , respectively. The data shown in Figure 4 suggest that our collision velocities are clearly above both thresholds because the coefficient of restitution is in the regime in which energy-dissipating effects dominate. In this velocity regime, Thornton & Ning (1998) predict a decrease of the coefficient of restitution with increasing velocity and an asymptotic power-law behavior of the coefficient of restitution of the form of $e \propto v^{-1/4}$. The dotted line in Figure 4 shows such a dependence, with $v_y = 0.12 \text{ cm s}^{-1}$ for $\phi = 0.3$ and $v_y = 0.4 \text{ cm s}^{-1}$ for $\phi = 0.4$, respectively. As can be seen in the comparison between the model and our data, our 5 cm sized dust aggregates can be reasonably described by the Thornton & Ning (1998) continuum theory for effective impact velocities up to $\sim 4 \text{ cm s}^{-1}$. However, for larger impact speeds, the coefficient of restitution drops below the curve predicted by Thornton & Ning (1998) and is rather velocity independent for velocities between $\sim 10 \text{ cm s}^{-1}$ and the fragmentation limit (see Figure 4).

4.2. Molecular-dynamics Simulations of Dust-aggregate Collisions

To understand these different collision behaviors of dust aggregates, we use a molecular-dynamics approach featuring detailed contact mechanics of microscopic silicate grains. The corresponding interaction laws have been proposed by Johnson et al. (1971) and Dominik & Tielens (1995, 1996). An overview is given by Dominik & Tielens (1997) who applied the model to simulate dust-agglomerate collisions for the first time in the context of planet formation. Later, Wada et al. (2007) presented a different approach where the same interaction laws were derived from potentials. Recently, Seizinger et al. (2012) proposed simple modifications to the model to better reproduce the compression behavior measured in laboratory experiments by Güttler et al. (2009).

In this work, the modified model of Seizinger et al. (2012) is used. The material parameters used here are given in Table 1. They are identical to those of Seizinger et al. (2012) but differ from the ones used for similar simulations performed by Wada et al. (2011).

4.2.1. Sample Generation

Here, we study the collisions of spherical aggregates. The samples were generated using the following procedure: we began with the regular lattice of the hexagonal closest packing (hcp) for which the volume filling factor is given by $\phi = \pi/2\sqrt{3} \approx 0.74$. To achieve lower filling factors, we removed the proper amount of randomly selected monomers. Especially for lower filling factors, some monomers may end up disconnected from the rest of the aggregate. In the last step, we therefore removed all isolated monomers which were not connected to the

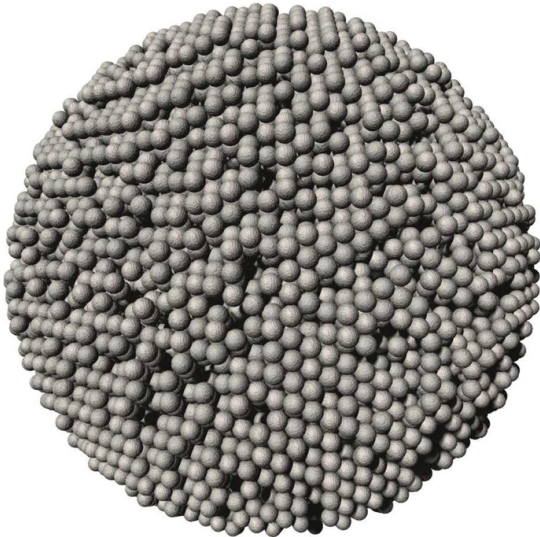


Figure 7. Example of an aggregate used for the collision simulations. It possesses a mean filling factor of $\phi = 0.55$ and consists of $\approx 40,000$ monomers.

main aggregate (typically less than 10^{-3} of the total number of monomers). Except for the removal of isolated monomers, this preparation method has been used by Wada et al. (2011) before.

The samples we used in this work consist of approximately 4×10^4 monomers, with a coordination number of ≈ 8.6 , a diameter of $50 \mu\text{m}$, and a volume filling factor of $\phi \approx 0.55$. An image of such a sample is shown in Figure 7.

4.2.2. Numerical Collision Experiments

Three samples generated by the procedure described above were rotated randomly and collided head-on with impact velocities between 0.01 and 0.5 m s^{-1} . In the case of a bouncing event, we determined the relative velocity between the

collision partners by averaging over the individual velocities of the monomers that each aggregate was composed of.

Due to the lattice structure of the samples, their relative orientation has a significant influence on the outcome of the collision. Depending on this orientation, both sticking and bouncing may occur for a given velocity. As we intended to study the dependency of the coefficient of restitution on the collision velocity, we kept the same orientation for a whole collision sequence. For each sample, eight randomly chosen orientations were examined. Thus, 24 collision sequences have been simulated in total. Typically, not all collisions of one sequence resulted in bouncing.

4.2.3. Results

The results of these collision sequences for the coefficient of restitution are shown in Figure 8. Similar to the laboratory experiments, one can distinguish between different velocity regimes. The velocity dependency of the coefficient of restitution can be well fitted by power laws, $e(v) = av^b$. We determined two fits $e_{\text{low}}(v)$ for the low-velocity regime ranging from 1 cm s^{-1} to 7 cm s^{-1} and $e_{\text{high}}(v)$ for velocities from 5 cm s^{-1} to 33 cm s^{-1} . We obtain $a_{\text{low}} = 0.219$, $b_{\text{low}} = -0.268$ and $a_{\text{high}} = 0.109$, $b_{\text{high}} = -0.513$. For the low-velocity regime, the exponent of the power law agrees very well with the one derived by Thornton & Ning (1998) for the continuum theory, i.e., $b_{\text{theory}} = -0.25$. The error bars show the influence of the orientation of the colliding aggregates on the outcome of the collision. For velocities higher than 33 cm s^{-1} , we did not observe bouncing behavior anymore.

For low-velocity collisions, the kinetic impact energy is too low to restructure the aggregates, and thus the energy is mainly dissipated by the formation and breaking of contacts between the monomers, as shown in Figure 9. At velocities above 2 cm s^{-1} , restructuring of the dust aggregate sets in. As we can see in Figure 10, inelastic rolling and sliding become the most important dissipative channels. The dominance of the inelastic sliding results from the high compactness of the aggregates. Due to the large coordination number, monomers are tightly fixed by their

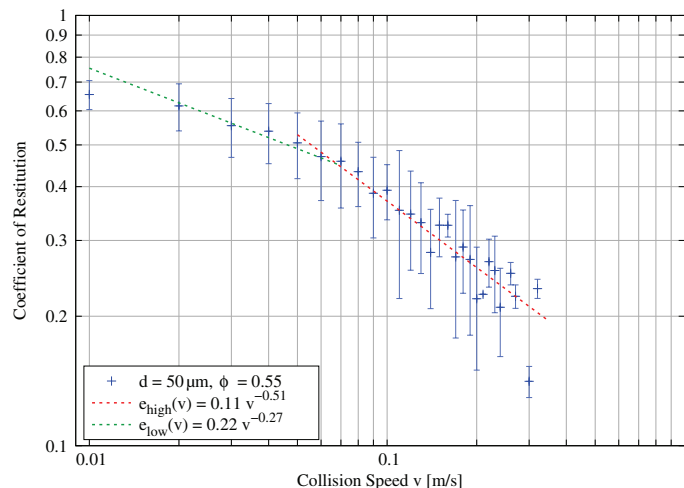


Figure 8. Dependency of the coefficient of restitution on the collision velocity obtained from molecular-dynamics simulations. The collision partners are two identical $\approx 50 \mu\text{m}$ sized spherical dust aggregates having a mean porosity of $\phi \approx 0.55$.

(A color version of this figure is available in the online journal.)

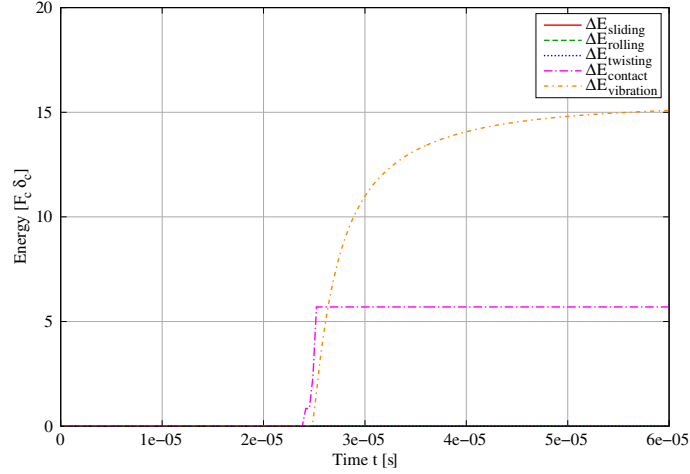


Figure 9. Energy dissipation during a bouncing collision in the low-velocity regime with an impact velocity of 1 cm s^{-1} . The impact occurs after $23 \mu\text{s}$. The kinetic energy is dissipated by contact formation and breaking and vibrations of monomers. (A color version of this figure is available in the online journal.)

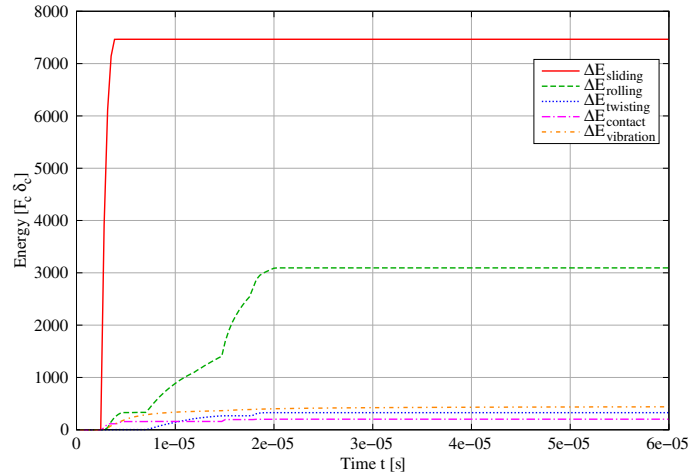


Figure 10. Energy dissipation of a bouncing collision in the high-velocity regime with an impact velocity of 10 cm s^{-1} . The impact occurs after $2.3 \mu\text{s}$. Contrary to the low-velocity regime (Figure 9), energy is mainly being dissipated by inelastic sliding and rolling. (A color version of this figure is available in the online journal.)

neighbors, which limits the amount of inelastic rolling that may occur.

Given the vast differences in monomer-particle numbers between the experimental and the model dust aggregates, the agreement in the range of absolute values of the coefficient of restitution and the occurrence of different physical regimes is striking. Both approaches show a solid-state-like behavior for very low impact velocities and deviations from the expected power law with a slope of $-1/4$ for higher velocities.

5. ASTROPHYSICAL APPLICATIONS

5.1. Protoplanetary Disks

It has only recently been shown that cm-sized dust aggregates can grow in PPDs (Zsom et al. 2010). Under certain conditions,

even larger dust aggregates can be formed. Windmark et al. (2012) showed that a few indestructible, cm-sized solid bodies can trigger further growth of dust aggregates through a fragmentation and re-accretion cycle. Baroclinic vortices (Klahr & Bodenheimer 2004) or streaming instabilities (Youdin & Goodman 2005) can concentrate cm-sized or larger dust aggregates to high number densities. In all such cases, knowledge about the low- and intermediate-velocity collision behavior of dust aggregates is of the utmost importance to correctly describe the fate of the dusty components. In highly mass-loaded regions of PPDs, such as instability regions, the coefficient of restitution determines the reduction of the relative velocities among the dust aggregates. A low value of the coefficient of restitution eases the occurrence of gravitational instabilities. It is thus important to know the threshold

velocity for the onset of fragmentation, so that the size evolution of the dust aggregates, and thus the efficiency of the gravitational instability in PPDs, can be correctly determined (see Johansen et al. 2006, 2008, 2012).

5.2. Debris Disks

As relative velocities in virtually gas-free debris disks are typically larger than tens of meters per second, fragmentation dominates the outcomes in collisions between dust aggregates. Thus, one would expect a broad size distribution of dust aggregates from the monomer grains or the radiation-pressure blowout size (whatever is larger) to the largest occurring bodies. However, the recent discovery of ultra-cold debris disks with dust temperatures below the blackbody equilibrium temperature has severely challenged this picture (Eiroa et al. 2011). Such low temperatures require dust materials with very low absorption in the far-infrared and the absence of a source for particles smaller than the wavelength. The former can possibly be reached with icy constituents, while the latter requires collision velocities below the fragmentation threshold.

We found in our investigation that the fragmentation limit is as low as $\sim 50 \text{ cm s}^{-1}$ for large dust aggregates consisting of micrometer-sized SiO_2 grains. This is very close to the $\sim 100 \text{ cm s}^{-1}$ sticking threshold for the monomer particles (Poppe et al. 2000). Unfortunately, it has only recently been possible to produce micrometer-sized water-ice particles (Gundlach et al. 2011) so that impact experiments with monomer particles and aggregates have not yet been performed. However, the experiments by Gundlach et al. (2011) showed that the surface force for the water-ice particles is about a factor of 10 higher than for silica so that one can expect a similar increase for the threshold velocities for monomer sticking and aggregate fragmentation, i.e., $v_{\text{frag,ice}} \approx 10 \text{ m s}^{-1}$. Future experiments will have to show whether or not this is true.

5.3. Planetary Rings

In Saturn's main rings, the particle sizes have been estimated to range from $\sim 1 \text{ cm}$ to $\sim 10 \text{ m}$ (Zebker et al. 1985) and are believed to be at least covered by a regolith layer (Poulet & Cuzzi 2002), which makes them similar in their collision behavior to our dust aggregates. In the rings, the orbital shear leads to random velocities among the ring particles. This effect is counterbalanced by the energy loss due to the inelastic collisions among the ring particles, leading to a steady-state velocity distribution if and only if the coefficient of restitution decreases with increasing collision velocity. A basic description of this behavior is given in Goldreich & Tremaine (1978). The authors also found a direct correlation between the optical depth of the ring and the coefficient of restitution if the rings are in dynamical equilibrium. For reasonable optical depths for Saturn's main rings, the required coefficients of restitution are $e \gtrsim 0.6$. Both conditions, the negative correlation between the coefficient of restitution and the collision velocity as well as the required values of the coefficient of restitution, show that the physical composition of the ring particles must be such that the threshold velocity between elastic and plastic impacts is just slightly lower than the typical impact speeds ($\lesssim 1 \text{ cm s}^{-1}$). Clearly, much more work has to be done before we can really understand the collision behavior of ring particles (e.g., use icy aggregates, much lower collision velocities, include rotation, etc.), but the dust-aggregate collision experiments presented in this article show how to proceed.

6. SUMMARY

We investigated the low-velocity collision behavior of 5 cm sized cylindrical dust agglomerates made by compression of micrometer-sized SiO_2 particles. We measured the coefficient of restitution and the onset of fragmentation for agglomerates with volume filling factors of $\phi = 0.3$ and $\phi = 0.4$ and found that (1) at the very lowest velocities ($v_{\text{eff}} \lesssim 4 \text{ cm s}^{-1}$), the coefficient of restitution follows the solid-state model by Thornton & Ning (1998) within the measurement uncertainties as shown by the error bars in Figure 4; (2) that the coefficient of restitution decreases steeply to $e = 0.2$ for a volume filling factor of 0.3 for velocities of $4 \text{ cm s}^{-1} \lesssim v_{\text{eff}} \lesssim 6 \text{ cm s}^{-1}$ and to $e = 0.3$ for a volume filling factor of 0.4 for velocities of $4 \text{ cm s}^{-1} \lesssim v_{\text{eff}} \lesssim 10 \text{ cm s}^{-1}$; (3) that the coefficient of restitution remains constant for higher velocities; (4) until fragmentation dominates for $v_{\text{eff}} \gtrsim 40 \pm 10 \text{ cm s}^{-1}$.

Our own numerical simulations, using the molecular-dynamics approach described in Seizinger et al. (2012), yield a reasonable match to the experimental data over the entire bouncing regime. We discussed the consequences of our results concerning PPDs, cold debris disks, and planetary rings.

We thank Evelyn Liebert, Hans-Georg Pietscher, and Heinrich Schmidt for their help in adjusting the laboratory drop tower to larger dust aggregates and for some test experiments. We thank Stephan Olliges and the Institut für Partikeltechnik at the TU-Braunschweig for performing the XRT measurements of our samples. This research was supported by the Deutsches Zentrum für Luft- und Raumfahrt under grant No. 50WM0936 and by the Deutsche Forschungsgemeinschaft (DFG) under grants BL 298/17 and KL 650/16, and within the collaborative research group FOR 759 *The formation of planets*. The simulations were performed on the bwGRiD cluster, which is funded by the Ministry for Education and Research of Germany and the Ministry for Science, Research and Arts of the state Baden-Württemberg.

REFERENCES

- Beitz, E., Güttler, C., Blum, J., et al. 2011, *ApJ*, 736, 34
 Dominik, C., & Tielens, A. G. G. M. 1995, *Phil. Mag. A*, 72, 783
 Dominik, C., & Tielens, A. G. G. M. 1996, *Phil. Mag. A*, 73, 1279
 Dominik, C., & Tielens, A. G. G. M. 1997, *ApJ*, 480, 647
 Eiroa, C., Marshall, J. P., Mora, A., et al. 2011, *A&A*, 536, L4
 Goldreich, P., & Tremaine, S. D. 1978, *Icarus*, 34, 227
 Gundlach, B., Kilias, S., Beitz, E., & Blum, J. 2011, *Icarus*, 214, 717
 Güttler, C., Blum, J., Zsom, A., Ormel, C. W., & Dullemond, C. P. 2010, *A&A*, 513, A56
 Güttler, C., Krause, M., Geretshausen, R. J., Speith, R., & Blum, J. 2009, *ApJ*, 701, 130
 Johansen, A., Brauer, F., Dullemond, C., Klahr, H., & Henning, T. 2008, *A&A*, 486, 597
 Johansen, A., Klahr, H., & Henning, T. 2006, *ApJ*, 636, 1121
 Johansen, A., Youdin, A. N., & Lithwick, Y. 2012, *A&A*, 537, A125
 Johnson, K. L., Kendall, K., & Roberts, A. D. 1971, *Proc. R. Soc. A*, 324, 301
 Klahr, H., & Bodenheimer, P. 2004, *Rev. Mex. Astron. Astrofis. Ser. Conf.*, 22, 87
 Kothe, S., Güttler, C., & Blum, J. 2010, *ApJ*, 725, 1242
 Poppe, T., Blum, J., & Henning, T. 2000, *ApJ*, 533, 454
 Poulet, F., & Cuzzi, J. N. 2002, *Icarus*, 160, 350
 Seizinger, A., Speith, R., & Kley, W. 2012, *A&A*, 541, A59
 Thornton, C., & Ning, Z. 1998, *Powder Technol.*, 99, 154
 Torquato, S., & Stillinger, F. H. 2010, *Rev. Mod. Phys.*, 82, 2633
 Wada, K., Tanaka, H., Suyama, T., Kimura, H., & Yamamoto, T. 2007, *ApJ*, 661, 320

Wada, K., Tanaka, H., Suyama, T., Kimura, H., & Yamamoto, T. 2011, *ApJ*, **737**, 36
Weidling, R., Güttler, C., & Blum, J. 2012, *Icarus*, **218**, 688
Wilner, D. J., Raman, A., Lisanti, M., Qi, C., & Hogerheijde, M. 2005, *BAAS*, **37**, 1224

Windmark, F., Birnstiel, T., Güttler, C., et al. 2012, *A&A*, **544**, L16
Youdin, A. N., & Goodman, J. 2005, *ApJ*, **620**, 459
Zebker, H. A., Marouf, E. A., & Tyler, G. L. 1985, *Icarus*, **64**, 531
Zsom, A., Ormel, C. W., Güttler, C., Blum, J., & Dullemond, C. P. 2010, *A&A*, **513**, A57

Bouncing behavior of microscopic dust aggregates

A. Seizinger and W. Kley

Institut für Astronomie und Astrophysik, Eberhard Karls Universität Tübingen, Auf der Morgenstelle 10c, 72076 Tübingen, Germany
e-mail: alexs@tat.physik.uni-tuebingen.de

Received 18 December 2012 / Accepted 14 January 2013

ABSTRACT

Context. Bouncing collisions of dust aggregates within the protoplanetary disk may have a significant impact on the growth process of planetesimals. Yet, the conditions that result in bouncing are not very well understood. Existing simulations studying the bouncing behavior used aggregates with an artificial, very regular internal structure.

Aims. Here, we study the bouncing behavior of sub-mm dust aggregates that are constructed applying different sample preparation methods. We analyze how the internal structure of the aggregate alters the collisional outcome and we determine the influence of aggregate size, porosity, collision velocity, and impact parameter.

Methods. We use molecular dynamics simulations where the individual aggregates are treated as spheres that are made up of several hundred thousand individual monomers. The simulations are run on graphic cards (GPUs).

Results. Statistical bulk properties and thus bouncing behavior of sub-mm dust aggregates depend heavily on the preparation method. In particular, there is no unique relation between the average volume filling factor and the coordination number of the aggregate. Realistic aggregates bounce only if their volume filling factor exceeds 0.5 and collision velocities are below 0.1 ms^{-1} .

Conclusions. For dust particles in the protoplanetary nebula we suggest that the bouncing barrier may not be such a strong handicap in the growth phase of dust agglomerates, at least in the size range of $\approx 100 \mu\text{m}$.

Key words. planets and satellites: formation – methods: numerical – protoplanetary disks

1. Introduction

For the planet formation process, the growth from micron-sized dust grains to kilometer-sized objects is a key ingredient of the core accretion scenario originally proposed by Pollack et al. (1996). Yet, the question remains unanswered how this process is accomplished in the face of various impediments. First of all, fast inward drift limits the time available to form planetesimals by successive collisions to less than 10^4 years (Weidenschilling 1977). The growth process itself heavily depends on two ingredients:

1. the dynamical properties of the disk that determine the collision rate as well as the parameters of a collision such as the impact velocity;
2. the mechanical behavior of the colliding aggregates that determines the outcome of the collision.

Since the information accessible through direct observations is limited, the first aspect is addressed mainly by theoretical work and computer simulations (Flaig et al. 2012). For an overview on the properties of protoplanetary disks, we refer to the following reviews by Dullemond et al. (2007) and Armitage (2011).

Various methods are employed to investigate the collision behavior of dust/icy aggregates. Depending on the size of the aggregates and the desired collision velocity, laboratory experiments are possible. As of today, laboratory experiments provide data of collisions ranging from millimeter- to decimeter-sized aggregates composed of different materials (mainly silicate/quartz and ice). A comprehensive summary of laboratory experiments is given by Blum & Wurm (2008). Computer simulations provide a second method to study the collisional behavior of dust or ice aggregates. Collisions of very small, micron-sized

aggregates have been simulated using a molecular dynamics approach (e.g., Dominik & Tielens 1997; Paszun & Dominik 2009; Wada et al. 2007, 2009). For macroscopic aggregates different methods such as smoothed-particle hydrodynamics (SPH) are employed (e.g., Schäfer et al. 2007; Geretshäuser et al. 2010).

More recent experiments showed that collisions of mm- to cm-sized aggregates often result in bouncing (e.g., Weidling et al. 2009; Heißelmann et al. 2010; Weidling et al. 2012; Jankowski et al. 2012). Extrapolating the results obtained from the various experiments, Güttler et al. (2010) devised a model describing the outcome of collision with respect to the collision velocity, and the mass and porosity of the colliding aggregates. Employing this model to simulate the evolution of a swarm of dust aggregates in a protoplanetary disk, the so called “bouncing barrier” emerged (Zsom et al. 2010). As the aggregates grow larger, their relative velocities increase. Because of the growing kinetic impact energy, aggregates get increasingly compacted during successive collisions. When the aggregates get too compact, their collisions do not result in sticking anymore. Instead, they bounce off each other and the growth process is stopped. This occurs in the size regime of centimeters.

A possible way to overcome the bouncing barrier has been recently suggested by Windmark et al. (2012a). Under the assumption of a few bigger aggregates that act as initial seeds, it is possible to grow 100 m-sized bodies on the timescale of 1 Myr. A possible origin of those seeds has been proposed by Windmark et al. (2012b). Taking into account a Maxwellian velocity distribution, they found that low velocity collisions can allow a few aggregates to grow considerably larger than the average of the simulated population.

Despite its significant influence on the growth process, bouncing still lacks theoretical understanding of its prerequisites

Table 1. Material parameters of the individual monomers used in the simulations.

Physical property	Silicate
Particle radius r (in μm)	0.6
Density ρ (in g cm^{-3})	2.65
Surface energy γ (in mJ m^{-2})	20
Young's modulus E (in GPa)	54
Poisson number ν	0.17
Critical rolling length ξ_{crit} (in nm)	2

on a microscopical scale. So far, molecular dynamics (MD) simulations result in bouncing only for compact aggregates (Wada et al. 2011; Schr apler et al. 2012). According to Wada et al. (2011) an average coordination number of 6 is required for aggregates to bounce off each other. However, in laboratory experiments bouncing was frequently observed in collisions of aggregates with lower filling factors/coordination numbers for which MD simulations clearly predict sticking. It has been speculated that this discrepancy could result from a size effect or a possible compaction of the outer shell during the handling process of the aggregates used in the laboratory experiments. However, the latter hypothesis has been refuted by recent experiments (Kothe et al. 2013).

The aim of this work is to study the influence of the internal structure on the bouncing behavior of sub-mm dust aggregates in greater detail. Using the enormous computing power provided by GPUs, we can simulate aggregates consisting of several hundreds of thousands of monomers and thus simulate aggregates in a size range from several microns up to ≈ 0.1 mm in diameter.

2. Interaction model

To simulate the behavior of dust aggregates we use a soft-sphere discrete element method (SSDEM) approach. The dust aggregates are composed of hundreds of thousands of micron-sized spherical grains (monomers). Our interaction model is based on the work of Dominik & Tielens (1997) who combined earlier theoretical work by Johnson et al. (1971); Dominik & Tielens (1995, 1996) into a detailed micro-mechanical model describing the interaction between two monomers. These monomers may establish adhesive contacts when touching each other and kinetic energy is dissipated upon deformation of these contacts. A few years later, Wada et al. (2007) presented a different approach when deriving nearly the same forces and torques from corresponding potentials.

When trying to reproduce the results of laboratory experiments performed by G uttler et al. (2009) on the compression of porous dust cakes, Seizinger et al. (2012) observed that the behavior predicted by the model of Dominik & Tielens (1997) was too soft. Since the samples used by G uttler et al. (2009) had been composed of micron-sized, spherical, monodisperse silicate grains their results constituted a perfect opportunity to calibrate the model. Introducing two free parameters m_r and m_s that modify the strength of the rolling and sliding interaction between two monomers, Seizinger et al. (2012) were able to obtain excellent agreement between the laboratory results and the computer simulations.

In this work we use the modified interaction model presented by Seizinger et al. (2012) with $m_r = 8$ and $m_s = 2.5$. The material parameters are listed in Table 1.

3. Sample generation

In this work we examine the conditions under which bouncing occurs. Apart from the external parameters describing the physics of collisions such as the impact parameter or velocity, we study the influence of the internal structure of the aggregate. Examples of such aggregates that have been generated by different methods are shown in Fig. 1.

To study the influence of the aggregate size, we use aggregates with diameters in the range of 30 to 100 μm . Unfortunately, simulations with larger aggregates are infeasible because of the required computational cost, at least for a wider range of parameters.

Typically, the volume filling factor ϕ and the average coordination number n_c are used to classify aggregates. In general, the filling factor is given by

$$\phi = \frac{NV_p}{V_A}, \quad (1)$$

where N denotes the number of monomers, V_p is the volume of a monomer, and V_A is the total volume occupied by the aggregate. As we use spherical aggregates, V_A can be calculated easily from the outer radius of the aggregate. For irregular-shaped aggregates there are different ways to define V_A . For example Kozasa et al. (1992) determine the size of a porous aggregate based on its radius of gyration, whereas Ossenkopf (1993) uses the geometric cross section. It is important to keep this ambiguity in mind when comparing the porosities of fluffy aggregates to results presented by other papers.

In molecular dynamics simulations, the coordination number of a monomer denotes the number of the neighbors it interacts with. Thus, the average coordination number n_c is obtained by averaging the number of contacts of each particle.

In this work we use three different types of aggregates: Hexagonal lattice aggregates featuring a regular grid structure, aggregates produced by slowly compacting a porous dust cake, and aggregates generated by successively adding single monomers from randomly chosen directions. These choices were motivated by the fact that hexagonal lattice aggregates are easy to build and allow for comparison with earlier work by Wada et al. (2011), whereas the static compaction resembles the generation of samples used in laboratory results. The aggregates of the third type are generated algorithmically, but their structure remains comparable to the static-compaction type (see Sect. 3.4). Because the aggregates within the protoplanetary nebula grow through successive collisions one might expect that their internal structure lies somewhere in between the static-compression and the ballistic-aggregation cases.

3.1. Hexagonal lattice (CPE)

Hexagonal-lattice type aggregates, also referred to as hexagonal close packing with extraction (CPE), can be generated very easily. First, a hexagonal close-packing aggregate is generated which features a volume filling factor $\phi \approx 0.74$ and a coordination number $n_c \approx 12$ (because of surface effects n_c equals 12 only for aggregates of infinite size). In the second step, a suitable number of randomly selected monomers will be removed to achieve the desired volume filling factor. As a result, a small number of monomers on the surface may become disconnected from the main aggregate and will be removed as well.

Wada et al. (2011) have already studied the bouncing behavior of these aggregates and found that bouncing will occur if the

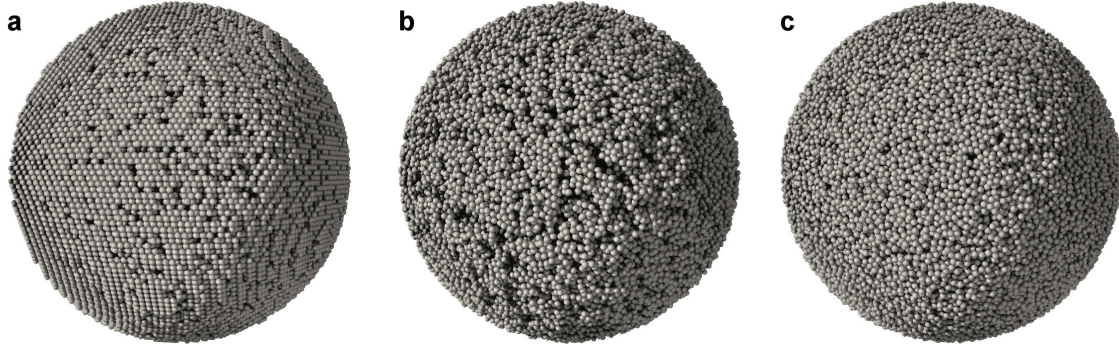


Fig. 1. Examples of the different types of aggregates used in this work: **a)** hexagonal lattice $\phi = 0.59$, $n_c = 9.93$; **b)** ballistic aggregation with migration $\phi = 0.40$, $n_c = 3.98$; and **c)** static compaction $\phi = 0.49$, $n_c = 3.50$. All depicted spheres have a diameter of $60 \mu\text{m}$.

average coordination number is greater than 6. Schr apler et al. (2012) analyzed the relation between the coefficient of restitution and the collision velocity in experiments and simulations using CPE aggregates. Their results agreed well with a theoretical model by Thornton & Ning (1998).

3.2. Ballistic aggregation with migration (BAM)

The second type of aggregates was originally suggested by Shen et al. (2008) and also studied in the work of Wada et al. (2011). To generate a larger aggregate, single monomers are successively shot in from random directions onto the existing aggregate. When the monomer hits the aggregate it will either remain at the position where the first contact was established or it will migrate to a position close by where it establishes contacts with two or three monomers. Compared to Shen et al. (2008), we use three different methods to select the final position of the migrating particle:

1. select the position closest to the spot where the monomer impacts on the aggregate (referred to as “shortest migration”);
2. select the position randomly from all available possibilities (referred to as “random migration”);
3. select the position which is closest to the center of mass (referred to as “center migration”).

For a given coordination number, the resulting aggregates show a different filling factor depending on which selection mechanism is employed (see Fig. 2). The first method leads to the most porous aggregates since the monomers typically migrate to positions farther outward compared to the case of random migration. The resulting aggregates will become even more compact if monomers migrate to the most inward position available.

Note that we do not claim that random and center migration are realistic growth processes that accurately describe the growth of dust aggregates in protoplanetary discs. Yet, they constitute a computationally very cheap approach to generate larger aggregates that do not suffer from the artificial lattice structure like the CPE aggregates described above. Compared to the static-compaction aggregates they offer the additional advantage of being perfectly relaxed. Since all monomers are at equilibrium distance from each other, there are no attractive or repulsive forces that could lead to a breakup of the aggregate.

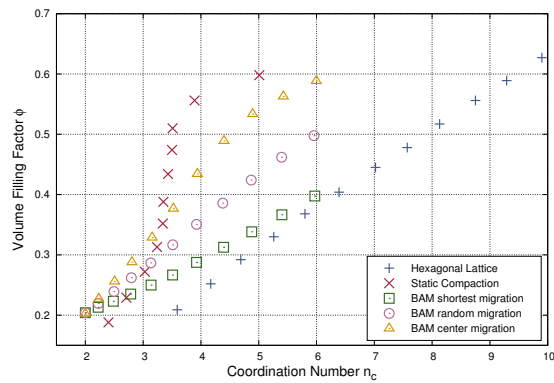


Fig. 2. The relation between the volume filling factor ϕ and the average coordination number n_c . All aggregates are spherical and have a diameter of $60 \mu\text{m}$.

3.3. Static compaction (SC)

The last type of aggregates used for our studies is the most computationally expensive. To generate a spherical aggregate of a certain diameter we start with a sufficiently large, cuboid-shaped dust cake generated by random ballistic deposition (RBD). Since RBD aggregates feature an initial volume filling factor of $\phi = 0.15$, we first have to compact the aggregate until we reach the desired filling factor. For this purpose, the aggregate is put into a box with walls that can move toward each other. According to Seizinger et al. (2012) this compaction must be very slow to prevent inhomogeneities.

Even if the cake is compacted homogeneously for filling factors above ≈ 0.45 , it will become elastically charged and expand when the compacting walls are removed. Therefore, the dust cake needs to be relaxed before removing the walls of the compaction box. For this purpose, we disturb the aggregate by modifying the position of the monomers randomly by a very small amount. We keep the disturbed aggregate in a box of fixed size and wait until the kinetic energy induced by the disturbance is damped away by the inelastic monomer interaction. To eliminate kinetic energy below the threshold where the inelastic regime is entered, we additionally enforce a viscous damping mechanism. For this purpose, the velocities and angular velocities of

the monomers are multiplied by a factor of $1-\kappa$ in each time step, where κ denotes a damping coefficient. In this work we use $\kappa = 0.0001$.

It turns out that a maximum disturbance of a factor of 0.001 to the radius of a monomer is sufficient to stabilize the aggregate without altering its internal structure. Higher values may alter the coordination number significantly which could potentially change the collisional behavior of the aggregates and is therefore unwanted. For filling factors above $\phi = 0.58$ – 0.59 this method no longer works because the compaction is too close to the random closest packing ($\phi \approx 0.63$) and no stable configuration can be reached without rearranging the monomers significantly.

After the aggregate has been relaxed the compaction box is removed and a spherical aggregate will be cut out of the compacted cake. As this procedure is computationally very expensive, it takes several days to generate larger ($50 \mu\text{m}$ in diameter and above) aggregates of this type.

3.4. Comparison

Comparing the relation between ϕ and n_c of the different types of aggregates described above shows very interesting features. As we can see in Fig. 2, the relation depends considerably on the preparation method. The different BAM generation methods have been described in Sect. 3.2.

From the work presented in this section two important conclusions can be drawn:

1. the coordination number n_c is not sufficient to describe the properties of an aggregate. Especially, there is no unambiguous relation $\phi(n_c)$ between filling factor and coordination number;
2. hexagonal lattice (CPE) aggregates have a distinct relation $\phi(n_c)$ compared to the other two methods that produce aggregates with less artificial structures.

In laboratory experiments with aggregates composed of micron-sized dust grains, it is typically only possible to determine the filling factor but not the coordination number. Thus, one has to be very careful when comparing results from numerical simulations of CPE aggregates with results from laboratory experiments.

4. Results

In this section we present our results from various simulations in which we study the influence of the collision velocity, impact parameter, and aggregate size on the bouncing behavior. All simulations were performed on NVIDIA GPUs (GTX460, GTX570, Tesla C2070). Depending on the aggregate size and filling factor, each simulation took between less than an hour and half a day.

4.1. Growth factor

In the following bouncing maps the “growth factor” γ that is inspired by the four-population model suggested by Geretshausner et al. (2011) is depicted. It is defined by

$$\gamma = \frac{m_{\text{largest}}}{m_{\text{tot}}}, \quad (2)$$

where m_{largest} is the mass of the largest fragment and m_{tot} the total mass of the colliding aggregates. For perfect sticking we obtain $\gamma = 1$, for total destruction $\gamma \rightarrow 0$. In collisions of aggregates of equal size, a value $\gamma = 0.5$ indicates bouncing. However, during

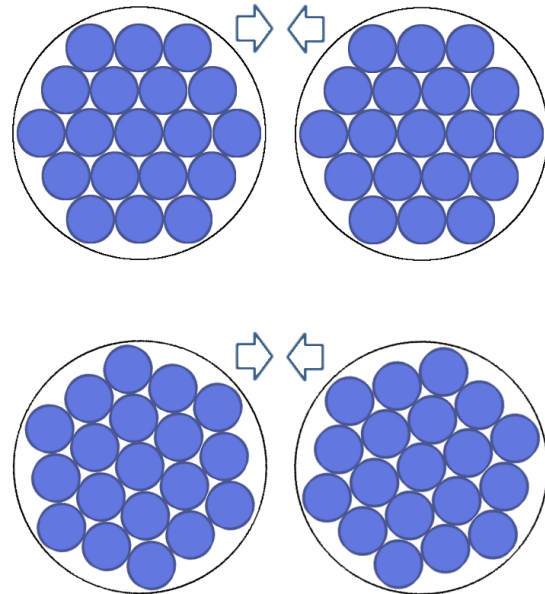


Fig. 3. Schematic view of the possible alignment of two CPE aggregates. In the upper case the aggregates are oriented with respect to their lattice structure. In the lower case the orientation is arbitrary.

the transition from perfect sticking to fragmentation γ may also become 0.5. To distinguish between the two cases we consider the mass ratio γ_2 of the second largest fragment. In the bouncing case $\gamma = \gamma_2 = 0.5$ whereas in the fragmentation case the mass of the second largest fragment is much lower than 0.5 of the total mass as there are a lot of other smaller fragments.

Thus, in the bouncing maps presented in this work the green areas indicate sticking, the upper left yellow areas bouncing, and the color gradient from green to yellow to red on the right marks the transition from sticking to fragmentation.

Note that $\gamma = \gamma_2 = 0.5$ only applies in the case of “perfect bouncing”. In our simulations we often observe the loss of a few monomers (typically less than 100), which is negligible compared to the total number of monomers of 5×10^4 to 5×10^5 . Thus, we also count collisions as bouncing events if γ and γ_2 are slightly smaller than 0.5.

4.2. Hexagonal lattice

The outcome of head-on collisions of CPE aggregates has already been studied by Wada et al. (2011) who observed bouncing if the coordination number was greater than 6. However, their aggregates were much smaller ($\approx 10^4$ monomers). Since hexagonal-lattice aggregates feature a regular lattice structure, their orientation is likely to influence the collision behavior. Thus, we first examine the effect of the orientation by comparing the case where the aggregates are aligned to their lattice structure (see upper part of Fig. 3) with a random orientation (lower part of Fig. 3). As we can see in Fig. 4, the orientation of the aggregates is important especially for the transition from sticking to bouncing with increasing filling factor. Looking at the left panel of Fig. 4 and comparing the filling factor with the coordination number in Fig. 2 we can reproduce the $n_c \geq 6$ -criterion proposed by Wada et al. (2011) for the aligned case. On the other hand, the

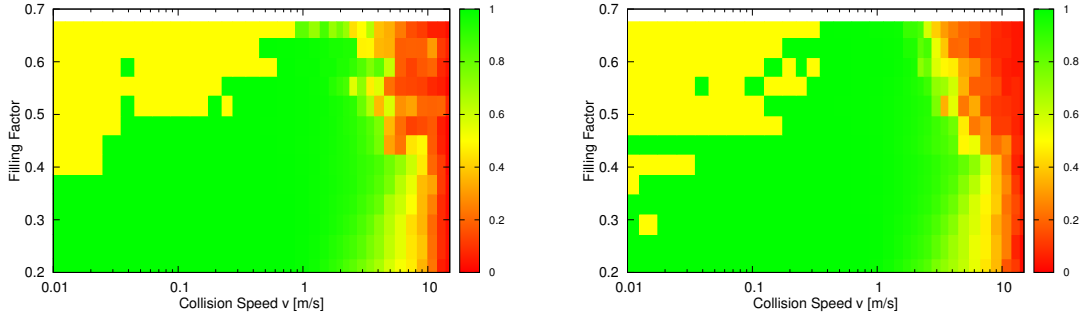


Fig. 4. Growth factor γ (Eq. (2)) of the collision of two CPE aggregates with a diameter of $60 \mu\text{m}$. Sticking occurs in the green area, whereas the yellow area in the upper left indicates bouncing. *Left:* orientation aligned to the lattice structure of the aggregates. *Right:* non-aligned orientation.

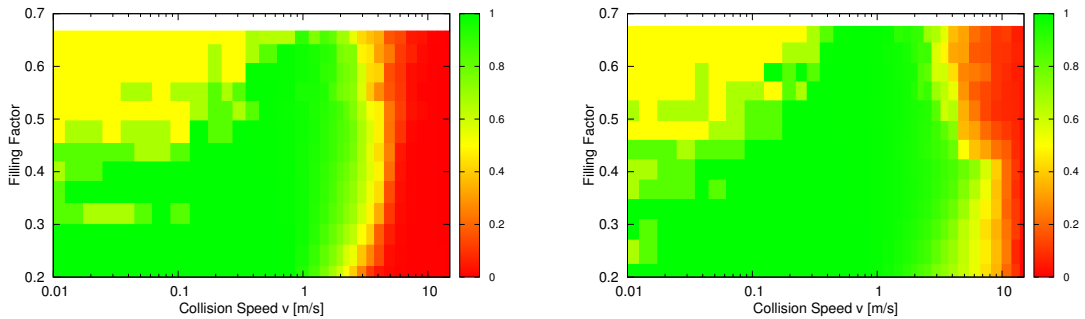


Fig. 5. Growth factor of the collision of two CPE aggregates of different size averaged over three different orientations. *Left:* aggregates of a diameter of $30 \mu\text{m}$. *Right:* aggregates of a diameter of $60 \mu\text{m}$.

bouncing map differs significantly for a non-aligned orientation (see right panel of Fig. 4).

In order to mitigate the effect of the orientation we averaged over three different orientations to investigate the size dependency of our results. Each map was generated using 12 different filling factors and 28 velocities. Thus, $3 \times 336 = 1008$ simulations had to be performed in total. Concerning bouncing, we could not observe a clear difference between aggregates with a diameter of 30 and $60 \mu\text{m}$ (see Fig. 5).

However, the velocity $v_{s \rightarrow f}$ at which the transition from sticking to fragmentation occurs changes significantly. For the small aggregates we get $v_{s \rightarrow f} \approx 4 \text{ ms}^{-1}$ (left panel of Fig. 5). For the bigger aggregates we observe that $v_{s \rightarrow f}$ depends on the filling factor. For $\phi < 0.43$ we find that $v_{s \rightarrow f} \approx 10 \text{ ms}^{-1}$, whereas for $\phi > 0.43$ $v_{s \rightarrow f} \approx 5 \text{ ms}^{-1}$ (right panel of Fig. 5). This can be explained by the reduced capability of compact aggregates to dissipate kinetic energy by restructuring. Taking into account Fig. 2, we see that the transition occurs when the average coordination number n_c exceeds a value of 6. A monomer with six or more contacts is fixated tightly and thus the aggregate can no longer change its internal structure as easily.

In summary, it can be said that for hexagonal lattice aggregates we regularly observe bouncing collisions for filling factors above 0.5 and for collision velocities up to roughly 0.2 ms^{-1} .

4.3. Ballistic aggregation with migration

Wada et al. (2011) found that bouncing may occur if $n_c \geq 6$ independent of the type of aggregate they used. In Fig. 6 we show

the outcome of collisions between two roughly $75 \mu\text{m}$ -sized BAM aggregates generated using the shortest migration method described in Sect. 3.2. The corresponding filling factor is between 0.36 and 0.39, however, we observed only two bouncing collisions. Since $n_c = 6$ is the maximum value that can be achieved by two time migration, we could not investigate what happens at higher coordination numbers.

We repeated the shortest-migration setup described above, but this time for center migration case and we obtained similar results as for the shortest-migration case shown in Fig. 6. We observe hardly any bouncing events even for aggregates with $n_c = 6$ (which corresponds to a filling factor of 0.49–0.5). This indicates that the bouncing behavior of BAM aggregates depends more on the filling factor than on the coordination number.

To achieve higher filling factors we switched to the center migration method (see Sect. 3.2). The corresponding bouncing maps are shown in Fig. 7. It is striking that the bouncing regime is much smaller compared to the CPE aggregates. As before, the transition from sticking to fragmentation occurs at higher velocities for larger aggregates.

4.4. Static compaction

The bouncing behavior of the aggregates generated by static compaction is quite similar to the bouncing behavior of BAM aggregates (see Fig. 8). Again, the bouncing regime is considerably smaller compared to the case of hexagonal lattice aggregates and bouncing is observed only in some cases for high filling factors above 0.5 and collision velocities below 0.1 ms^{-1} .

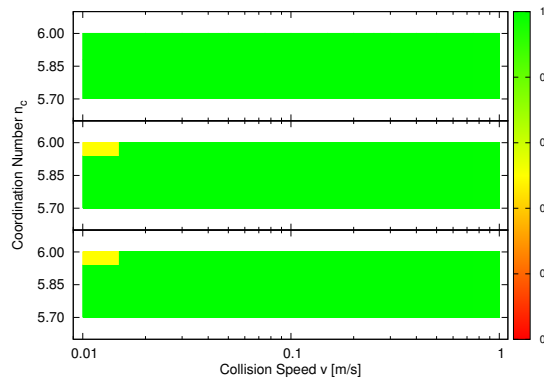


Fig. 6. Growth factor of the collision of two BAM aggregates generated using the shortest migration method. For three different aggregates of a diameter of roughly $75 \mu\text{m}$ only two collisions at 1 cm s^{-1} lead to bouncing.

As in the case of the other aggregate types, the transition velocity $v_{s \rightarrow f}$ from sticking to fragmentation increases with increasing aggregate size. For the the small aggregates with $d = 30 \mu\text{m}$ we observe $v_{s \rightarrow f} \approx 4 \text{ ms}^{-1}$, whereas for $d = 60 \mu\text{m}$ the transition velocity goes up to $v_{s \rightarrow f} \approx 12 \text{ ms}^{-1}$.

4.5. Size dependency

To further examine the influence of the aggregate size we performed collisions of $100 \mu\text{m}$ -sized CPE and BAM aggregates (using the center migration method because it yields the BAM aggregates with the highest filling factors). For the CPE aggregates we observe slightly more bouncing for filling factors between 0.4 to 0.5 (see left panel of Fig. 9). However, for BAM aggregates there is no noticeable difference compared to the $60 \mu\text{m}$ aggregates (see right panel of Fig. 9).

Depending on the filling factor, the $100 \mu\text{m}$ aggregates consist of up to 350 000 monomers. In order to analyze the size dependency it would be desirable to simulate collisions of even larger aggregates. Unfortunately, this is rendered impossible by the lack of available computing power. Simulating a single collision of two $100 \mu\text{m}$ -sized aggregates took 10 to 20 h (owing to the different filling factors) on a GPU. Doubling the size would require computing times on the order of weeks for a single collision. For each orientation shown in Fig. 9, 48 collisions were performed.

4.6. Impact parameter

As a last step we examine the influence of the impact parameter $b = 0.5$. For the collisions, we used the same orientation as for the results shown in the right panel of Fig. 4. Contrary to our expectations, we do not observe a significant influence of the impact parameter on the bouncing behavior of CPE aggregates (see Fig. 10). However, fragmentation sets in at considerably lower velocities of $v_{s \rightarrow f} \approx 3 \text{ ms}^{-1}$. In a head on collision the entire aggregate can dissipate the kinetic impact energy by internal restructuring which helps to prevent fragmentation. This does not apply to offset collisions where it is easier to tear away the outer layers without major restructuring of the core of the aggregates. However, comparing the growth map of the

collisions between aggregates with a diameter of 30 and $60 \mu\text{m}$ we do not observe any significant increase of velocity $v_{s \rightarrow f}$ where the transition from sticking to fragmentation occurs (see left and right panels of Fig. 10). As already pointed out by Wada et al. (2009) the increase of $v_{s \rightarrow f}$ for larger aggregates is limited to the case of head-on collisions.

In contrast, for BAM aggregates we do observe bouncing in a larger regime compared to the case of head-on collisions (see Fig. 11). Again, the same samples and orientation as for the head-on collisions (right panel of Fig. 7) were used.

5. Requirements for bouncing

Compared to the aggregates generated by BAM or static compaction, the bouncing regime of CPE aggregates is significantly larger. A likely explanation for this discrepancy is given by the different structure of the aggregates. To gain a deeper insight into the physical processes leading to sticking or bouncing, it is worthwhile to have a closer look at a single collision.

Two aggregates can bounce off each other only if there is enough elastic energy left to break the contact area. Thus, a significant amount of the kinetic impact energy must be stored temporarily without being dissipated. If the colliding aggregates penetrate each other too deeply, the impact energy is dissipated upon internal restructuring in the area where the contact is established. In this case inelastic sliding and rolling constitute the main dissipation channels (Wada et al. 2011). Thus, the ratio of elastic to dissipated energy of colliding aggregates is the key parameter that determines whether sticking or bouncing will occur.

Being able to track the evolution of the different types of energies over time is the key advantage of the model presented by Wada et al. (2007). To address the different behavior of BAM and CPE aggregates we compare a bouncing collision of two CPE aggregates with a sticking collision of BAM aggregates. Both aggregates are $60 \mu\text{m}$ in diameter and have a filling factor $\phi \approx 0.59$. The time evolution of different types of energies and potentials for these collisions is shown in Fig. 12.

As expected, when sticking occurs most of the kinetic energy is dissipated by inelastic sliding and rolling (right panel of Fig. 12). Only a small percentage of the impact energy is stored in the elastic regime of the normal U_{normal} and sliding potential U_{slide} (since the elastic energy stored in the rolling and twisting potentials is negligible they are not shown in Fig. 12).

We observe an entirely different situation when bouncing occurs. As shown in the left panel of Fig. 12, only about one third of the impact energy is dissipated, while roughly half of the kinetic energy is temporarily converted into potential energy. This coincides well with our predictions above. The potential energy that is stored mainly in the normal and sliding interaction is converted back into kinetic energy and allows the colliding aggregates to separate again.

We can conclude that owing to their lattice structure, CPE aggregates can convert significantly more impact energy into elastic energy than BAM aggregates. In a compact CPE aggregate the monomers are located in densely packed layers. When the outer monomer of such a layer hits the other aggregate it is pushed inwards and will compress the layer. In this way, kinetic energy is converted into potential energy without the occurrence of inelastic restructuring. This mechanism works well in the presence of a regular grid structure which is the case for CPE aggregates. However, the monomers of BAM aggregates are not arranged in any regular pattern. Thus, they are not likely to bounce unless they are very compact in which case

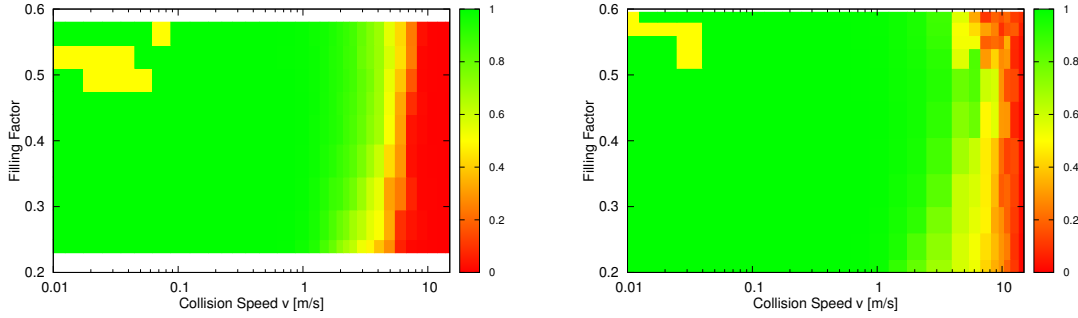


Fig. 7. Growth factor of the collision of two BAM aggregates of different size generated using the center migration method. *Left:* diameter of $30 \mu\text{m}$. *Right:* diameter of $60 \mu\text{m}$.

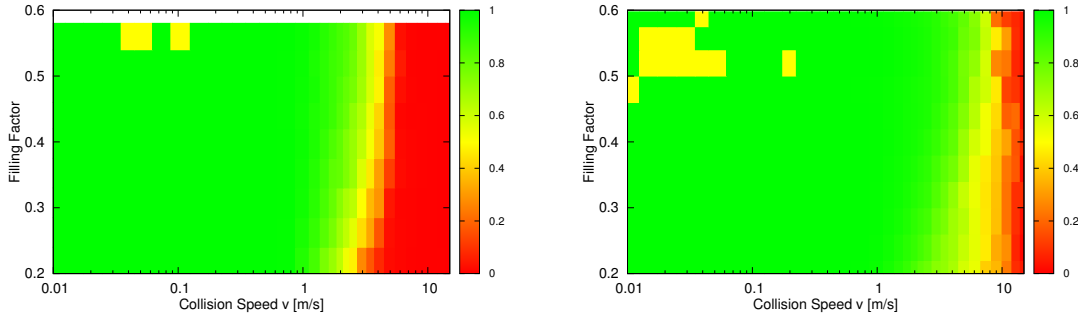


Fig. 8. Growth factor of the collision of two static-compaction aggregates of different size. *Left:* diameter of $30 \mu\text{m}$. *Right:* diameter of $60 \mu\text{m}$.

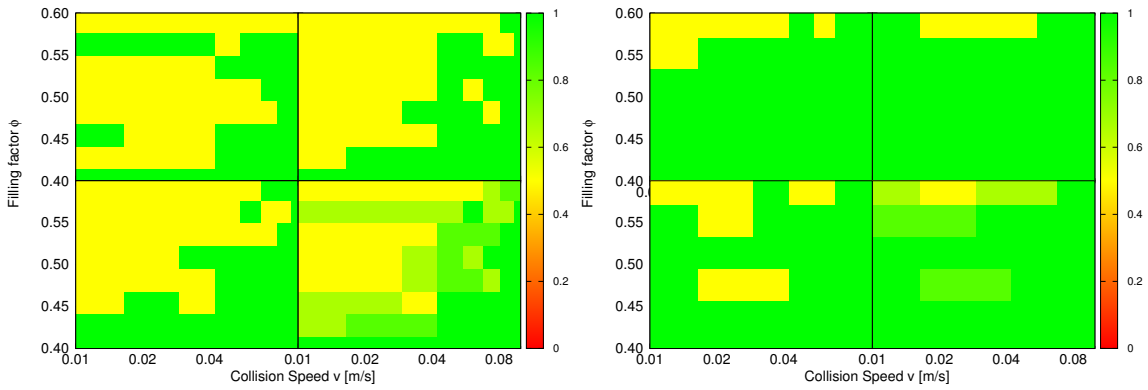


Fig. 9. Growth factor of the collision of two aggregates with a diameter of $100 \mu\text{m}$ for three different orientations. The plot on the *bottom right* of both panels shows the values averaged over the three orientations. *Left:* CPE aggregates. *Right:* BAM aggregates (center migration).

energy dissipation by internal restructuring is hindered because the monomers are locked in their position.

It also offers an explanation for the lower impact velocity of BAM aggregates at which we observe the transition from bouncing to sticking. At impact velocities above 0.1 ms^{-1} , the kinetic impact energy is sufficient to restructure the monomers in the contact area that had been locked at lower impact velocities. Since the lattice structure of CPE aggregates offers higher

resistivity against restructuring, their transition velocity from bouncing to sticking is roughly 0.3 ms^{-1} .

6. Conclusions

From the analysis of the statistical properties of the different samples presented in Sect. 3 we clearly see that the method of preparation plays a crucial role when studying the collisional

A&A 551, A65 (2013)

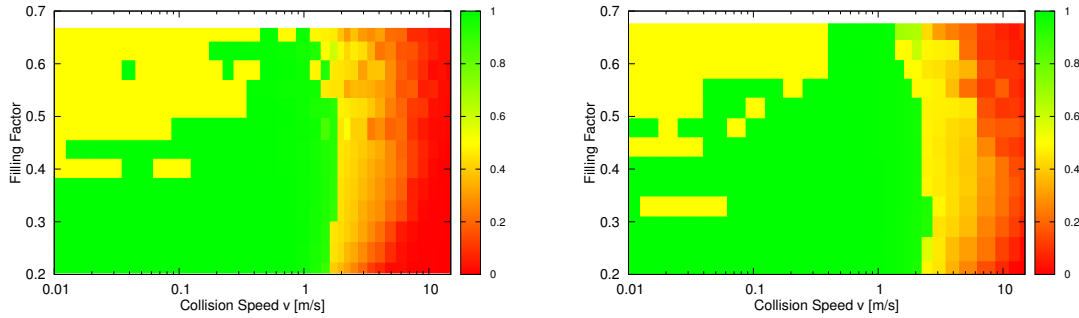


Fig. 10. Growth factor of the collision of two CPE aggregates with an impact parameter $b = 0.5$. *Left:* aggregates with a diameter of $30 \mu\text{m}$. *Right:* aggregates with a diameter of $60 \mu\text{m}$.

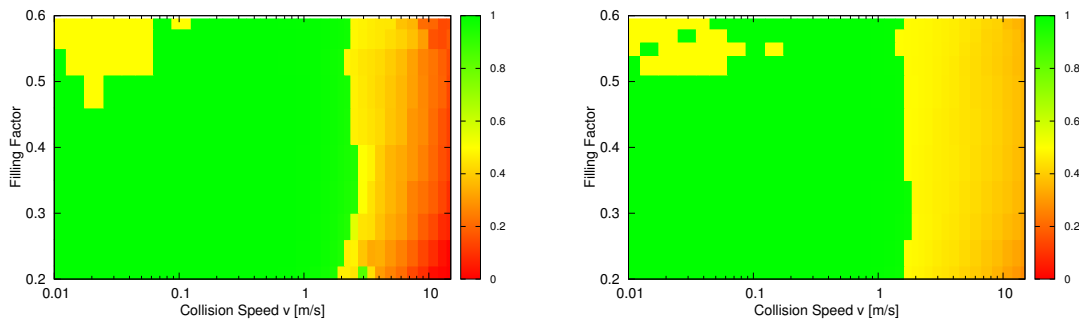


Fig. 11. Growth factor of the offset collisions of two $60 \mu\text{m}$ -sized BAM aggregates. *Left:* impact parameter $b = 0.5$. *Right:* impact parameter $b = 0.75$.

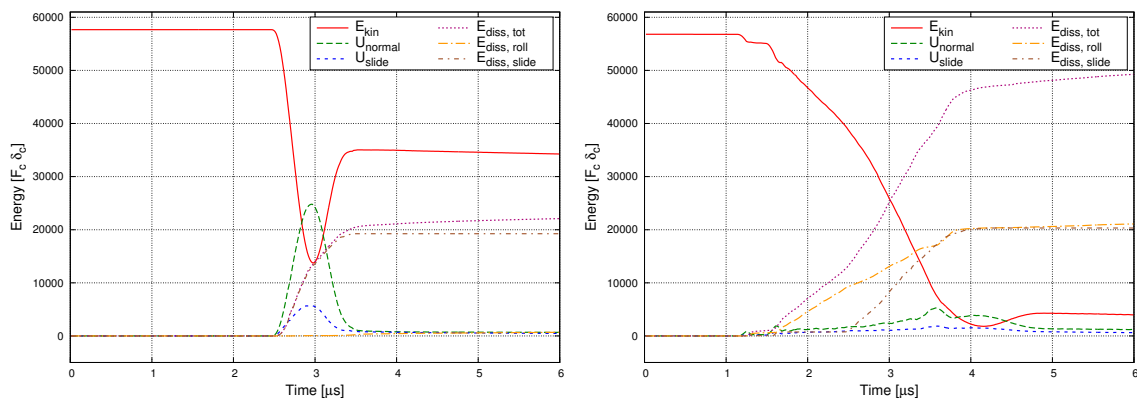


Fig. 12. Time evolution of the kinetic, potential, and dissipated energy during collisions of two aggregates with a diameter of $60 \mu\text{m}$ and filling factor $\phi \approx 0.59$. *Left:* a bouncing collision between two CPE aggregates. A sufficient amount of the impact energy is temporarily stored in the potential U_{normal} of the normal interaction. *Right:* during a sticking collision of two BAM aggregates most of the kinetic impact energy is dissipated.

behavior of microscopic dust aggregates. As the relation between the volume filling factor and the average coordination number strongly depends on the method of preparation, one must be careful when comparing results obtained from computer simulations with results obtained from laboratory work. In most laboratory experiments, only the volume filling factor can be measured, while the equally important coordination number remains unknown. Since the more compact aggregates used in laboratory experiments are typically produced by mechanical compression,

we expect that their microscopic structure resembles the static compaction aggregates much more closely than the hexagonal lattice type aggregates.

For computer simulations, generating large, compact aggregates by static compaction is infeasible because of the additional computational effort. We suggest using BAM aggregates as an alternative. Their statistical properties are close to the aggregates produced by static compaction, yet they can be generated directly. Additionally, one does not run into problems caused by

elastic charging as the generation procedure ensures that BAM aggregates are perfectly relaxed. At least in the various collision simulations performed in this work, BAM and static compaction aggregates show very similar behavior.

Based on the outcome of the simulations presented in this work, we can conclude that bouncing collisions of dust aggregates in the size regime below 0.1 mm are rare. Unless the aggregates feature a regular lattice structure, which is not likely to be the case for the aggregates in a protoplanetary disk, bouncing requires filling factors greater than 0.5 and collision velocities below 0.1 ms^{-1} . Even if these prerequisites are met, bouncing does not occur very frequently. Additionally, laboratory experiments on dust growth show that the maximum filling factor that is achieved during the growth process is much lower than $\phi = 0.5$ (e.g., Teiser et al. 2011). Therefore, the influence of bouncing on the growth process is limited in the sub-mm size regime.

Hence, from a microscopic view it remains unclear how cm-sized aggregates with filling factors considerably below 0.5 are able to bounce off each other. The idea of a compacted outer layer (also referred to as a hard shell) has been put forward as a possible explanation. Using SPH simulations, Geretshauser et al. (in prep.) observed that a hard shell can indeed lead to bouncing collisions between aggregates with a porous core. Wada et al. (2011) obtained similar results when performing molecular dynamics simulations of collisions of CPE aggregates featuring a hard sphere. Langkowski et al. (2008) found that molding an aggregate significantly alters the outcome of a collision experiment. However, Kothe et al. (2013) analyzed aggregates used in their collision experiments with X-ray computer tomography imaging and could not find any compacted outer layers.

In Sect. 4.6 we have shown that offset collisions result in bouncing somewhat more often than head-on collisions do. Depending on the experimental setup, head-on collisions will be rare, and in a setup featuring free collision with many particles head-on collisions will be rare as well (e.g., Weidling et al. 2012; Beitz et al. 2012). Thus, the impact parameter helps to resolve some of the discrepancies between numerical simulations and laboratory experiments.

Taking into account the different aggregate types we can only partially confirm the $n_c \geq 6$ criterion for bouncing proposed by Wada et al. (2011). It agrees well with our results from collisions of CPE aggregates. However, for BAM aggregates generated by the shortest migration method we observe very little bouncing at $n_c = 6$ (see Sect. 4.3 and Fig. 6). Likewise, for static-compaction aggregates or BAM aggregates generated by the random or center migration method there are a few bouncing events where n_c is considerably lower than 6. A volume filling factor of $\phi \approx 0.5$ appears to constitute a lower limit for bouncing. At the present time we do not have an explanation for what determines the exact value of the critical filling factor for the onset of bouncing. We have shown that it depends on the amount of energy that can be stored in the normal potential. The energy deposition is a continuous process, and it is to be expected that below a certain density sticking ensues. Numerically, we determined this value to be $\phi \approx 0.5$ in the sub-mm size regime.

Our simulations give insight into the fragmentation threshold as well. For small aggregates ($30 \mu\text{m}$) the fragmentation velocity is around 4 m/s. Upon increasing the projectile size the fragmentation threshold increases to about 10 m/s for the largest particle sizes we considered ($60 \mu\text{m}$), and this is independent of the sample generation method. This value is in very good agreement with the findings of SPH simulation for much larger objects (Geretshauser et al. 2011). The shift to a larger

fragmentation velocity is caused by the ability of larger particles to dissipate more kinetic energy. Upon increasing the filling factor, the fragmentation threshold decreases because the aggregates become much stiffer and cannot be deformed so easily. However, as shown in Sect. 4.6, this effect only applies to the case of head-on collisions.

With respect to the growth of small dust agglomerates in the protoplanetary nebula, our results indicate that for more realistic aggregates (BAM-type) bouncing only occurs for very small collision velocities ($<0.1 \text{ m/s}$) and large filling factors >0.5 . Thus, the bouncing barrier may not be such a strong handicap in the growth phase of dust agglomerates, at least in the size range of $\approx 100 \mu\text{m}$. For larger, m -sized particles SPH results indicate bouncing up to 1 m/s.

Acknowledgements. A. Seizinger acknowledges the support through the German Research Foundation (DFG) grant KL 650/16. The authors acknowledge support through DFG grant KL 650/7 within the collaborative research group FOR 759 *The formation of planets*. We also thank the referee, Koji Wada, for his helpful comments that improved the quality of this paper. A part of the simulations were performed on the bwGRiD cluster, which is funded by the Ministry for Education, and Research of Germany and the Ministry for Science, Research and Arts of the state of Baden-Württemberg.

References

- Armitage, P. J. 2011, *ARA&A*, 49, 195
 Beitz, E., Güttler, C., Weidling, R., & Blum, J. 2012, *Icarus*, 218, 701
 Blum, J., & Wurm, G. 2008, *ARA&A*, 46, 21
 Dominik, C., & Tielens, A. G. G. M. 1995, *Philos. Mag., Part A*, 72, 783
 Dominik, C., & Tielens, A. G. G. M. 1996, *Philos. Mag., Part A*, 73, 1279
 Dominik, C., & Tielens, A. G. G. M. 1997, *ApJ*, 480, 647
 Dullemond, C. P., Hollenbach, D., Kamp, I., & D'Alessio, P. 2007, *Protostars and Planets V*, 555
 Flaig, M., Ruoff, P., Kley, W., & Kissmann, R. 2012, *MNRAS*, 420, 2419
 Geretshauser, R. J., Speith, R., Güttler, C., Krause, M., & Blum, J. 2010, *A&A*, 513, A58
 Geretshauser, R. J., Meru, F., Speith, R., & Kley, W. 2011, *A&A*, 531, A166
 Güttler, C., Krause, M., Geretshauser, R. J., Speith, R., & Blum, J. 2009, *ApJ*, 701, 130
 Güttler, C., Blum, J., Zsom, A., Ormel, C. W., & Dullemond, C. P. 2010, *A&A*, 513, A56
 Heißelmann, D., Blum, J., Fraser, H. J., & Wölling, K. 2010, *Icarus*, 206, 424
 Jankowski, T., Wurm, G., Kelling, T., et al. 2012, *A&A*, 542, A80
 Johnson, K. L., Kendall, K., & Roberts, A. D. 1971, *Roy. Soc. London Proc. Ser. A*, 324, 301
 Kothe, S., Blum, J., Weidling, R., & Güttler, C. 2013, *Icarus*, submitted
 Kozasa, T., Blum, J., & Mukai, T. 1992, *A&A*, 263, 423
 Langkowski, D., Teiser, J., & Blum, J. 2008, *ApJ*, 675, 764
 Ossenkopf, V. 1993, *A&A*, 280, 617
 Paszun, D., & Dominik, C. 2009, *A&A*, 507, 1023
 Pollack, J. B., Hubickyj, O., Bodenheimer, P., et al. 1996, *Icarus*, 124, 62
 Schäfer, C., Speith, R., & Kley, W. 2007, *A&A*, 470, 733
 Schräpler, R., Blum, J., Seizinger, A., & Kley, W. 2012, *ApJ*, 758, 35
 Seizinger, A., Speith, R., & Kley, W. 2012, *A&A*, 541, A59
 Shen, Y., Draine, B. T., & Johnson, E. T. 2008, *ApJ*, 689, 260
 Teiser, J., Engelhardt, I., & Wurm, G. 2011, *ApJ*, 742, 5
 Thornton, C., & Ning, Z. 1998, *Powder Technol.*, 99, 154
 Wada, K., Tanaka, H., Suyama, T., Kimura, H., & Yamamoto, T. 2007, *ApJ*, 661, 320
 Wada, K., Tanaka, H., Suyama, T., Kimura, H., & Yamamoto, T. 2009, *ApJ*, 702, 1490
 Wada, K., Tanaka, H., Suyama, T., Kimura, H., & Yamamoto, T. 2011, *ApJ*, 737, 36
 Weidenschilling, S. J. 1977, *MNRAS*, 180, 57
 Weidling, R., Güttler, C., Blum, J., & Brauer, F. 2009, *ApJ*, 696, 2036
 Weidling, R., Güttler, C., & Blum, J. 2012, *Icarus*, 218, 688
 Windmark, F., Birnstiel, T., Güttler, C. 2012a, *A&A*, 540, A73
 Windmark, F., Birnstiel, T., Ormel, C. W., & Dullemond, C. P. 2012b, *A&A*, 544, L16
 Zsom, A., Ormel, C. W., Güttler, C., Blum, J., & Dullemond, C. P. 2010, *A&A*, 513, A57

Tensile & shear strength of porous dust agglomerates

A. Seizinger,¹ R. Speith,² and W. Kley¹

¹ Institut für Astronomie und Astrophysik, Eberhard Karls Universität Tübingen,
Auf der Morgenstelle 10, D-72076 Tübingen, Germany
e-mail: alexs@tat.physik.uni-tuebingen.de

² Physikalisches Institut, Eberhard Karls Universität Tübingen,
Auf der Morgenstelle 14, D-72076 Tübingen, Germany

Received 10.06.2013; accepted 23.08.2013

ABSTRACT

Context. Within the sequential accretion scenario of planet formation, planets are built up through a sequence of sticking collisions. The outcome of collisions between porous dust aggregates is very important for the growth from very small dust particles to planetesimals. In this work we determine the necessary material properties of dust aggregates as a function of porosity.

Aims. Continuum models such as SPH that are capable of simulating collisions of macroscopic dust aggregates require a set of material parameters. Some of them, such as the tensile and shear strength, are difficult to obtain from laboratory experiments. The aim of this work is to determine these parameters from ab initio molecular dynamics simulations.

Methods. We simulated the behavior of porous dust aggregates using a detailed micro-physical model of the interaction of spherical grains that includes adhesion forces, rolling, twisting, and sliding. Using different methods of preparing the samples, we studied the strength behavior of our samples with varying porosity and coordination number of the material.

Results. For the tensile strength, we can reproduce data from laboratory experiments very well. For the shear strength, there are no experimental data available. The results from our simulations differ significantly from previous theoretical models, which indicates that the latter might not be sufficient to describe porous dust aggregates.

Conclusions. We have provided the functional behavior of tensile and shear strength of porous dust aggregates as a function of the porosity, which can be directly applied to continuum simulations of these objects in planet formation scenarios.

Key words. Planets and satellites: formation – Methods: numerical

1. Introduction

The formation of planetesimals, which are kilometer-sized objects that are massive enough for gravity to come into play, constitutes a key step in the core accretion scenario for planet formation proposed by Pollack et al. (1996). However, the earlier growth from mm to km sized bodies has not yet been fully understood. Understanding the interplay between porosity, impact velocity, and the size and structure of colliding aggregates in the meter-size regime is crucial to unraveling the process of planetesimal formation. Obviously, this size regime renders laboratory experiments impossible. Thus, for years to come astrophysicists will have to rely on computer simulations to obtain the necessary insight into this complex process.

Molecular dynamics simulations featuring detailed micro-mechanical interactions have been employed to study collisions of sub-mm sized dust and ice aggregates (e.g., Dominik & Tielens, 1997; Wada et al., 2007; Ringl et al., 2012). Owing to the high computational demand, a different approach is necessary for the mm to meter size regime. In this regime, SPH simulations have often been utilized to model preplanetesimal collisions (e.g., Sirono, 2004; Schäfer et al., 2007; Geretshauser et al., 2011). Smoothed particle hydrodynamics (SPH) constitutes a continuum approach that is able to simulate the collisional behavior of macroscopic aggregates including physical processes such as compaction or fragmentation. As a continuum approach, SPH requires various material parameters such as the

compressive, tensile, and shear strength, so that a proper calibration is necessary (Geretshauser et al., 2010). Typically, the calibration process is based on comparison with results from laboratory experiments (Güttler et al., 2009). However, not all material parameters have been obtained in this way. For instance, the shear strength has only been based on theoretical models and estimations so far.

Only a few laboratory experiments have been performed to investigate the mechanical properties of porous dust aggregates. Blum & Schräpler (2004) measured the tensile strength of highly porous dust aggregates generated by random ballistic deposition. Since they used monodisperse, spherical silica grains, their experiments are comparable to our simulations. It has been shown both theoretically (Bertini et al., 2009) and experimentally (Blum et al., 2006) that the mechanical properties depend on the shape and size distribution of the grains. Recently, Meisner et al. (2012) presented results from various experiments on the mechanical properties of irregularly shaped quartz aggregates.

Determining material parameters directly from molecular dynamics simulations of porous dust aggregates constitutes a tempting alternative. Paszun & Dominik (2008) presented the first attempt to obtain the compressive strength from ab initio simulations. A few years later, Seizinger et al. (2012) studied the compressive strength in greater detail and especially revealed the differences between static and dynamic compaction processes.

Article number, page 1 of 9

Table 1. Material parameters.

Physical property	Silicate
Particle radius r (in μm)	0.6
Density ρ (in g cm^{-3})	2.65
Surface energy γ (in mJ m^{-2})	20
Young's modulus E (in GPa)	54
Poisson number ν	0.17
Critical rolling length ξ_{crit} (in nm)	2

The aim of the present work is to extend this approach to determine the tensile and shear strength of porous aggregates. Together with the compressive strength we then can provide continuum simulations (such as SPH) with a complete parameter set describing the transition from elastic to plastic deformation.

2. Interaction model

We simulated the behavior of porous dust aggregates with a molecular dynamics approach. In this work we use cuboidal shaped aggregates with an edge length of 30 to 60 μm . Depending on its volume filling factor, such an aggregate consists of up to $6 \cdot 10^4$ micron-sized spherical grains (monomers).

The interaction between individual monomers is based on the work of Dominik & Tielens (1997). Based on earlier theoretical work by Johnson et al. (1971); Dominik & Tielens (1995, 1996), they developed a detailed micromechanical model of the interaction of two microscopic spherical grains. When two monomers touch each other, surface forces allow for the creation of an adhesive contact. Upon deformation of these contacts caused by the relative motion of the monomers, kinetic energy is dissipated. This approach is favorable to our purpose because the process of internal restructuring of the aggregate is modeled far more realistically than in simpler hard-sphere models.

Later, Wada et al. (2007) derived almost the same interaction laws from corresponding potentials. Seizinger et al. (2012) calibrated the interaction model by comparison with laboratory experiments on the compression of porous dust aggregates (Güttler et al., 2009). They observed that the original model of Dominik & Tielens (1997) was too soft. To increase the strength of the aggregates, Seizinger et al. (2012) introduced the rolling and sliding modifiers m_r and m_s that modify the strength of the corresponding type of interaction. By increasing the rolling interaction by a factor of 8 and the sliding interaction by a factor of 2.5, they achieved excellent agreement between numerical simulations and laboratory results.

In this work we use the modified interaction model presented by Seizinger et al. (2012) with $m_r = 8$ and $m_s = 2.5$ unless stated otherwise. The material parameters are listed in Table 1.

3. Sample generation

In this section we briefly summarize our sample-generation methods. Here we use cuboidal-shaped dust aggregates (also referred to as dust cakes) of different porosities. In principle, we may employ different methods to generate these samples. As shown in in Fig. 1 the relation between the volume filling factor and the average coordination number n_c depends on the selected generation method (Seizinger & Kley, 2013).

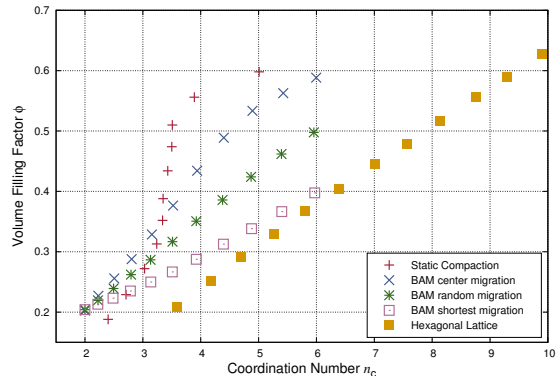


Fig. 1. The relation between the volume filling factor ϕ and the average coordination number n_c . Figure taken from Seizinger & Kley (2013).

The volume filling factor ϕ is given by

$$\phi = \frac{NV_p}{V}, \quad (1)$$

where N denotes the number of monomers, V_p is the volume of an individual monomer, and V is the total volume occupied by the sample. The coordination number, n_c , denotes the number of contacts a monomer has established with its neighbors. The mean n_c of the sample is calculated by averaging the number of contacts of each monomer.

3.1. Static compaction

Static compaction constitutes a method that very closely resembles the generation process of dust cakes in laboratory experiments. Initially, a dust cake is built by random ballistic deposition (RBD) where single monomers are successively dropped onto the existing sample. They come to rest right at the spot where they hit the existing sample. This growth process results in fractal, highly porous aggregates with a volume filling factor of $\phi = 0.15$ (Watson et al., 1997).

In the second step, the RBD cake is put into a box and compacted until the desired filling factor is reached. However, the compaction must occur slowly enough to avoid inhomogeneities (Seizinger et al., 2012). For the material/monomer size used in this work, a typical speed of the compacting wall is 1 cm s^{-1} . The simulation time needed to compact an aggregate is proportional to the desired size and filling factor. Since the number of monomers increases with the size and compactness of the final dust cake, the computational effort per integration step rises as well. Thus, generating samples by static compaction can become a computationally expensive, time-consuming procedure.

Elastic loading of dust cakes compressed to filling factors above ≈ 0.45 constitutes another setback of this method (Seizinger & Kley, 2013). Because of the elastic energy stored in the contacts between monomers the aggregate will start to expand once the confining walls of the compaction box are removed. This effect will alter the results of a measurement of the tensile or shear strength significantly.

Up to a filling factor of ≈ 0.58 dust cakes may be stabilized in the following way. After slightly disturbing the positions of monomers, the aggregate is kept in a box until the energy induced by the disturbance is damped away (Seizinger & Kley, 2013).

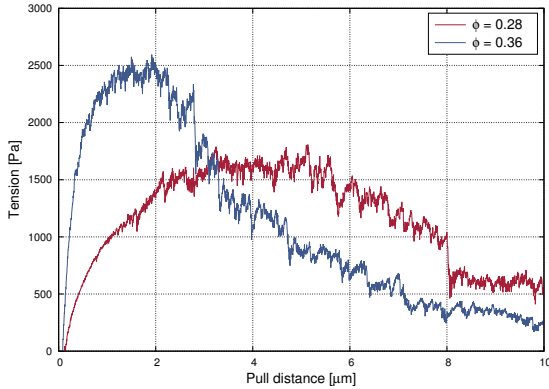


Fig. 2. Example of the tension required to pull the plates apart from each other for two cubical samples of different porosity. As the pull distance increases the required force decreases because cracks form in the sample.

3.2. Ballistic aggregation and migration

The generation procedure of ballistic aggregation and migration (BAM) has been proposed by Shen et al. (2008). A larger aggregate is generated by successively shooting in single monomers from random directions onto the existing aggregate.

In Seizinger & Kley (2013) we employed three different methods to select the final position of a monomer hitting the aggregate:

1. Select the position closest to the spot, where the monomer impacts the aggregate (referred to as “shortest migration”).
2. Select the position randomly from all available possibilities (referred to as “random migration”).
3. Select the position that is closest to the center of mass (referred to as “center migration”).

The volume filling factor of the generated aggregate depends on the selection mechanism. For a given coordination number, aggregates generated with the “shortest migration” feature the lowest filling factor, whereas the “center migration” method leads to the most compact aggregates.

The relation between the filling factor and the coordination number is displayed in Fig. 1, for the different preparation methods. For comparison we show the results for the hexagonal close packing as well, see Seizinger & Kley (2013) for more details. After generating a sufficiently large aggregate, a cuboidal shaped dust cake of the desired size is sliced out to be used for the subsequent numerical experiments.

4. Tensile strength

4.1. Setup

In principle, the procedure for determining the tensile strength of a given sample is simple. After attaching two plates at the top and bottom of the cubic aggregate, the plates are pulled apart at constant speed. During this process the pulling force exerted on these plates is measured. At first, the force will increase with the distance between the plates. If a certain distance is exceeded, cracks will form. Thus, the strength of the sample is reduced and the force required to pull the two plates apart decreases. An example showing a typical relation between the pull distance and

tension is shown in Fig. 2. It is very similar to experimental data (see Blum & Schröpfer, 2004, Fig. 4).

The force is determined by summing up the individual interaction forces of all monomers that are in contact with the wall. In the case of the tensile strength, only the component in the direction of the motion of the wall (which is equivalent to the normal vector of the wall) is taken into account. To allow easier comparison between different sized samples, we use their base area to normalize the values and plot the corresponding tension instead of the force.

In accordance with Blum et al. (2006), we define the maximum tension that is measured during a run as the tensile strength of the sample. The displacement at which force/pressure peaks depends on the porosity of the sample. In a sample with a high filling factor, monomers are fixed tightly, which hampers internal restructuring. In contrast, in a fluffy sample individual chains of monomers can be unfolded, and thus the material can be stretched out significantly before the formation of cracks sets in.

To model this setup in our simulations, the sample is put into a box of flat walls. Before slowly moving the top and bottom walls away from each other, we must ensure that enough monomers are in contact with these walls. For this purpose the top and bottom walls are slowly pushed inwards a short distance. For samples with filling factors below $\phi = 0.2$, we use a value of one monomer radius, whereas for more compact samples, we decrease the distance to $0.5 - 0.1$ monomer radii.

Another problem arises when pulling the two plates away from each other. The critical force F_c required to break a contact between two monomers is given by $F_c = 3\pi\gamma R$, where γ denotes the surface energy and R the reduced radius of the two particles (Johnson et al., 1971). The wall is modeled as a particle of infinite radius, which means that the reduced radius of a particle-wall contact equals twice the reduced radius of a particle-particle contact (Seizinger et al., 2012). Thus, contacts between two particles can be broken more easily than particle-wall contacts. As a result, the monomers that are in contact with one of the plates tend to get ripped off the remaining sample (see left panel of Fig. 3).

To counter this effect we artificially increase the strength of the adhesion between two monomers depending on the distance to the plates. To achieve this “gluing effect” the force/potential of the normal interaction that is responsible for the adhesion is multiplied by a gluing factor κ . To avoid discontinuities in the particle interaction, κ is interpolated linearly depending on the distance to the closest plate. Above a threshold of eight particle radii κ is set to 1 and thus the default JKR interaction is used. As shown in the righthand panel of Fig 3, this mechanism leads to the rupture somewhere in the middle of the sample rather than just tearing off the upper- or lowermost layer of monomers. Because the first cracks will form where the aggregate is weakest, the exact location is random owing to the inhomogeneous structure of the aggregate.

We tested different maximum values of κ and found that a value of 2 is sufficient for our purpose. For $\kappa < 1.5$, samples do not break in the center anymore. On the other hand, higher values do not alter the measured tensile strength significantly (see Fig. 4).

4.2. Results

Apart from the wall-gluing factor κ , there are several other parameters whose influence has to be studied. To determine the influence of the rolling and sliding interaction, we performed a series of simulations using $m_r = m_s = 1$, which is equivalent to

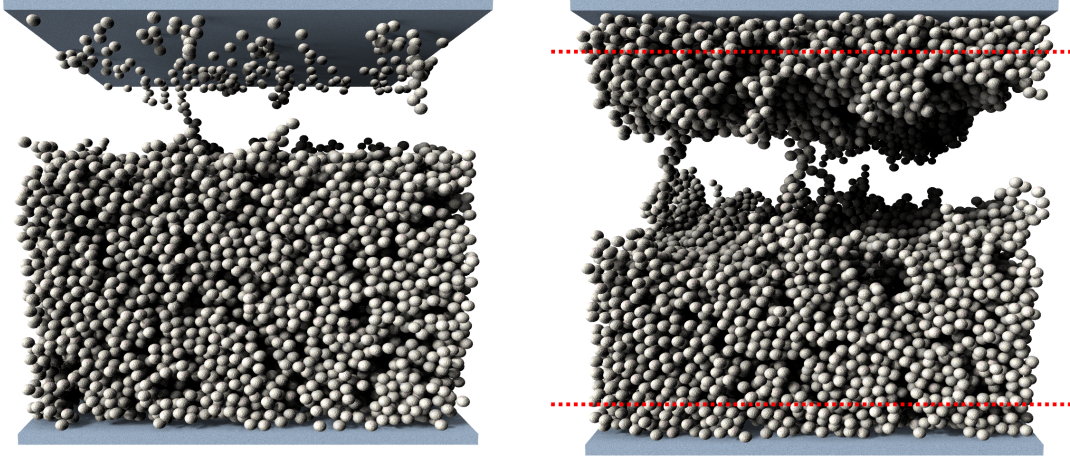


Fig. 3. Outcome of a typical pull experiment on a cubical sample agglomerate. *Left:* Since the adhesion between particle-wall contacts is stronger than between particles, the uppermost layer of particles is ripped off when pulling the plates away from each other. *Right:* Adhesion between particles that are close to one of the plates has been artificially increased. The red dotted line indicates where the additional gluing effect sets in.

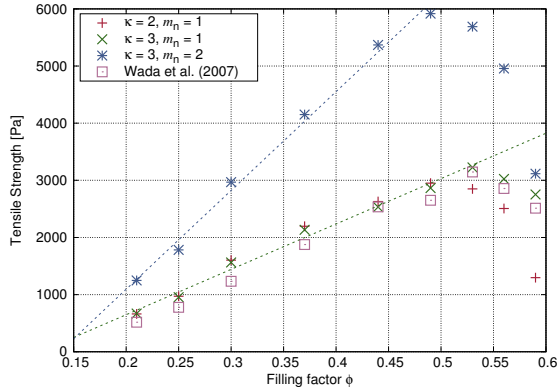


Fig. 4. Tensile strength for different wall glue factors κ and normal interaction modifiers m_n using the model from Seizinger et al. (2012) ($m_r = 8, m_s = 2.5$). The dotted lines represent linear fits for filling factors below 0.5. For comparison, we also performed simulations using the model employed by Wada et al. (2007) ($m_r = m_s = 1$). All samples are BAM cakes with an edge length of $50 \times 50 \times 30 \mu\text{m}$.

the model of Wada et al. (2007). In this and all of the following simulations, we used a wall-gluing factor of $\kappa = 2$. Apparently, internal restructuring that is governed by rolling and sliding does not play a major role when determining the tensile strength (see the purple squares in Fig. 4 showing results for the model from Wada et al. (2007)).

Contacts between the monomers have to be broken while the sample aggregate is torn apart. Therefore, we expect that the measured tensile strength depends on the number of contacts that have to be broken, as well as on the critical force F_c that is necessary to break a contact between individual monomers. To check this hypothesis, we alter the strength of the normal force by mul-

tiplying it by the normal force modifier m_n . Indeed, when doubling the strength of the normal interaction (and thus F_c) by setting $m_n = 2$, we observe a steeper increase in the tensile strength with the filling factor (blue asterisks in Fig. 4). When determining a linear fit for filling factors below 0.5 to the $\kappa = 3, m_n = 1$ and $\kappa = 3, m_n = 2$ simulations we get slopes of 7.9 kPa and 15.3 kPa, respectively. Their ratio of $15.3/7.9 = 1.94$ is very close to the value of the normal interaction modifier $m_n = 2$. This strongly suggests that the pull-off force F_c is critical for the measured value of the tensile strength.

Independent of κ, m_n , or the rolling and sliding interaction, there is a striking drop in the tensile strength for filling factors above 0.5. To unravel its cause we first used a different type of sample. Much to our surprise, the critical filling factor at which the tensile strength drops is different for each type of aggregate and close to the maximum filling factor that may be achieved by a given generation method (see Fig. 5). Apparently, the micro-mechanical behavior is not governed by the volume filling factor alone.

Therefore we take the average coordination number n_c into account. From the relation between the filling factor and the coordination number of the different sample types (see Fig. 1), we find that the drop in the measured tensile strength of BAM aggregates coincides with a value of n_c around ≈ 4.5 (see Fig. 6). This points to the influence of the coordination number on the micro-mechanical properties of the sample aggregates. If the average coordination number is low, the majority of monomers may react to an external stress by rearranging themselves. Thus, a large number of monomers participate in absorbing the external stress, and the aggregate exhibits rather ductile behavior. As the coordination number increases, monomers are fixated in their positions more tightly. For compact aggregates the monomers cannot rearrange themselves freely any longer, which means that fewer monomers have to absorb the applied strain. Therefore, the aggregates become brittle.

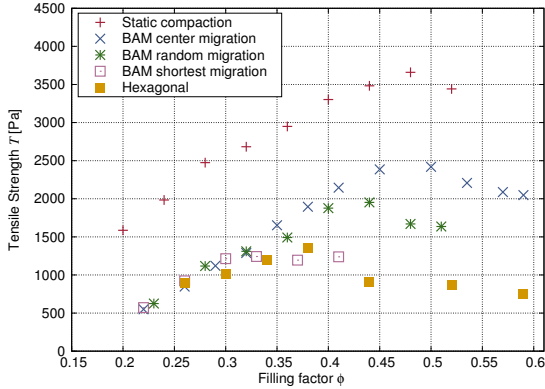


Fig. 5. Comparison of the relation between the filling factor ϕ and the tensile strength of different sample types. Most noticeably, the measured tensile strength always drops when a certain type-specific filling factor is exceeded.

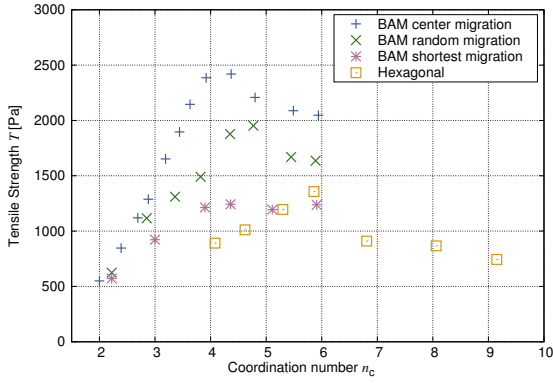


Fig. 6. Comparison of the relation between tensile strength and initial coordination number n_c of different sample types. The tensile strength of the different BAM aggregates drops for values of n_c around 4.5. For the hexagonal close-packing aggregates we see a clear drop for $n_c \rightarrow 6$.

The effect of brittleness can clearly be seen in the case of the hexagonal lattice aggregates. Because of their regular, crystal-like structure (see Seizinger & Kley, 2013, Fig. 1a), their capability of internal restructuring is very limited. Thus, contacts break very easily when external strain is applied. As a result, the measured tensile strength is considerably lower than for BAM or static compaction aggregates.

Additionally, the pressure exerted on the sample when slowly pressing on the top and bottom walls suffices to disrupt very compact aggregates. Moving the top and bottom walls inwards by a distance of 0.5 to 0.15 particle radii is necessary to establish a firm contact between the walls and the sample. For a BAM (center migration) aggregate with $\phi = 0.59$, for example, the average coordination number decreased from 5.94 to 4.95 after moving the top wall inwards by a distance of only 0.1 monomer radii. This means that the strength of the sample is lowered during the preparation process. This raises the question of whether the transition from ductile to brittle behavior or the disturbance when affixing the plates is the dominant effect.

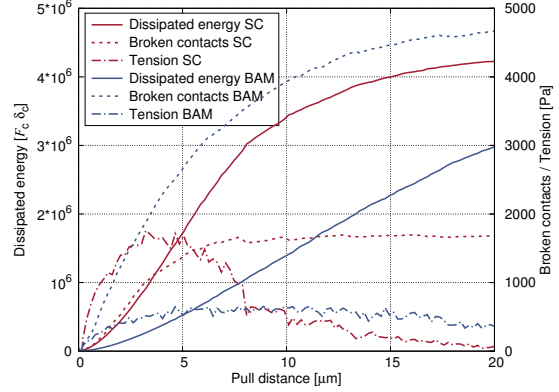


Fig. 7. The dissipated energy (solid line) and the total number of broken contacts (dotted line) of BAM and static compaction (SC) aggregates while pulling the plates apart. The size of both samples is $50 \times 50 \times 30 \mu\text{m}$, and their initial filling factor is $\phi = 0.28$. The critical force F_c and critical distance δ_c at which a contact breaks are used to normalize the energies. For comparison, the corresponding tension (dashed-dotted line) is also plotted.

Recently, Kataoka et al. (2013) presented a different approach to determining the compressive strength of highly porous ($\phi < 0.1$) dust aggregates by using periodic boundary conditions. A similar approach might work for the tensile strength as well and would avoid the problem of attaching the plates to a highly compact sample without lowering its strength. Luckily, measuring the tensile strength of hexagonal lattice aggregates also allows us to circumvent this problem. Because of their regular grid structure, the contact between the wall and all particles of the top or bottom layer is established without compacting the sample. Nevertheless, we observe a significant drop in the tensile strength for $n_c \rightarrow 6$ (see Fig. 6). This observation allows us to conclude that the disruption caused by affixing the plates only plays a secondary role.

To explain the discrepancy between BAM and static compaction aggregates as shown in Fig. 5, the process of pulling the plates apart is analyzed more closely. Comparing the dissipated energy of the different types of aggregates, we clearly see that tearing the static compaction aggregate apart requires more energy (Fig. 7). Thus, a higher value of the tensile strength is measured. Tracking the number of contacts that have been broken since the start of the simulation provides us with a hint at an explanation of this observation: Compared to the BAM aggregate, fewer than half as many contacts break while pulling the static compaction aggregate apart, although more kinetic energy is dissipated.

This observation might be surprising at first sight, yet it illustrates the importance of the internal structure for the outcome of the measurements. In reaction to the applied strain, the internal structure of the aggregates changes, where inelastic rolling accounts for $\approx 80\%$ and the breaking of contacts for only $\approx 3\%$ of the total dissipated energy for both aggregate types. In the case of the static compaction aggregate, the final number of broken contacts is reached much more quickly after pulling the sample roughly $7.5 \mu\text{m}$ apart. Likewise, the peak of the measured tension is reached earlier. At this point, a lot more energy has been dissipated by internal restructuring (mainly by inelastic rolling) than for the BAM aggregate.

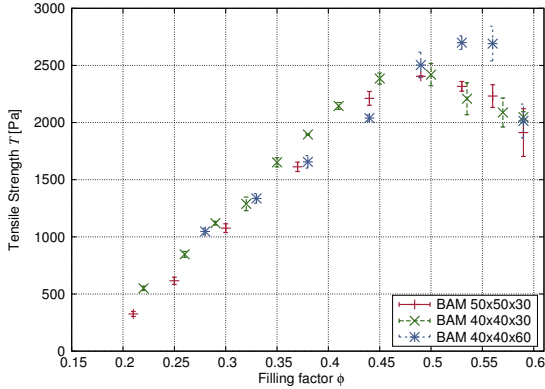


Fig. 8. Tensile strength measurements for BAM (center migration) aggregates of different size. The error bars have been determined by averaging the results of six runs with different samples.

However, for the BAM aggregates, the total number of broken contacts increases much faster. This means that the internal structure of this type of aggregate allows for less restructuring before contacts start to break. Since roughly 97% of the dissipated energy is required for restructuring rather than breaking the contacts, we measure a lower tensile strength for BAM aggregates.

We think that the reason behind this observation lies in the fact that the tensile strength test is the reversal of the compression process by which the static compaction aggregates have been generated. While being slowly compacted to the desired filling factor, enough time had been given to the fractal chains of the initial RBD aggregates to rearrange themselves. As a result, the monomers of the static compaction aggregates adopt a structure that is favorable to withstand an external load.

While pulling the plates apart, the total number of broken contacts (Fig. 7) sometimes decreases. This happens when the connection between two already stretched out parts of the sample breaks and both parts “snap back”.

We also checked whether there are any preferred directions resulting from the generation process. For this reason we rotated cubic static compaction samples by 90° before determining the tensile strength. Reassuringly, we measured the same values (not shown in this work) and may rule out that the direction of the compaction induces any preferred direction in the structure of the sample.

As a last step we varied the geometry of the samples to check that the size influences the results. As seen in Fig. 8, the results do not vary significantly if we alter the size of the samples. In Fig. 9 we compare our results with laboratory experiments performed by Blum & Schr apler (2004) and Blum et al. (2006). Considering that their samples have been produced by static compaction, our results show good agreement with their data for filling factors below $\phi = 0.5$. Because of the drop in the tensile strength for $n_c \rightarrow 6$ explained in the previous paragraphs, we cannot compare our simulations to laboratory experiments for higher filling factors. Earlier compression simulations have already indicated that our physical model may no longer be valid for highly compact aggregates (Seizinger et al., 2012). Luckily, the filling factor regime relevant to the growth processes of planetesimals is below 0.5 (e.g., Teiser et al., 2011).

Article number, page 6 of 9

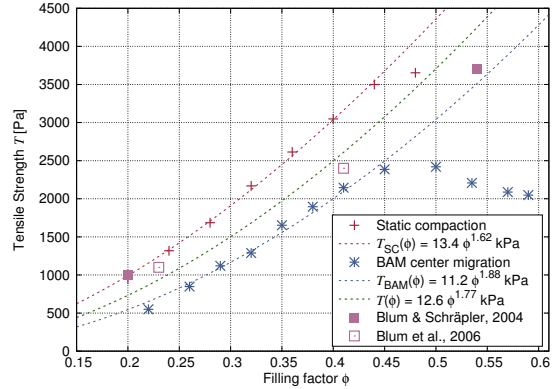


Fig. 9. Comparison of the results of simulations with static compaction and BAM (center migration) aggregates to laboratory experiments by Blum & Schr apler (2004); Blum et al. (2006). The fitting curve has been obtained by combining both data sets for filling factors $\phi < 0.5$.

To determine the fitting curve depicted in Fig. 9, only data points for filling factors below 0.5 have been taken into account. Because of the significant difference between the static compaction and BAM aggregates, we determined two fit curves $T_{SC}(\phi)$ and $T_{BAM}(\phi)$, respectively. We obtain

$$T_{SC}(\phi) = 13.4 \phi^{1.62} \text{ kPa}, \quad (2)$$

and

$$T_{BAM}(\phi) = 11.2 \phi^{1.88} \text{ kPa}. \quad (3)$$

Based on their generation process, the laboratory samples should resemble the static compaction cakes. Indeed, for $\phi \approx 0.2$, our simulations agree very well with laboratory experiments (Blum & Schr apler, 2004; Blum et al., 2006). However, for higher filling factors, the laboratory results lie somewhere between the static compaction and BAM results. In private conversation J urgen Blum (Braunschweig) pointed out that creating more compact samples in the lab sometimes proved to be a difficult task. Thus, we also determined a fit $T(\phi)$ to the combined results of the static compaction and BAM aggregates. Using the combined data points from both aggregate types shown in Fig. 9 for a single fit $T(\phi)$, we find, for values of $\phi < 0.5$,

$$T(\phi) = 12.6 \phi^{1.77} \text{ kPa}. \quad (4)$$

4.3. Influence of the monomer size

Most other numerical simulations dealing with silicates have been performed with monomers with a diameter of 1.2 and $1.5 \mu\text{m}$ because these sizes have been used in laboratory experiments with spherical silicate grains. Out of curiosity we varied the size of the monomers. In general, it can be said that according to JKR-theory, the adhesion forces increase as grains get smaller. Indeed, we find that the tensile strength depends closely on the size of the monomers (see Fig. 10). Our interaction model has not been calibrated for monomer radii other than $r_p = 0.6 \mu\text{m}$. Therefore the rolling and sliding modifiers m_r and m_s may not have the correct values to properly describe restructuring processes. However, in the case of the tensile strength, this problem does not arise, as we have already seen that it is mainly governed by the normal interaction (see Fig. 4).

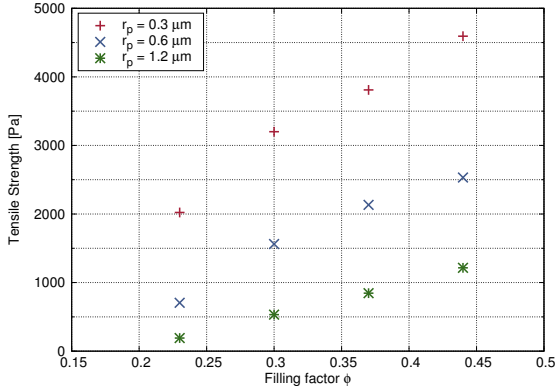


Fig. 10. Tensile strength for aggregates composed of differently sized monomers. The default monomer radius is $r_p = 0.6 \mu\text{m}$, which is also used in the corresponding laboratory experiments.

From Fig. 4 we see that the tensile strength scales linearly with the normal interaction. Altering the monomer size by a factor of 2 for the transition from $0.6 \mu\text{m}$ to $1.2 \mu\text{m}$ sized monomers, the change in the measured tensile strength differs from 2. At first glance this may seem odd since the critical pull-off force F_c depends linearly on the monomer radius. However, the dependence of the normal force acting upon the monomers before they are separated on the monomer radius is nonlinear (see Seizinger et al., 2012, Eqs. 2 and 3). Nevertheless, these simulations confirm the importance of the pull-off force F_c that has already been shown in Fig. 4.

The results clearly demonstrate the effect of the stickiness of the single monomers on the tensile strength. For future work it would be interesting to perform simulations with aggregates composed of monomers of different sizes.

5. Shear strength

5.1. Setup

The shear strength of a porous aggregate is determined in a similar way to the tensile strength. As before, two plates are attached to the top and bottom of the sample. During the shearing motion of the plates, the force acting on them is tracked. However, for the shear strength, the direction of motion is perpendicular to the normal of the wall, i.e. tangential to a cuboid surface. During the simulation the vertical positions of the top and bottom walls remain fixed to keep the filling factor constant. This means, similar to the “fixed walls” used in the work of Seizinger et al. (2012), that the normal component of the force acting upon the walls is ignored. As before, the initial base area of the sample is used to normalize the force.

The setup closely resembles the tensile strength setup. A firm contact between the sample and the plates is achieved in the same way as described in Sect. 4.1. To prevent the monomers that are in contact with the moving wall from being torn away from the sample, an additional “gluing effect” is applied to particles that are close to one of the plates. A snapshot taken during a typical simulation is depicted in Fig. 11.

While the top plate is slowly moving, shearing sets in. With increasing pulling distance, cracks will form and reduce the strength of the sample. Thus, we expect a similar shape to the one for the tensile strength if we plot the tension acting on the

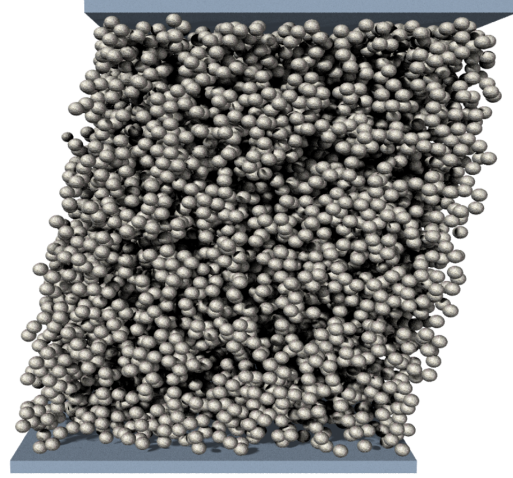


Fig. 11. A snapshot taken during a shear strength test using an aggregate with an edge length of $30 \times 30 \times 40 \mu\text{m}$

. The upper plate is slowly moving to the right. Adhesion between particles that are close to one of the plates has been artificially increased.

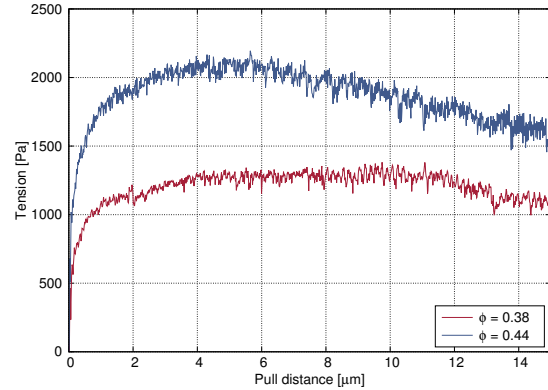


Fig. 12. Example of the tension (force per area) acting on the upper plate during the shearing motion.

moving plate with respect to the displacement. Indeed, the example shear strength curve shown in Fig. 12 resembles the curves shown in Fig. 2. Similar to the tensile strength case, we define the shear strength as the maximum tension that is measured during the simulation. Again, the higher the porosity of a sample, the larger the necessary displacement at which the force peaks.

5.2. Results

Owing to the computational demand of the simulations, the size of our samples is limited to values below 0.1 mm . To study the dependency of our results on the sample size, we prepared both BAM and static compaction aggregates with different edge lengths. For each data point, six different samples with equal statistical properties have been generated.

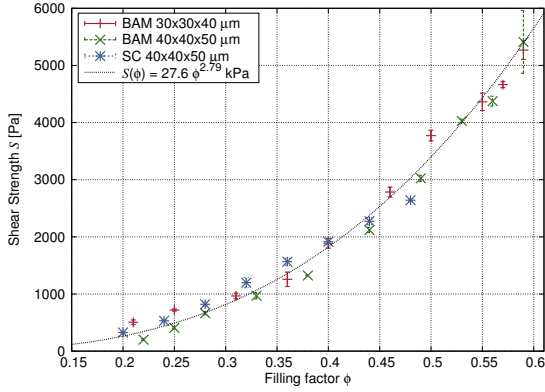


Fig. 13. Comparison of the relation between the filling factor ϕ and shear strength of different sample types and sizes. The error bars have been determined by averaging the results from six different samples. The black dotted line has been obtained by fitting a power law to the results from BAM and static compaction aggregates with an edge length of $40 \times 40 \times 50 \mu\text{m}$.

Some of the results are shown in Fig. 13. As we can see, the results of the different sample sizes do not alter significantly. In order to check whether the length of the sample in the direction of the shearing motion is sufficient we also performed simulations for sample sizes of $80 \times 40 \times 50 \mu\text{m}$ and $120 \times 40 \times 50 \mu\text{m}$. Owing to the huge number of particles, these simulations took several weeks. Therefore we restricted the values of the filling factor to $\phi = 0.33$ and $\phi = 0.49$. The deviation to the values obtained from the smaller $40 \times 40 \times 50 \mu\text{m}$ aggregates was $\approx 8-10\%$ for $\phi = 0.33$ and $\approx 2-3\%$ for $\phi = 0.49$. Thus, we may draw the conclusion that the samples are in fact sufficiently large. With the exception of the most compact samples ($\phi = 0.59$), the error bars obtained by averaging the results from the six samples are very small.

Interestingly, we do not observe a significant difference between the static compaction and BAM aggregates as in the case of the tensile strength. As explained in Sect. 4.2, owing to their generation process, the internal structure of the static compaction aggregates is more favorable to counteracting external loading/tension. However, this does not apply to shearing motion that results in different kinds of deformation compared to the tensile strength test. Therefore, the two types of samples exhibit similar values for the shear strength.

To provide SPH simulations with a model for the shear strength that is easy to implement, we describe the dependency of shear strength S on the filling factor ϕ with a power law $S(\phi) = a\phi^b$. Using the results from BAM and static compaction aggregates of $40 \times 40 \times 50 \mu\text{m}$ edge length, we obtained (see Fig. 13)

$$S(\phi) = 21.7\phi^{2.65} \text{ kPa.} \quad (5)$$

5.3. Comparison with the SPH continuum model

One objective of the present investigations has been to compare the resulting strengths with those adopted in the SPH simulations by Geretschauser et al. (2010). To model shear failure, Sirono (2004) introduced a von Mises yielding criterion in his SPH simulations. The required shear strength is in principle equivalent to the shear strength obtained in our calculations. Güttler et al.

Article number, page 8 of 9

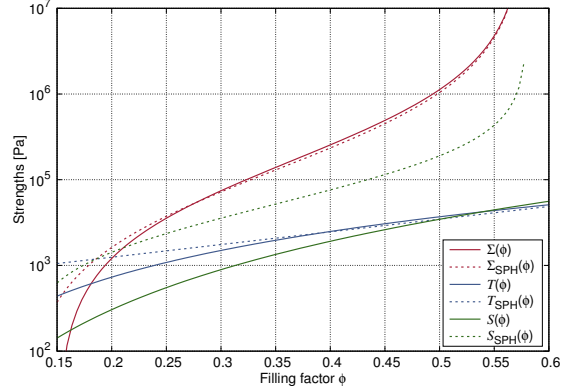


Fig. 14. Comparison of the fit curves for the compressive Σ , tensile T , and shear strength S derived in this work, and the corresponding functions Σ_{SPH} , T_{SPH} , and S_{SPH} adopted in the SPH code by Geretschauser et al. (2010). The compressive strength $\Sigma(\phi)$ has already been determined in earlier work (Seizinger et al., 2012).

(2009) calibrated their SPH model in an extensive process by comparing simulation results with laboratory experiments. They find a new representation for the dynamic compressive strength,

$$\Sigma_{\text{SPH}}(\phi) = 13 \left(\frac{\phi_2 - \phi_1}{\phi_2 - \phi} - 1 \right)^{0.58 \ln 10} \text{ kPa} \quad (6)$$

with $\phi_1 = 0.12$ and $\phi_2 = 0.58$, and they chose the tensile strength according to Blum & Schr apler (2004),

$$T_{\text{SPH}}(\phi) = 10^{2.8+1.48\phi} \text{ Pa.} \quad (7)$$

For the shear strength, no experimental data have been available. Therefore the shear strength was adopted following Sirono (2004) according to

$$S_{\text{SPH}} = \sqrt{\Sigma_{\text{SPH}} T_{\text{SPH}}}. \quad (8)$$

In Fig. 14 the fit curves of tensile strength $T(\phi)$, Eq. (4), and shear strength $S(\phi)$, Eq. (5), are compared to the corresponding values of the SPH model, $T_{\text{SPH}}(\phi)$, Eq. (7), and $S_{\text{SPH}}(\phi)$, Eq. (8). As can be seen, the tensile strength curves match rather well. This emphasizes that the present molecular dynamics method is well suited to modeling highly porous aggregates. The shear strength curves, however, differ by nearly one order of magnitude. This indicates that the approach of Sirono (Eq. 8) for the SPH shear strength, which is not based directly on laboratory experiments, might be inappropriate. But during the calibration process it was found already that the SPH simulation results for the chosen reference problems only depend weakly on the exact values of the shear strength (Güttler et al., 2009).

6. Conclusions

This work supports the observation of Seizinger & Kley (2013) that the sample generation method influences its mechanical behavior significantly. Whereas the bouncing behavior of microscopic dust aggregates differs little for BAM and static compaction aggregates, they do behave differently when external strain is applied (see Fig. 5). It is important to keep this in mind when comparing numerical simulations to laboratory results.

Observing the transition from ductile to brittle behavior for coordination numbers of ≈ 6 is very interesting. It certainly influences the outcome of collisions as well. For brittle aggregates, fragmentation will play a significantly larger role.

In this work we determined simple power laws to describe the relation between the tensile strength (see Eq. 4) or shear strength (see Eq. 5) and the porosity. In combination with earlier work on the compressive strength (Seizinger et al., 2012), it provides a complete description when the inelastic regime is entered upon deformation of porous dust aggregates. Since the dissipation of the kinetic impact energy is critical, this knowledge is crucial for continuum simulations of collisions of macroscopic porous aggregates.

Comparing with a special SPH model, we find that our tensile strength agrees well with the tensile strength adopted in the SPH code. The same holds for the compressive strength as found in earlier work (Seizinger et al., 2012). However, the shear strength differs significantly. Future analysis has to show whether our improved relation for the shear strength will have a fundamental impact on the SPH simulation results, or whether the shear strength only alters details in the simulations, as might be indicated by previous work.

Acknowledgements. A. Seizinger acknowledges support through the German Research Foundation (DFG) grant KL 650/16. The authors acknowledge support through DFG grant KL 650/7. Additional support through the German Research Foundation (DFG) through grant KL 650/11 within the Collaborative Research Group FOR 759: *The formation of Planets: The Critical First Growth Phase* is acknowledged. We thank the anonymous referee for pointing out possible misunderstandings and helping to improve the quality of the paper.

References

- Bertini, I., Gutierrez, P. J., & Sabolo, W. 2009, *A&A*, 504, 625
 Blum, J. & Schräpler, R. 2004, *Phys. Rev. Lett.*, 93, 115503
 Blum, J., Schräpler, R., Davidsson, B. J. R., & Trigo-Rodríguez, J. M. 2006, *ApJ*, 652, 1768
 Dominik, C. & Tielens, A. G. G. M. 1995, *Philosophical Magazine*, Part A, 72, 783
 Dominik, C. & Tielens, A. G. G. M. 1996, *Philosophical Magazine*, Part A, 73, 1279
 Dominik, C. & Tielens, A. G. G. M. 1997, *ApJ*, 480, 647
 Geretshauser, R. J., Speith, R., Güttler, C., Krause, M., & Blum, J. 2010, *A&A*, 513, A58
 Geretshauser, R. J., Speith, R., & Kley, W. 2011, *A&A*, 536, A104
 Güttler, C., Krause, M., Geretshauser, R. J., Speith, R., & Blum, J. 2009, *ApJ*, 701, 130
 Johnson, K. L., Kendall, K., & Roberts, A. D. 1971, *Royal Society of London Proceedings Series A*, 324, 301
 Kataoka, A., Tanaka, H., Okuzumi, S., & Wada, K. 2013, *A&A*, 554, A4
 Meisner, T., Wurm, G., & Teiser, J. 2012, *A&A*, 544, A138
 Paszun, D. & Dominik, C. 2008, *A&A*, 484, 859
 Pollack, J. B., Hubickyj, O., Bodenheimer, P., et al. 1996, *Icarus*, 124, 62
 Ringl, C., Bringa, E. M., Bertoldi, D. S., & Urbassek, H. M. 2012, *ApJ*, 752, 151
 Schäfer, C., Speith, R., & Kley, W. 2007, *A&A*, 470, 733
 Seizinger, A. & Kley, W. 2013, *A&A*, 551, A65
 Seizinger, A., Speith, R., & Kley, W. 2012, *A&A*, 541, A59
 Shen, Y., Draine, B. T., & Johnson, E. T. 2008, *ApJ*, 689, 260
 Sirono, S.-I. 2004, *Icarus*, 167, 431
 Teiser, J., Engelhardt, I., & Wurm, G. 2011, *ApJ*, 742, 5
 Wada, K., Tanaka, H., Suyama, T., Kimura, H., & Yamamoto, T. 2007, *ApJ*, 661, 320
 Watson, P. K., Mizes, H., Castellanos, A., & Perez, A. T. 1997, *Powders & Grains*, 109

Erosion of dust aggregates

A. Seizinger,¹ S. Krijt,² and W. Kley¹

¹ Institut für Astronomie und Astrophysik, Eberhard Karls Universität Tübingen,
Auf der Morgenstelle 10, D-72076 Tübingen, Germany
e-mail: alexs@tat.physik.uni-tuebingen.de

² Leiden Observatory, Leiden University, P.O. Box 9513, 2300 RA Leiden, The Netherlands

Received 30.09.2013; accepted 14.10.2013

ABSTRACT

Aims. The aim of this work is to gain a deeper insight into how much different aggregate types are affected by erosion. Especially, it is important to study the influence of the velocity of the impacting projectiles. We also want to provide models for dust growth in protoplanetary disks with simple recipes to account for erosion effects.

Methods. To study the erosion of dust aggregates we employed a molecular dynamics approach that features a detailed micro-physical model of the interaction of spherical grains. For the first time, the model has been extended by introducing a new visco-elastic damping force which requires a proper calibration. Afterwards, different sample generation methods were used to cover a wide range of aggregate types.

Results. The visco-elastic damping force introduced in this work turns out to be crucial to reproduce results obtained from laboratory experiments. After proper calibration, we find that erosion occurs for impact velocities of 5 ms^{-1} and above. Though fractal aggregates as formed during the first growth phase are most susceptible to erosion, we observe erosion of aggregates with rather compact surfaces as well.

Conclusions. We find that bombarding a larger target aggregate with small projectiles results in erosion for impact velocities as low as a few ms^{-1} . More compact aggregates suffer less from erosion. With increasing projectile size the transition from accretion to erosion is shifted to higher velocities. This allows larger bodies to grow through high velocity collisions with smaller aggregates.

Key words. Planets and satellites: formation – Protoplanetary disks – Methods: numerical

1. Introduction

In the past years, both laboratory experiments and numerical simulations have been able to shed light on many aspects of the growth processes leading to the formation of planetesimals. Nevertheless, various questions regarding the growth from microscopic dust grains to kilometer-sized bodies remain unanswered.

One of these open questions concerns the presence of small dust grains in protoplanetary disks. From observations, we know that sub-mm sized grains are present (e.g. Williams & Cieza, 2011). Yet, theoretical growth models predict a rapid depletion of small grains by sticking (Dullemond & Dominik, 2005). Replenishing the amount of small grains during the evolution of the disk may reconcile these predictions with observations. Destructive collisions of larger bodies are likely to come to mind as a source of small particles. But other effects such as photophoresis may contribute to the production of small grains as well (Wurm & Krauss, 2006; Kelling & Wurm, 2011; de Beule et al., 2013). Alternatively, it has been proposed that electric charging hinders the growth of larger bodies by suppressing coagulation of sub-mm sized grains (e.g. Okuzumi, 2009; Okuzumi et al., 2011).

In this work, we perform simulations to study the erosion of different aggregate types. To model high velocity impacts more accurately, we extend the molecular dynamics approach of Seizinger et al. (2012) by a new viscoelastic damping mechanism recently presented by Krijt et al. (2013). This work is supposed to provide the necessary data for a better treatment of erosion in the existing models for dust growth in protoplan-

etary disks (e.g. Ormel et al., 2007; Zsom & Dullemond, 2008; Birnstiel et al., 2010; Windmark et al., 2012; Drążkowska et al., 2013). Thus, we study the erosion efficiency for different aggregates with properties that are typically encountered during the growth process in protoplanetary disks.

In the beginning, dust growth is driven primarily by Brownian motion because micron-sized aggregates couple very well to the surrounding gas in the disk. Owing to the low relative velocities most frequent are hit & stick collisions without any restructuring. Such collisions result in the growth of very fluffy, fractal aggregates (e.g. Blum et al., 1996; Kempf et al., 1999). As these fractal aggregates are typical for the size regime of mm and below we study the erosion of fractal aggregates.

As the aggregates grow larger, their relative velocities increase and the hit & stick regime is left. Depending on the collision velocity compaction and fragmentation will set in (Blum & Wurm, 2000). As of today, the further evolution of dust aggregates is hotly debated. The impact of various processes such as compaction, fragmentation, bouncing, fragmentation with mass transfer, or reaccretion in aggregate collisions at different velocities and with different porosities has been studied in numerous laboratory experiments. For a helpful summary we refer to Blum & Wurm (2008) and Güttler et al. (2010).

Unfortunately, owing to the available computing power it is not possible to study any possible aggregate type at any given size. Instead, we restrict our study to a few aggregate types that may serve as prototypes. For this purpose we chose aggregates generated by particle-cluster aggregation (PCA) and several ballistic-aggregation-and-migration (BAM) aggregates. The

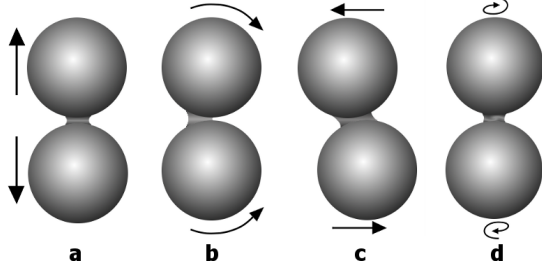


Fig. 1. The four types of particle interaction: Compression/Adhesion (a), Rolling (b), Sliding (c), and Twisting (d). Figure taken from Seizinger et al. (2012).

results obtained for these aggregate types are supposed to give an estimate on the erosion efficiencies expected for the more compact aggregates formed during the growth process in a protoplanetary disk.

2. Interaction model

2.1. Established model

In our simulations, aggregates are composed of thousands of equal sized, spherical grains (also referred to as monomers). Monomers interact with each other only if they are in contact. Energy is dissipated upon deformation of these contacts caused by the relative motion of the grains. Long range forces such as electromagnetic forces or gravity are not taken into account.

We use nearly the same interaction model as proposed by Dominik & Tielens (1997). To model the interaction of two spherical grains they distinguish between four types of motions (see Fig. 1). The equations describing these types of motions are mostly based on earlier theoretical work (Johnson et al., 1971; Dominik & Tielens, 1995, 1996). For rolling, sliding, and twisting, the interaction remains elastic as long as the displacement from the equilibrium state remains small. If a certain threshold is exceeded, the motion enters the inelastic regime and energy is being dissipated. Apart from one minor difference Wada et al. (2007) derived the same equations from corresponding potentials. This brings the advantage of being able to track how much energy is dissipated by which type of motion.

However, compared to laboratory experiments on the compression of porous dust aggregates performed by Güttler et al. (2009) the behavior predicted by the model of Dominik & Tielens (1997) was too soft. To overcome this discrepancy, Seizinger et al. (2012) modified the rolling and sliding interaction. They observed much better agreement between simulations and laboratory results by increasing the rolling interaction by a factor of 8 and the sliding interaction by a factor of 2.5.

In this work, we employ the modified interaction model proposed by Seizinger et al. (2012) with $m_r = 8$ and $m_s = 2.5$. The material parameters are listed in Tab. 1.

2.2. Visco-elastic damping

The critical sticking velocity v_{crit} at which the transition from sticking to bouncing occurs constitutes an important value when comparing the collisional behavior predicted by a theoretical interaction model with laboratory results. For micron sized silicate grains JKR theory predicts $v_{\text{crit}} \approx 0.1 \text{ ms}^{-1}$. However, in labora-

Table 1. Material parameters.

Physical property	Silicate
Particle Radius r (in μm)	0.6
Density ρ (in g cm^{-3})	2.65
Surface Energy γ (in mJ m^{-2})	20
Young's Modulus E (in GPa)	54
Poisson Number ν	0.17
Critical Rolling Length ξ_{crit} (in nm)	2
Viscous damping time T_{vis} (in s)	$1.25 \cdot 10^{-11}$

tory experiments on the stickiness of such grains a considerably higher sticking velocity of the order of 1 ms^{-1} has been measured (Poppe et al., 2000).

As an attempt to overcome this discrepancy Paszun & Dominik (2008) proposed surface asperities as a possible damping mechanism. Upon collision of two monomers small asperities on their surfaces get flattened. The corresponding plastic deformation would lead to the additional dissipation of kinetic energy. The damping was applied by artificially lowering the relative velocity of two monomers in the integration step where they collided with each other. However, when performing simulations with higher collisions velocities ($> \text{ms}^{-1}$) Seizinger et al. (2012) found that this damping mechanism introduced numerical instability.

In this work, we instead use the new damping force derived by Krijt et al. (2013), who show that for viscoelastic materials, the dissipative stresses in the contact area can be integrated to yield a damping force

$$F_D = \frac{2T_{\text{vis}}E^*}{\nu^2} a v_{\text{rel}}, \quad (1)$$

where a denotes the current contact radius and v_{rel} the relative normal velocity of the two monomers. The Poisson number ν and the reduced Young's modulus $E^* = E/(2(1-\nu^2))$ are material constants. The viscoelastic timescale T_{vis} is not well-known, but values around $10^{-12} - 10^{-11} \text{ s}$ allowed Krijt et al. (2013) to reproduce collision experiments with single microspheres very well.

The damping force given in Eq. 1 replaces the weak damping introduced by Seizinger et al. (2012) to prevent aggregates from being heated up artificially (Paszun & Dominik, 2008).

3. Erosion of RBD cakes

3.1. Calibration

In the first step, we calibrate our extended interaction model using the results of laboratory experiments performed by (Schräpler & Blum, 2011). In their work, they shot a volley of single monomers on a sample dust cake (from now on referred to as projectiles and target). The samples have been generated by random ballistic deposition (RBD) and had a high porosity (Blum & Schräpler, 2004). The velocity of the incoming projectiles was 15, 30, 45, and 60 ms^{-1} . After shooting a certain number of projectiles at the target the current weight of the target was measured. By repeating this procedure they determined the evolution of the mass loss with respect to the total projectile mass exposure (see Schräpler & Blum, 2011, Fig. 4).

In our simulations, we try to follow this procedure as closely as possible. We start by generating a target via random ballistic deposition. Owing to the computational demand imposed by

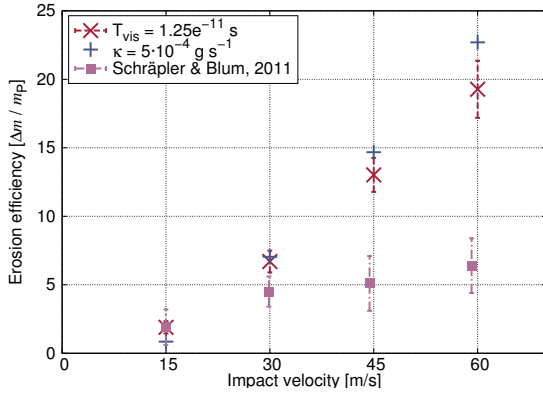


Fig. 2. Erosion efficiency for different velocities of the incoming projectiles. The errorbars have been determined by using 6 randomly generated targets with equal properties. At velocities below 30 ms^{-1} the results we obtain when setting $T_{\text{vis}} = 1.25 \cdot 10^{-11} \text{ s}$ (red crosses) agree well with laboratory experiments by Schräpler & Blum (2011) (purple squares). At higher velocities our micromechanical interaction model is probably no longer applicable as plastic deformation of the monomers will play a larger role. For comparison, we show results obtained by increasing the strength of normal damping mechanism introduced in Seizinger et al. (2012) by a factor of 500 (blue crosses).

high numbers of particles we limit the base area of the target to $100 \times 100 \mu\text{m}$. Initially, the target has a height of $\approx 70 \mu\text{m}$ and is composed of 10^5 monomers. Then, a barrage of 100 randomly distributed monomers is shot at the target. The mass loss Δm of the target is given by the number of monomers ΔN that are knocked out by the incoming projectiles. Dividing the number of eroded monomers by the number of projectiles we obtain the erosion efficiency ϵ

$$\epsilon = \frac{\Delta N}{N_p}, \quad (2)$$

where N_p denotes the total number of monomers of the incoming projectiles and $\Delta N = N_{\text{target,before}} - N_{\text{target,after}}$ the change of the number of monomers of the target aggregate. Thus, for $\epsilon > 0$ the target has been eroded whereas for $\epsilon < 0$ some of the projectile mass has been accreted onto the target. The values can be compared directly with the results from Schräpler & Blum (2011).

In Fig. 2, the erosion efficiency obtained from our simulations is compared to laboratory results (Schräpler & Blum, 2011, Fig. 5). By choosing $T_{\text{vis}} = 1.25 \cdot 10^{-11} \text{ s}$ we get an erosion efficiency of 1.89 ± 0.45 for $v = 15 \text{ ms}^{-1}$. This is in excellent agreement with the value of 1.9 ± 1.3 obtained from laboratory experiments (Schräpler & Blum, 2011). If we perform the simulations without the additional visco-elastic damping force we find $\epsilon = 83.16 \pm 1.68$ for $v = 15 \text{ ms}^{-1}$. This demonstrates impressively why a proper treatment of such damping effects is crucial in the high velocity regime.

Finding a value for T_{vis} that fitted the whole velocity range well was not possible. We believe that the discrepancy at collision velocities $\approx 30 \text{ ms}^{-1}$ and above is caused by the plastic deformation of single monomers. A plastic yield velocity of 30 ms^{-1} implies a material yield strength of $\approx 3 \text{ GPa}$ (Thornton & Ning, 1998), which is well within the range of $0.1 - 11 \text{ GPa}$ given by Paszun & Dominik (2008). In this velocity regime our physical model may therefore not provide a good description

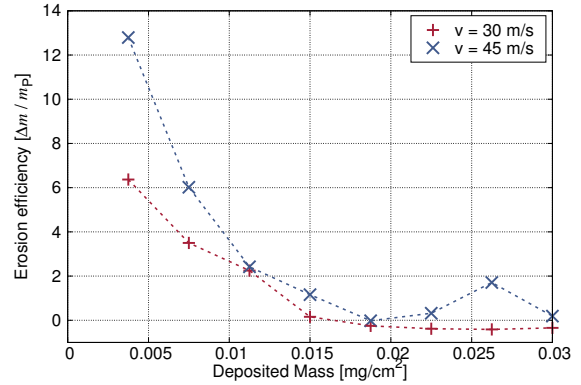


Fig. 3. Erosion efficiency with respect to the cumulative mass of the projectiles that have been shot at the target. Like in the laboratory experiments the trajectory of the incoming projectiles is perpendicular to the surface of the target. The target aggregate becomes passivated quickly which leads to a significant drop of the erosion efficiency.

anymore. Thus, we put our focus on the data points for lower impact velocities, which are also more relevant in the context of the collisions of smaller aggregates in protoplanetary disks (e.g. Brauer et al., 2008).

For comparison, we also show results from simulations without the new damping force given in Eq. 1. Instead, we greatly increased the strength of the normal damping force by setting $\kappa = 5 \cdot 10^{-4} \text{ gs}^{-1}$ (see Seizinger et al., 2012, Sect. 2.1.4). This corresponds to an increase of κ by a factor of 500. For $v = 15 \text{ ms}^{-1}$ this results in a drop of the erosion efficiency drops from 83.16 to 0.85. This means that we can also get much closer to the laboratory results by greatly increasing the strength of the normal damping (see blue crosses in Fig. 2). Nevertheless, we prefer the viscoelastic damping force proposed by Krijt et al. (2013) because its derivation is based on physical deliberations, whereas the weak normal damping had been introduced for numerical reasons only.

3.2. Passivation

The experiments by Schräpler & Blum (2011) show a decline of the erosion efficiency to very low values after shooting in a sufficiently large number of projectiles. Successive impacts restructure the upper layers of the target in such a way that further projectiles are less likely to knock out monomers. To check if we can reproduce this effect we bombard the same target repeatedly with 100 monomers. For each barrage we measure the erosion efficiency independently. Indeed, we observe a similar passivation effect (see Fig. 3). An example of how the structure of the samples changes after a bombardment with 1000 projectiles at $v = 30 \text{ ms}^{-1}$ is depicted in Fig. 4. As shown in the right panel of Fig. 4 the bombardment leads to the formation of deep holes and pillar like structures. Compared to the initial density in a RBD aggregate the monomer density in these pillars is increased. Similar restructuring processes have also been observed in the laboratory experiments (see Schräpler & Blum, 2011, Fig. 6).

So far, the trajectories of all projectiles have been perpendicular to the surface of the target. This leads to the question whether the pillar-shaped features will also emerge when projec-

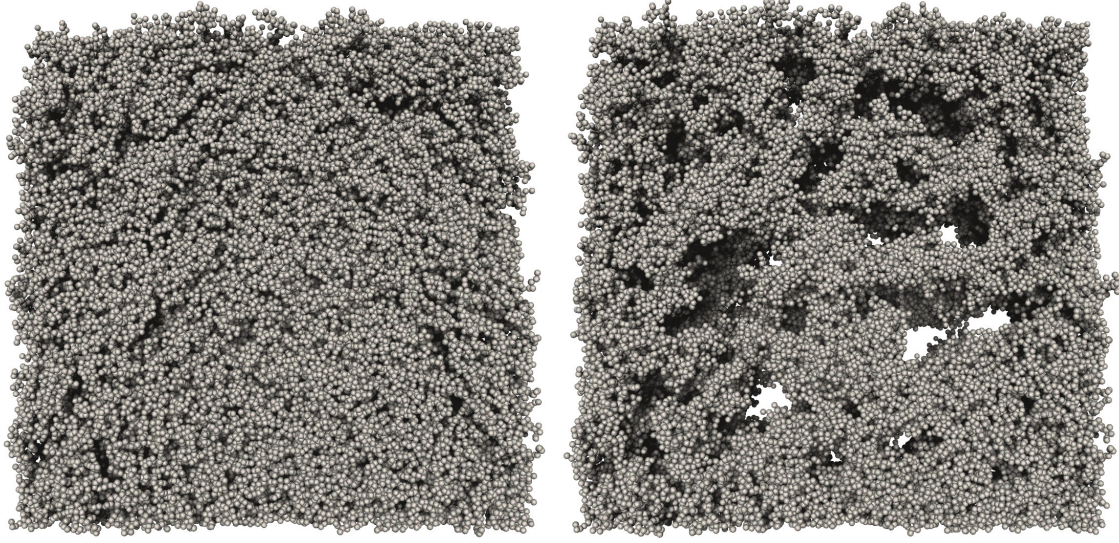


Fig. 4. Top-down view on a target aggregate before and after an impact sequence. Following the bombardment with a sufficient number of high speed projectiles the shape of the target aggregate changes significantly. *Left:* Initially, the RBD sample features a very homogeneous structure. *Right:* After shooting 1000 projectiles at the sample with $v = 30 \text{ ms}^{-1}$ the homogeneous structure has been destroyed. Deep holes and more compact pillars have formed.

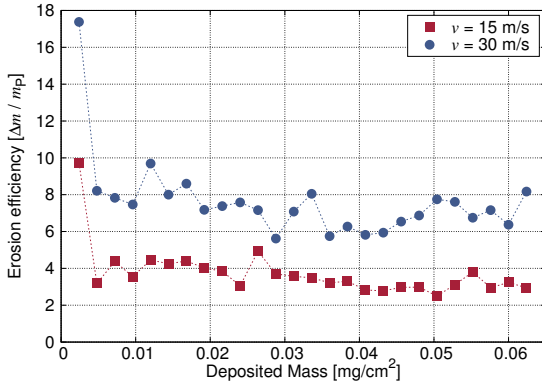


Fig. 5. Erosion efficiency with respect to the cumulative mass of the projectiles. Because the projectiles are coming in from random directions, this time a larger cake with a base area of $150 \times 150 \mu\text{m}$ and a height of $\approx 70 \mu\text{m}$ is used. Each data point depicts the average erosion efficiency after shooting in a bunch of 100 monomers. The random distribution of impact angles greatly reduces the passivation effect. At the end of the simulations roughly a quarter of the aggregate mass has been eroded.

tiles impact under different angles. While shooting in monomers from random directions is complicated in laboratory experiments it does not pose any problem in numerical simulations. Apart from the impact direction we use the same setup as before.

Indeed, after randomizing the impact angles the passivation effect seems to vanish (see Fig. 5). One might argue that there is small decline of the erosion efficiency, which indicates that the simulations had not fully converged yet. However, at the end of the simulations 25 % of the initial target mass have already been

eroded. As shown later in Sect. 4.2, no passivation is observed when shooting projectiles at an aggregate from random directions. Therefore we may conclude that it originates from the specific setup of the laboratory experiments. This is a relevant result because in the context of planet formation projectiles will hit from random directions. Thus, at least on the microscopic scale, passivation does not play an important role.

However, in Fig. 5 we notice a strong decrease of the erosion efficiency between the first and the second barrage of projectiles. Presumably, this is caused by chopping off the uppermost fractal chains of the initial target cake. As a result of the RBD generation process the uppermost part of the aggregate is less homogeneous than the parts below. Fractal, very fluffy chains of monomers stick out. They can be sandblasted away very easily by tangential hits. The first barrage of projectiles is sufficient to erode this upper layer.

Compared to the calibration simulations (see Fig. 2) we obtain higher values for the erosion efficiency when the projectiles impact from random directions. For $v = 15 \text{ ms}^{-1}$ the erosion efficiency roughly doubles from $\epsilon_{\text{calibration}} = 1.9$ to $\epsilon_{\text{random}} \approx 4$. The rise of the erosion efficiency is no surprise: In the calibration setup projectiles hit the surface of the target under an angle of 90° . Their kinetic energy suffices to knock a few monomers out at the impact location. The majority of these monomers is pushed deeper into the sample where they may be recaptured because their excess kinetic energy is dissipated by subsequent collisions with other monomers of the target. Since this recapturing mechanism is less effective for tangential impacts we measure a higher erosion efficiency when shooting in projectiles from random directions.

4. Erosion of aggregates

In this section we extend our studies to a variety of more realistic aggregates. The setup for the calibration simulation is

somewhat artificial compared to the processes in a protoplanetary disk. However, bombarding a free floating aggregate with single projectiles at a well defined impact velocity in laboratory experiments is not possible at the present time. Thus, we employ numerical simulation to address this question.

4.1. Sample generation

The target aggregates used in this work have been generated by a variety of methods. The aggregates generated by particle-cluster aggregation and random ballistic deposition are spherical and homogeneous. In contrast, the fractal aggregates have a non-spherical shape and are highly inhomogeneous. Examples of all three types are shown in Fig. 6.

Particle-cluster aggregation (PCA) constitutes an easy way to generate larger aggregates. The aggregate grows by adding single monomers from random directions. The monomers stick at the location where the first contact with the existing aggregate is established. Thus, the resulting aggregate will be rather fluffy with a volume filling factor of $\phi \approx 0.19$ (see left panel of Fig. 6). This procedure is similar to random ballistic deposition except that particles are coming from random directions rather than a specific side.

The second aggregate type is ballistic aggregation and migration (BAM) which has been suggested by Shen et al. (2008). As in the case of PCA monomers approaching from random directions are successively added to the aggregate. However, the final position of a monomer is determined in such a way that contact to two or three existing monomers is established at the same time resulting in more compact aggregates. For a more detailed description of the generation process we refer to Seizinger & Kley (2013, Sect. 3.2). In this work, we use two-times migration (BAM2), which means that after migrating once to establish contact with a second monomer, the migration process is repeated to get in contact with a third monomer. This procedure generates compact aggregates with a coordination number $n_c = 6$. An example of such an aggregate is shown in the center of Fig. 6.

The two aggregate types described above both share the disadvantage that their structure is somewhat artificial. Thus, we also use aggregates which have been obtained from a joint project where two different numerical techniques have been combined to simulate the growth of dust aggregates (Seizinger et al., in prep.). Starting with aggregates consisting of a single monomer, we followed the evolution of a swarm of representative aggregates using the approach presented by Zsom & Dullemond (2008). On the microscopic scale, every collision between two representative aggregates has been simulated using molecular dynamics. That way, the changes of the aggregate structure during the growth process could be resolved in great detail. The growth of sub-mm sized aggregates is primarily driven by Brownian motion which results in very porous aggregates (e.g. Kempf et al., 1999). An example is depicted in the right panel of Fig. 6.

As already mentioned in Sect.1 these aggregates have been chosen as prototypes reflecting different stages in the evolution of dust aggregates. When dealing with dust aggregates of different porosities/structure the following equations may serve as easily implementable recipes to account for erosion.

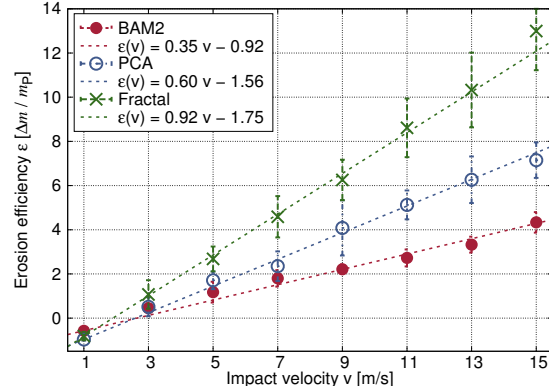


Fig. 7. Erosion efficiency for different types of aggregates. In general, the erosion efficiency is lower for compact aggregates. The threshold velocity where two monomers stick to each other is 2.6 ms^{-1} . Around this velocity we observe the transition from accretion to erosion.

4.2. Results

Using the sample aggregates described in Sect. 4.1 we determine the erosion efficiency in the following way:

First, a given number of single monomers (from now on referred to as projectiles) is randomly distributed around the target in such a way, that their trajectories will hit the target with an impact parameter b between 0 and 1. The impact parameter is chosen such that the number of impacts per cross section area are constant. To avoid projectiles interfering with each other we restrict the total number of incoming projectiles to 20. A lower number of projectiles is used when increasing their size in Sect. 4.3. The erosion efficiency is calculated in the same way as described in Sect. 3.1.

We perform simulations for impact velocities from 1 ms^{-1} to 15 ms^{-1} . Note that the velocity range has been chosen to compare our results to the calibration experiments. Even in turbulent disks impact velocities of 15 ms^{-1} are quite high for mm-sized aggregates (e.g. Brauer et al., 2008).

For each velocity, we perform 5 simulations with a different initial distribution of the projectiles and average over the results. As the fractal aggregates have an inhomogeneous density, we use 5 different aggregates of similar size / structure.

The results are shown in Fig. 7. For low velocities the erosion efficiency approaches a value of -1 which corresponds to accretion rather than erosion. For both, the compact BAM2 and the rather porous PCA aggregate, the transition from accretion to erosion occurs at an impact velocity of $v \approx 2 \text{ ms}^{-1}$. As one would expect we observe a lower erosion efficiency for the “hardened” BAM2 aggregates. For $v = 15 \text{ ms}^{-1}$ the erosion efficiency measured for any of the target aggregates is well above the corresponding value of 1.9 obtained from the calibration simulations. As already explained in the last paragraph of Sect. 3.2, this is expected when the target is bombarded from random directions.

To derive simple recipes for the dependency of the erosion efficiency ϵ on the impact velocity v we determined fit curves for the different aggregate types. Based on the results shown in Fig. 7 we chose a linear fit. We find

$$\epsilon_{\text{BAM2}}(v) = 0.35v - 0.92, \quad (3)$$

$$\epsilon_{\text{PCA}}(v) = 0.60v - 1.56, \quad (4)$$

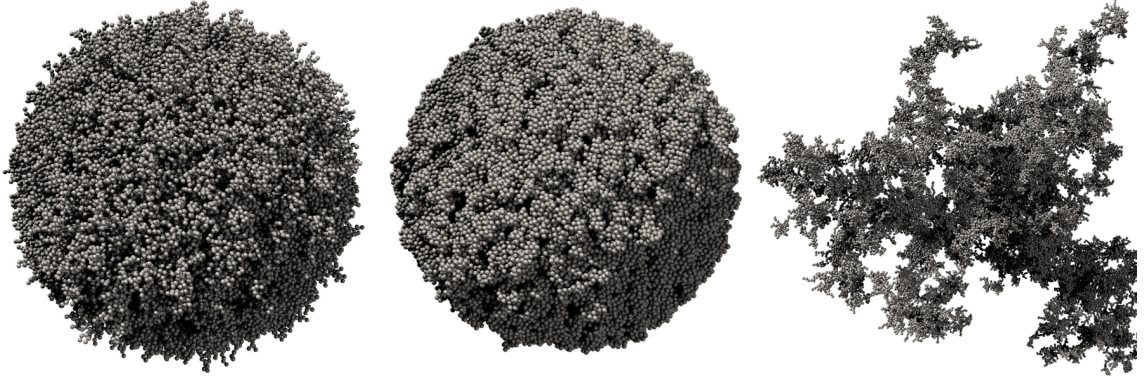


Fig. 6. Sample aggregates used in this work. *Left:* PCA aggregate ($n_c = 2$) with $8 \cdot 10^4$ monomers and a diameter of $100 \mu\text{m}$. *Center:* BAM aggregate consisting of $1.5 \cdot 10^5$ monomers with $n_c = 6$ and a diameter of $100 \mu\text{m}$. *Right:* Fractal aggregate ($n_c \approx 2$) consisting of $6 \cdot 10^4$ monomers and a maximum diameter of $\approx 280 \mu\text{m}$.

$$\epsilon_{\text{frac}}(v) = 0.92v - 1.75, \quad (5)$$

where v is given in ms^{-1} . Note that these fits should be applied with care for velocities below 1ms^{-1} . Negative values of $\epsilon(v)$ correspond to accretion, where $\epsilon = -1$ means that all incoming projectiles have been accreted onto the target. Obviously, values below -1 do not represent any physical process and are just an artifact of the fitting process. As accretion is dominating for low velocities, it applies

$$\lim_{v \rightarrow 0} \epsilon(v) = -1. \quad (6)$$

It is important to note that the erosion efficiency for the fractal aggregates has been determined in a different way than explained in Sect. 3.1. As the impact velocities of the projectiles increase, sometimes whole “fractal arms” are chopped off the main aggregate. However, this process resembles fragmentation rather than erosion. Thus, we only count the monomers of fragments that consist of fewer than 10 monomers when determining the erosion efficiency. In case of the more compact aggregates fragments consisting of more than two to three monomers are very rarely to be found. Thus, the both methods to determine the erosion efficiency return the same values.

We were curious whether we could reproduce the passivation effect we observed in our calibration simulations for aggregates. For this purpose we repeatedly shot 50 projectiles at the PCA aggregate (left panel of Fig. 6). After every barrage the erosion efficiency was measured and the fragments were removed. We choose the PCA aggregate because its structure is very similar to the RBD samples used for the calibration. However, no decline of the erosion efficiency was observed (see Fig. 8). Initially, the average coordination number of the PCA aggregate is 2. As a result of the bombardment monomers are pushed inwards which leads to an increase of the average coordination number of the aggregate. This supports the assumption that the “holes and pillars” shown in Fig. 4 play a key role for the accretion of incoming projectiles.

4.3. Influence of the projectile size

So far, the projectiles consisted of only a single monomer. However, aggregates of different sizes will be present in a protoplanetary disk. Thus, we extend our study to larger projectiles

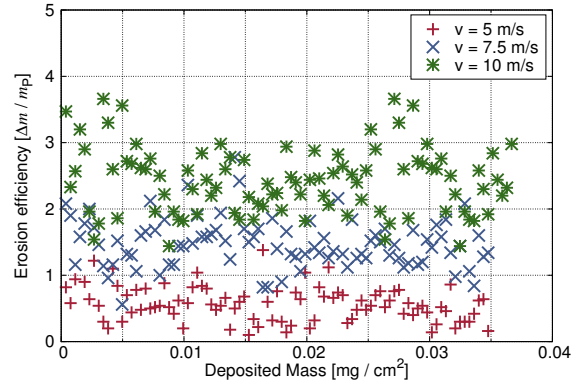


Fig. 8. Evolution of the erosion efficiency with an increasing amount of the deposited mass. The target was a PCA aggregate with a diameter of $100 \mu\text{m}$. Each data point corresponds to the average erosion efficiency measured after shooting in 100 monomers. Contrary to the calibration setup no passivation effect is observed.

which are generated by particle-cluster aggregation. The size of the projectile aggregates lies between two and a few thousand monomers, which means that their mass remains at least an order of magnitude below the target mass.

In the following simulations the PCA aggregates with the properties specified in Fig. 6 serve as targets. As shown in Fig. 9 the projectile size heavily influences the outcome of our simulations. For increasing size of the projectiles the erosion efficiency drops. At first glance, this may seem counterintuitive. The key to understand this observation lies in the, compared to the target, low mass of projectile. While the kinetic energy of a single monomer suffices to knock a few monomers out of the target aggregate, it is vastly below the energy threshold required to disrupt the entire aggregate. When the first monomers of the projectile hit the target monomers are knocked out. However, subsequent parts of the incoming projectile may push these eroded monomers back toward the target where they may get reacceted. For small projectiles there is a higher probability for eroded monomers to escape from the target aggregate.

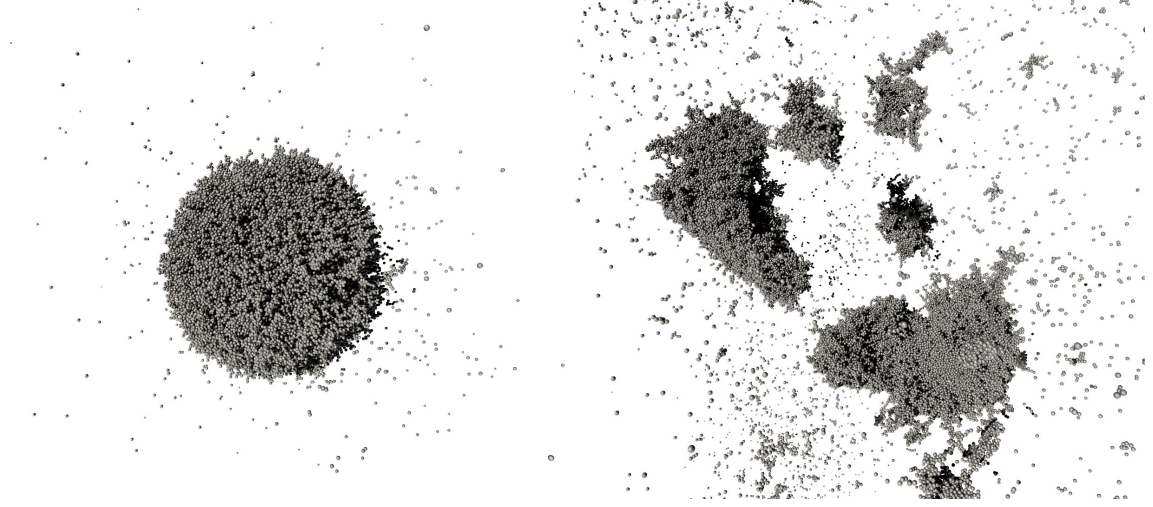


Fig. 10. Depending on the size of the projectiles the outcome changes from erosion to fragmentation. In both cases the impact velocity was 15 ms^{-1} . *Left:* Erosion after shooting in 25 projectiles each consisting of 4 monomers. *Right:* Fragmentation after shooting in 4 projectiles each consisting of 4096.

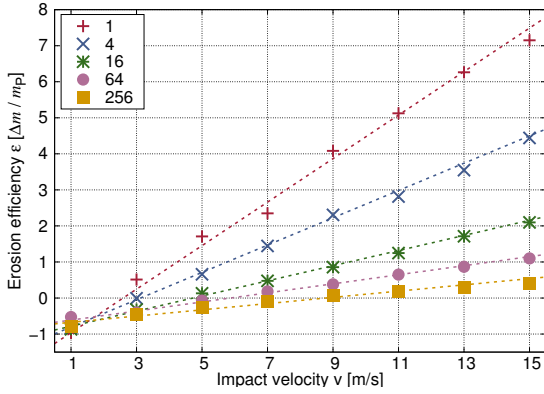


Fig. 9. Comparison of the erosion efficiency for different projectile sizes (in monomers). The PCA target has the same properties as the one depicted in Fig. 6. With growing projectile mass the transition from accretion to erosion is shifted to higher velocities.

In the context of planet formation the growth of larger bodies is a key issue. Therefore we are especially interested in the velocity $v_{A \rightarrow E}$ at which the transition from accretion to erosion occurs. For this purpose we first determine linear fits $\epsilon(v) = av + b$ for the results as depicted in Fig. 9. Then, $v_{A \rightarrow E}$ can be calculated via $v_{A \rightarrow E} = -(b/a)$. To examine the influence of the porosity of the target, we used rather fluffy PCA aggregates (see Fig. 9) as well as compact BAM2 aggregates (not shown) as targets.

Independent of the porosity of the target, we find that $v_{A \rightarrow E}$ increases significantly with growing projectile mass (see Fig. 11). For projectiles consisting of only a single monomer we find $v_{A \rightarrow E} = 2.6 \text{ ms}^{-1}$ and $v_{A \rightarrow E} = 2.64 \text{ ms}^{-1}$ for PCA and BAM2 targets, respectively. Indeed, this is equivalent to the critical sticking velocity of two spherical grains predicted using the theory of Krijt et al. (2013). For smaller projectiles between 1 and 256 monomer masses, we determined a fit for the transition

velocity

$$v_{A \rightarrow E, \text{PCA}}(N) = 0.89N^{0.37} + 1.71, \quad (7)$$

and

$$v_{A \rightarrow E, \text{BAM2}}(N) = 3.34N^{0.24} - 0.74, \quad (8)$$

where N denotes the number of monomers of the projectile (see dashed curve in Fig. 11).

For larger projectiles the measured threshold velocities $v_{A \rightarrow E}$ do not follow the fits given in Eqs. 7 and 8 anymore. This can be explained by the transition from the erosion to the fragmentation regime. In the erosion regime the vast majority of fragments is tiny (below 10 monomers) whereas in the fragmentation regime the impact energy of the projectiles is sufficient to shatter the target into larger fragments (see Fig. 10). From the mass m_T of the target we can estimate the mass ratio, where the collision outcome is dominated by fragmentation. For the data shown in Fig. 11, the critical projectile mass is between $256 - 512 m_P$ and $m_{\text{PCA}} = 8 \cdot 10^4 m_P$, $m_{\text{BAM2}} = 1.5 \cdot 10^5 m_P$, where m_P denotes the mass of a single monomer. Thus, the fragmentation regime is entered when the projectile mass exceeds roughly 0.5% of the target mass.

Though the exact values differ, the evolution of $v_{A \rightarrow E}$ for PCA and BAM2 targets is qualitatively very similar (see Fig. 11). Concerning the formation of larger bodies this is a positive result because it indicates that, regardless of the porosity of the target, growth is possible at velocities that are considerably above the sticking velocity of two individual dust grains.

In laboratory experiments, mass growth was found at velocities of about 50 ms^{-1} (Teiser & Wurm, 2009). Recently, Meisner et al. (2013) studied high velocity impacts of SiO_2 dust aggregates and found that growth is possible at velocities of $\approx 70 \text{ ms}^{-1}$. These velocities are considerably higher than our results. However, the size regime is completely different: The size of the projectiles used by Meisner et al. (2013) is comparable to the size of our target aggregates. Since the maximum value for $v_{A \rightarrow E}$ is limited by the onset of fragmentation we expect to observe accretion at higher velocities when using cm-

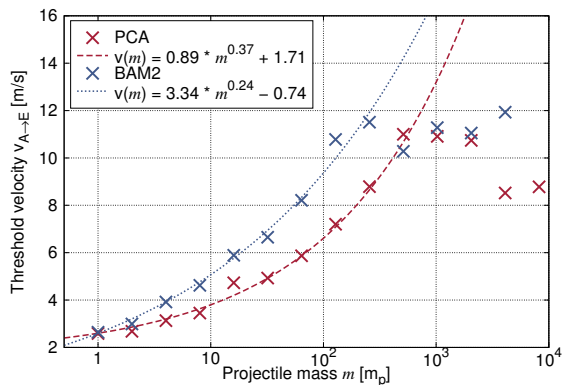


Fig. 11. Threshold velocity $v_{A \rightarrow E}$ where the transition from accretion to erosion occurs for different projectile sizes (in monomers). The targets are the same PCA and BAM2 aggregates as depicted in Fig. 6. At first, $v_{A \rightarrow E}$ increases with growing projectile mass. When the projectiles become too massive $v_{A \rightarrow E}$ drops as the collisions enter the fragmentation regime.

to decimeter-sized target aggregates. Unfortunately, numerical simulations of aggregates of mm size and above are infeasible with the currently available computing power.

5. Conclusions

Let us briefly summarize the key results of this work. First of all, in Sect. 3.1 we have shown that the JKR description of the repulsion and adhesion between two microscopic silicate grains fails to reproduce the erosion efficiency measured in laboratory experiments by a factor of about 20. By extending the interaction model by a visco-elastic damping force we obtain very good agreement between numerical simulations and laboratory experiments for collision velocities below 30 ms^{-1} . Thus, it is crucial to take this additional damping force into account for any further simulations of dust aggregates in the velocity regime of ms^{-1} .

Secondly, we found that the passivation effect observed in laboratory experiments originates from the artificial setup (see Sect. 3.2). In the context of dust growth in a protoplanetary disk passivation against erosion does not play an important role.

In Sect. 4.2 we studied how much different types of aggregates are affected by erosion. Especially the fluffy, fractal aggregates that form during the Brownian motion driven growth phase are prone to erosion. Despite their rather compact surface we find that even the BAM2 aggregates suffer from erosion, though less than the fractal or PCA aggregates. We provide simple recipes to quantify the erosion efficiency for the different aggregate types.

We also examine the influence of the projectile size. Indeed, it turns out that the transition from accretion to erosion is shifted to higher velocities as the projectiles become larger (see Sect. 4.3). The possibility of accretion at impact velocities of 20 ms^{-1} and above helps the growth of larger bodies.

At this point it is hard to judge how these results influence the growth process in protoplanetary disks. For a single impact, we have shown that the erosion efficiency depends on the impact velocity, the structure of the target aggregate as well as the size of the projectile. The prevalence of such impacts is determined by the abundance of small projectiles and the turbulence. As already mentioned in Sect. 1, the amount of small grains will be depleted

rapidly by collisional growth to larger aggregates (Dullemond & Dominik, 2005). In this work, we have shown that erosion (especially as long as the target aggregates are fluffy and fractal) will produce a steady stream of small dust grains. Therefore it could help to replenish the pool of small grains. The final outcome of this complex interplay of different effects will have to be determined by future simulations of the collisional evolution of dust aggregates in protoplanetary disks.

Acknowledgements. A. Seizinger acknowledges the support through the German Research Foundation (DFG) grant KL 650/16. The authors acknowledge support through DFG grant KL 650/7 within the collaborative research group FOR 759 *The formation of planets*. Dust studies at Leiden Observatory are supported through the Spinoza Premie of the Dutch science agency, NWO. The authors thank Carsten Güttler and Jürgen Blum (TU Braunschweig) for inspiring discussions.

References

- Birnstiel, T., Dullemond, C. P., & Brauer, F. 2010, *A&A*, 513, A79
 Blum, J. & Schräpler, R. 2004, *Phys. Rev. Lett.*, 93, 115503
 Blum, J. & Wurm, G. 2000, *Icarus*, 143, 138
 Blum, J. & Wurm, G. 2008, *ARA&A*, 46, 21
 Blum, J., Wurm, G., Kempf, S., & Henning, T. 1996, *Icarus*, 124, 441
 Brauer, F., Dullemond, C. P., & Henning, T. 2008, *A&A*, 480, 859
 de Beule, C., Kelling, T., Wurm, G., Teiser, J., & Jankowski, T. 2013, *ApJ*, 763, 11
 Dominik, C. & Tielens, A. G. G. M. 1995, *Philosophical Magazine, Part A*, 72, 783
 Dominik, C. & Tielens, A. G. G. M. 1996, *Philosophical Magazine, Part A*, 73, 1279
 Dominik, C. & Tielens, A. G. G. M. 1997, *ApJ*, 480, 647
 Drazkowska, J., Windmark, F., & Dullemond, C. P. 2013, *A&A*, 556, A37
 Dullemond, C. P. & Dominik, C. 2005, *A&A*, 434, 971
 Güttler, C., Blum, J., Zsom, A., Ormel, C. W., & Dullemond, C. P. 2010, *A&A*, 513, A56
 Güttler, C., Krause, M., Geretshauer, R. J., Speith, R., & Blum, J. 2009, *ApJ*, 701, 130
 Johnson, K. L., Kendall, K., & Roberts, A. D. 1971, *Royal Society of London Proceedings Series A*, 324, 301
 Kelling, T. & Wurm, G. 2011, *ApJ*, 733, 120
 Kempf, S., Pfalzner, S., & Henning, T. K. 1999, *Icarus*, 141, 388
 Krijt, S., Güttler, C., Heielmann, D., Dominik, C., & Tielens, A. G. G. M. 2013, *J Phys D in press*
 Meisner, T., Wurm, G., Teiser, J., & Schywek, M. 2013, *A&A submitted*
 Okuzumi, S. 2009, *ApJ*, 698, 1122
 Okuzumi, S., Tanaka, H., Takeuchi, T., & Sakagami, M.-a. 2011, *ApJ*, 731, 95
 Ormel, C. W., Spaans, M., & Tielens, A. G. G. M. 2007, *A&A*, 461, 215
 Paszun, D. & Dominik, C. 2008, *A&A*, 484, 859
 Poppe, T., Blum, J., & Henning, T. 2000, *ApJ*, 533, 454
 Schräpler, R. & Blum, J. 2011, *ApJ*, 734, 108
 Seizinger, A. & Kley, W. 2013, *A&A*, 551, A65
 Seizinger, A., Speith, R., & Kley, W. 2012, *A&A*, 541, A59
 Shen, Y., Draine, B. T., & Johnson, E. T. 2008, *ApJ*, 689, 260
 Teiser, J. & Wurm, G. 2009, *MNRAS*, 393, 1584
 Thornton, C. & Ning, Z. 1998, *Powder Technology*, 99, 154
 Wada, K., Tanaka, H., Suyama, T., Kimura, H., & Yamamoto, T. 2007, *ApJ*, 661, 320
 Williams, J. P. & Cieza, L. A. 2011, *ARA&A*, 49, 67
 Windmark, F., Birnstiel, T., Güttler, C., et al. 2012, *A&A*, 540, A73
 Wurm, G. & Krauss, O. 2006, *Physical Review Letters*, 96, 134301
 Zsom, A. & Dullemond, C. P. 2008, *A&A*, 489, 931

4 Summary & Outlook

In this chapter I will give a brief overview of the results obtained within the scope of this thesis and discuss their implications.

4.1 Implications for the interaction model

The key result of [Seizinger et al. \(2012\)](#) is that the compression behavior predicted by the interaction model used in earlier works ([Dominik and Tielens, 1997](#); [Wada et al., 2007](#)) is too soft. Using a similar setup as [Güttler et al. \(2009\)](#), porous dust aggregates could be compressed much more easily in numerical simulations. To overcome this discrepancy [Seizinger et al. \(2012\)](#) introduced two new parameters m_r and m_s that modify the strength of the rolling and sliding interaction. Excellent agreement with the laboratory experiments was obtained for $m_r = 8$ and $m_s = 2.5$. Increasing the strength of the rolling and sliding interaction raises the stiffness of the material. When comparing videos of experiments and visualizations of earlier numerical simulations it has been suspected that the behavior predicted by the latter is too soft.

A second major modification of the original interaction model was proposed by [Krijt et al. \(2013\)](#). Based on theoretical considerations and comparison with numerous laboratory experiments they proposed to extend the JKR interaction model ([Johnson et al., 1971](#)) by adding a visco-elastic damping force. Recently, [Seizinger et al. \(2013a\)](#) have shown that this extension of the interaction model is essential to reproduce results from high velocity erosion experiments ([Schräpler and Blum, 2011](#)). Without this additional damping mechanism the erosion efficiency determined in the numerical simulations exceeded the one measured in the laboratory experiments by a factor of 40.

In summary, it can be said that in the wake of this thesis two major improvements have been applied to the interaction model: the stiffness of the interaction has been increased significantly and much more kinetic energy is dissipated by the visco-elastic damping force. These changes heavily affect simulations of other relevant processes such as the compaction of fluffy aggregates or high velocity impacts.

4.2 Implications for MD simulations

The implications discussed in Sect. 4.1 are primarily important for MD simulations that are based on the same micro-mechanical interaction model. But some conclusions affecting MD simulations of porous aggregates in general may be drawn as well.

When studying the bouncing behavior, the first aggregates generated via hexagonal close packing with extraction (CPE). This aggregate type has already been used in earlier works (e.g. [Wada et al., 2011](#)). Because the author of this thesis suspected that the artificial lattice structure would tremendously influence the outcome of simulations, different methods to generate more realistic aggregates have been investigated. Indeed, it turned out that the regular lattice structure of CPE aggregates results in a significantly higher bouncing probability compared to more realistic aggregate structures ([Seizinger and Kley, 2013](#)). Likewise, [Seizinger et al. \(2013b\)](#) have shown that the reaction of porous dust aggregates to external strain depends heavily on the microscopic structure.

These results underline the importance of the method employed to generate sample aggregates for MD simulations. Within this thesis, it has become clear that the behavior of CPE aggregates is very different to aggregates generated via static compaction (SC). Though static compaction is the method of choice for the generation of compact aggregates with a realistic internal structure, the computational demand of the compaction process limits its applicability. Thus, [Seizinger and Kley \(2013\)](#) also studied ballistic aggregation and migration (BAM) aggregates ([Shen et al., 2008](#)) which can be generated quickly. Although the tensile strength of BAM and SC aggregates differs by factor of up to 2 ([Seizinger et al., 2013b](#)), their collision behavior is very similar ([Seizinger and Kley, 2013](#)). Thus, BAM aggregates are very useful when studying collisions of more compact, homogeneous aggregates.

Generating inhomogeneous, fractal aggregates is more difficult. As part of an upcoming paper ([Seizinger et al.](#)), the author will present a simple algorithm that allows the fast generation of aggregates with properties similar to those grown by successive collisions in a protoplanetary disk.

4.3 Implications for SPH simulations

When calibrating SPH simulations with laboratory results, differences between the quasi-static (slow) and dynamic (fast) compaction were taken into consideration ([Güttler et al., 2009](#)). Indeed, [Seizinger et al. \(2012\)](#) found that the compressive strength depends on how fast the compression occurs. Compared to the quasi-static case it becomes easier to compress porous aggregates until a critical compression velocity of $\approx 0.9 \text{ ms}^{-1}$ is reached. At higher compression velocities porous aggregates become harder to compress. This is a critical result, because collisions of macroscopic bodies occur in this velocity regime. [Seizinger et al. \(2012\)](#) provide SPH simulations with simple recipes for the compressive strength of porous dust aggregates spanning a wide range of compression velocities.

Equally important are the tensile and shear strength. The tensile strength could be measured in laboratory experiments ([Blum and Schräpler, 2004](#); [Blum et al., 2006](#)). However, measuring the shear strength of a highly porous dust aggregate has not been possible so far. Until now, SPH simulations had to rely on theoretical estimations (e.g. [Sirono, 2004](#)). After successfully calibrating our interaction model as explained in Sect. 4.1, [Seizinger et al. \(2013b\)](#) determined the shear strength of porous aggregates. Interestingly, they obtained a relation for the shear strength that differs by almost one order of magnitude from [Sirono \(2004\)](#). This indicates that

the approach of [Sirono \(2004\)](#) might not be applicable to porous aggregates.

As a result of this thesis, the compressive, tensile, and shear strength relations are now available, as well as a proper description of the transition from the quasi-static to the dynamic compaction regime. In future work, it will be very interesting to see how these refined material properties will alter the outcome of SPH simulations.

4.4 Implications for the growth of larger bodies

The frequency of bouncing collisions has a tremendous impact on growth of larger bodies. According to [Seizinger and Kley \(2013\)](#) sub-mm sized particles do not bounce off each other unless their filling factor is larger than ≈ 0.5 . Yet, laboratory experiments indicate that the volume filling factor remains below 0.5 during the growth to cm-sized aggregates ([Teiser et al., 2011](#)). Thus, bouncing does not hamper the growth of mm-sized aggregates.

Laboratory experiments show that collisional growth of dust aggregates is possible at velocities of about 50 ms^{-1} ([Teiser and Wurm, 2009](#)). In molecular dynamic simulations fragmentation typically sets in at much lower velocities of a few ms^{-1} (e.g. [Paszun and Dominik, 2009](#); [Seizinger and Kley, 2013](#)). Growth at higher velocities could be observed when using icy particles that are much more sticky ([Wada et al., 2009](#)).

Within this thesis, it has been shown that the mass ratio of the colliding aggregates plays an important role. In [Seizinger et al. \(2013a\)](#) the author determined the threshold velocity at which the transition from accretion to erosion occurs. With growing projectile masses the threshold velocity increases until the impact energy of the projectile suffices to shatter the target aggregate. This means that high velocity collisions may still result in net growth and helps to bridge the gap between MD simulations and laboratory results.

For the first time, [Seizinger et al. \(2013a\)](#) studied the erosion of larger bodies with numerical simulations. As expected, they found that fluffy, fractal aggregates are most vulnerable to erosion. However, even compact aggregates suffer from erosion. The erosion effect quickly diminishes as the projectiles grow larger. [Seizinger et al. \(2013a\)](#) determined simple equations that provide other simulations with the possibility to account for the effects of erosion.

4.5 Outlook

Regarding the growth of dust aggregates several aspects are still poorly understood. The structure of aggregates that form during very first growth phase has been studied in detail, both numerically and experimentally ([Kempf et al., 1999](#); [Blum et al., 2000](#)). Since this growth phase is dominated by Brownian motion collisions are purely hit & stick. As the aggregates grow larger collision velocities will increase which leads to restructuring. Studying how the aggregate structure changes is part of an ongoing project with Andras Zsom ([Seizinger et al.](#)).

This is closely linked with the porosity evolution of larger aggregates. Apart from the impact velocity, the porosity is the key variable that determines the outcome

of a collision. Therefore it is critical to study in detail how the porosity changes as aggregates collide with each other.

In this thesis, only aggregates composed of silicate grains have been studied. Given the necessary material parameters, the numerical method used in this thesis can simulate all kinds of materials. For instance, the collisional behavior of ice aggregates has been studied in earlier works (e.g. [Wada et al., 2008](#)). However, when modeling silicate aggregates [Seizinger et al. \(2012\)](#) and [Seizinger et al. \(2013a\)](#) demonstrated the necessity of proper calibration of the interaction model. The restriction of this thesis to silicate aggregates stems from the lack of laboratory experiments that allow for the calibration of the model for other materials. Recently, the first experiments with micron-sized ice grains have been performed ([Gundlach et al., 2011](#)). Within the near future suitable calibration experiments for ice will likely be available. Future work will cover the collisional behavior and mechanical properties of icy bodies. It will be very interesting to study the behavior of aggregates that are composed of a mixture of dust and ice.

5 Acknowledgements

First of all, I want to express my gratitude to my supervisor Wilhelm Kley for the excellent supervision of my thesis. Not only did he reply very quickly to questions and always found time to discuss the course of my work but he also allowed me to attend a lot of international conferences where I met my later collaborators.

For the fruitful collaboration I want to thank Sebastian Krijt, Andras Zsom, Rainer Schräpler and Jürgen Blum and his group at the TU Braunschweig. I also want to acknowledge the inspiring discussion and valuable input regarding my work from the whole planet formation community, especially Carsten Güttler, Fredrik Windmark and Cornelis Dullemond.

While working on my thesis I was financially supported through the German Research Foundation (DFG) grant KL 650/16 as well as KL 650/7 within the collaborative research group FOR 759 *The formation of planets*.

Some of the simulations were performed on the bwGRiD cluster, which is funded by the Ministry for Education, and Research of Germany and the Ministry for Science, Research and Arts of the state of Baden-Württemberg.

Within in the last few years I greatly enjoyed working in the Computational Physics group at the Institute for Astronomy and Astrophysics Tübingen. I want to thank everybody for the great time and countless inspiring discussions on life in general and planet formation in particular, especially Christoph Schäfer, Marius Hertfelder, Daniel Thun, Sven Riecker and Ralf Geretshauser. Most importantly, I want to thank my long-term colleague and friend Tobias Müller for his help with any kind of problem (and a never ending supply of sweets). Special thanks go to Franziska Adomat for proof-reading the manuscript.

Last but not least, a huge thank you goes to my family for their moral and financial support over the last nine years. Their inspiring example certainly played a part in my starting to work on this thesis.

Bibliography

- N. M. Batalha, W. J. Borucki, S. T. Bryson, L. A. Buchhave, D. A. Caldwell, J. Christensen-Dalsgaard, D. Ciardi, E. W. Dunham, F. Fressin, T. N. Gautier, III, R. L. Gilliland, M. R. Haas, S. B. Howell, J. M. Jenkins, H. Kjeldsen, D. G. Koch, D. W. Latham, J. J. Lissauer, G. W. Marcy, J. F. Rowe, D. D. Sasselov, S. Seager, J. H. Steffen, G. Torres, G. S. Basri, T. M. Brown, D. Charbonneau, J. Christiansen, B. Clarke, W. D. Cochran, A. Dupree, D. C. Fabrycky, D. Fischer, E. B. Ford, J. Fortney, F. R. Girouard, M. J. Holman, J. Johnson, H. Isaacson, T. C. Klaus, P. Machalek, A. V. Moorehead, R. C. Morehead, D. Ragozzine, P. Tenenbaum, J. Twicken, S. Quinn, J. VanCleve, L. M. Walkowicz, W. F. Welsh, E. Devore, and A. Gould. Kepler's First Rocky Planet: Kepler-10b. *Astrophysical Journal*, 729:27, mar 2011. doi: 10.1088/0004-637X/729/1/27.
- T. Birnstiel, C. P. Dullemond, and F. Brauer. Gas- and dust evolution in protoplanetary disks. *Astronomy & Astrophysics*, 513:A79, apr 2010. doi: 10.1051/0004-6361/200913731.
- J. Blum and R. Schräpler. Structure and Mechanical Properties of High-Porosity Macroscopic Agglomerates Formed by Random Ballistic Deposition. *Physical Review Letters*, 93(11):115503, sep 2004. doi: 10.1103/PhysRevLett.93.115503.
- J. Blum and G. Wurm. The Growth Mechanisms of Macroscopic Bodies in Protoplanetary Disks. *Annual Review of Astronomy and Astrophysics*, 46:21–56, sep 2008. doi: 10.1146/annurev.astro.46.060407.145152.
- J. Blum, G. Wurm, S. Kempf, T. Poppe, H. Klahr, T. Kozasa, M. Rott, T. Henning, J. Dorschner, R. Schräpler, H. U. Keller, W. J. Markiewicz, I. Mann, B. A. Gustafson, F. Giovane, D. Neuhaus, H. Fichtig, E. Grün, B. Feuerbacher, H. Kochan, L. Ratke, A. El Goresy, G. Morfill, S. J. Weidenschilling, G. Schwehm, K. Metzler, and W.-H. Ip. Growth and Form of Planetary Seedlings: Results from a Microgravity Aggregation Experiment. *Physical Review Letters*, 85:2426–2429, sep 2000. doi: 10.1103/PhysRevLett.85.2426.
- J. Blum, R. Schräpler, B. J. R. Davidsson, and J. M. Trigo-Rodríguez. The Physics of Protoplanetary Dust Agglomerates. I. Mechanical Properties and Relations to Primitive Bodies in the Solar System. *Astrophysical Journal*, 652:1768–1781, dec 2006. doi: 10.1086/508017.
- A. P. Boss. Giant planet formation by gravitational instability. *Science*, 276:1836–1839, 1997. doi: 10.1126/science.276.5320.1836.

- F. Brauer, C. P. Dullemond, and T. Henning. Coagulation, fragmentation and radial motion of solid particles in protoplanetary disks. *Astronomy & Astrophysics*, 480: 859–877, mar 2008. doi: 10.1051/0004-6361:20077759.
- C. Dominik and A. G. G. M. Tielens. Resistance to rolling in the adhesive contact of two elastic spheres. *Philosophical Magazine, Part A*, 72:783–803, sep 1995. doi: 10.1080/01418619508243800.
- C. Dominik and A. G. G. M. Tielens. Resistance to sliding on atomic scales in the adhesive contact of two elastic spheres. *Philosophical Magazine, Part A*, 73: 1279–1302, may 1996. doi: 10.1080/01418619608245132.
- C. Dominik and A. G. G. M. Tielens. The Physics of Dust Coagulation and the Structure of Dust Aggregates in Space. *Astrophysical Journal*, 480:647, may 1997. doi: 10.1086/303996.
- J. Drażkowska, F. Windmark, and C. P. Dullemond. Planetesimal formation via sweep-up growth at the inner edge of dead zones. *Astronomy & Astrophysics*, 556:A37, aug 2013. doi: 10.1051/0004-6361/201321566.
- C. D. Dressing and D. Charbonneau. The Occurrence Rate of Small Planets around Small Stars. *Astrophysical Journal*, 767:95, apr 2013. doi: 10.1088/0004-637X/767/1/95.
- P. Garaud, F. Meru, M. Galvagni, and C. Olczak. From Dust to Planetesimals: An Improved Model for Collisional Growth in Protoplanetary Disks. *Astrophysical Journal*, 764:146, feb 2013. doi: 10.1088/0004-637X/764/2/146.
- R. J. Geretshauser, R. Speith, C. Güttler, M. Krause, and J. Blum. Numerical simulations of highly porous dust aggregates in the low-velocity collision regime. Implementation and calibration of a smooth particle hydrodynamics code. *Astronomy & Astrophysics*, 513:A58, apr 2010. doi: 10.1051/0004-6361/200913596.
- R. J. Geretshauser, R. Speith, and W. Kley. Collisions of inhomogeneous pre-planetesimals. *Astronomy & Astrophysics*, 536:A104, dec 2011. doi: 10.1051/0004-6361/201117645.
- P. Goldreich and W. R. Ward. The Formation of Planetesimals. *Astrophysical Journal*, 183:1051–1062, aug 1973. doi: 10.1086/152291.
- P. Goldreich, Y. Lithwick, and R. Sari. Planet Formation by Coagulation: A Focus on Uranus and Neptune. *Annual Review of Astronomy and Astrophysics*, 42: 549–601, sep 2004. doi: 10.1146/annurev.astro.42.053102.134004.
- R. Greenberg, W. K. Hartmann, C. R. Chapman, and J. F. Wacker. Planetesimals to planets - Numerical simulation of collisional evolution. *Icarus*, 35:1–26, jul 1978. doi: 10.1016/0019-1035(78)90057-X.
- B. Gundlach, S. Kiliyas, E. Beitz, and J. Blum. Micrometer-sized ice particles for planetary-science experiments - I. Preparation, critical rolling friction force, and

-
- specific surface energy. *Icarus*, 214:717–723, aug 2011. doi: 10.1016/j.icarus.2011.05.005.
- C. Güttler, M. Krause, R. J. Geretshauser, R. Speith, and J. Blum. The Physics of Protoplanetesimal Dust Agglomerates. IV. Toward a Dynamical Collision Model. *Astrophysical Journal*, 701:130–141, aug 2009. doi: 10.1088/0004-637X/701/1/130.
- C. Güttler, J. Blum, A. Zsom, C. W. Ormel, and C. P. Dullemond. The outcome of protoplanetary dust growth: pebbles, boulders, or planetesimals?. I. Mapping the zoo of laboratory collision experiments. *Astronomy & Astrophysics*, 513:A56, apr 2010. doi: 10.1051/0004-6361/200912852.
- K. E. Haisch, Jr., E. A. Lada, and C. J. Lada. Disk Frequencies and Lifetimes in Young Clusters. *Astrophysical Journal Letters*, 553:L153–L156, jun 2001. doi: 10.1086/320685.
- D. Heielmann, J. Blum, H. J. Fraser, and K. Wolling. Microgravity experiments on the collisional behavior of saturnian ring particles. *Icarus*, 206:424–430, apr 2010. doi: 10.1016/j.icarus.2009.08.009.
- T. Jankowski, G. Wurm, T. Kelling, J. Teiser, W. Sabolo, P. J. Gutirrez, and I. Bertini. Crossing barriers in planetesimal formation: The growth of mm-dust aggregates with large constituent grains. *Astronomy & Astrophysics*, 542:A80, jun 2012. doi: 10.1051/0004-6361/201218984.
- K. L. Johnson, K. Kendall, and A. D. Roberts. Surface Energy and the Contact of Elastic Solids. *Royal Society of London Proceedings Series A*, 324:301–313, sep 1971. doi: 10.1098/rspa.1971.0141.
- S. Kempf, S. Pfalzner, and T. K. Henning. N-Particle-Simulations of Dust Growth. I. Growth Driven by Brownian Motion. *Icarus*, 141:388–398, oct 1999. doi: 10.1006/icar.1999.6171.
- E. Kokubo and S. Ida. Oligarchic Growth of Protoplanets. *Icarus*, 131:171–178, jan 1998. doi: 10.1006/icar.1997.5840.
- E. Kokubo and S. Ida. Formation of Protoplanet Systems and Diversity of Planetary Systems. *Astrophysical Journal*, 581:666–680, dec 2002. doi: 10.1086/344105.
- R. K. Kopparapu. A Revised Estimate of the Occurrence Rate of Terrestrial Planets in the Habitable Zones around Kepler M-dwarfs. *Astrophysical Journal Letters*, 767:L8, apr 2013. doi: 10.1088/2041-8205/767/1/L8.
- S. Krijt, C. Gttler, D. Heielmann, C. Dominik, and A. G. G. M. Tielens. Energy dissipation in head-on collisions of spheres. *accepted for publication in J Phys D*, 2013.
- M. Mayor and D. Queloz. A Jupiter-mass companion to a solar-type star. *Nature*, 378:355–359, nov 1995. doi: 10.1038/378355a0.

- C. W. Ormel, M. Spaans, and A. G. G. M. Tielens. Dust coagulation in protoplanetary disks: porosity matters. *Astronomy & Astrophysics*, 461:215–232, jan 2007. doi: 10.1051/0004-6361:20065949.
- D. Paszun and C. Dominik. Numerical determination of the material properties of porous dust cakes. *Astronomy & Astrophysics*, 484:859–868, jun 2008. doi: 10.1051/0004-6361:20079262.
- D. Paszun and C. Dominik. Collisional evolution of dust aggregates. From compaction to catastrophic destruction. *Astronomy & Astrophysics*, 507:1023–1040, nov 2009. doi: 10.1051/0004-6361/200810682.
- J. B. Pollack, O. Hubickyj, P. Bodenheimer, J. J. Lissauer, M. Podolak, and Y. Greenzweig. Formation of the Giant Planets by Concurrent Accretion of Solids and Gas. *Icarus*, 124:62–85, nov 1996. doi: 10.1006/icar.1996.0190.
- H. Rein. A proposal for community driven and decentralized astronomical databases and the Open Exoplanet Catalogue. *ArXiv e-prints*, nov 2012. URL <http://arxiv.org/abs/1211.7121>.
- C. Schäfer, R. Speith, and W. Kley. Collisions between equal-sized ice grain agglomerates. *Astronomy & Astrophysics*, 470:733–739, aug 2007. doi: 10.1051/0004-6361:20077354.
- R. Schräpler and J. Blum. The Physics of Protoplanetary Dust Agglomerates. VI. Erosion of Large Aggregates as a Source of Micrometer-sized Particles. *Astrophysical Journal*, 734:108, jun 2011. doi: 10.1088/0004-637X/734/2/108.
- R. Schräpler, J. Blum, A. Seizinger, and W. Kley. The Physics of Protoplanetary Dust Agglomerates. VII. The Low-velocity Collision Behavior of Large Dust Agglomerates. *Astrophysical Journal*, 758:35, oct 2012. doi: 10.1088/0004-637X/758/1/35.
- A. Seizinger and W. Kley. Bouncing behavior of microscopic dust aggregates. *Astronomy & Astrophysics*, 551:A65, mar 2013. doi: 10.1051/0004-6361/201220946.
- A. Seizinger, A. Zsom, and W. Kley. Simulating dust growth in protoplanetary disks. *in preparation*.
- A. Seizinger, R. Speith, and W. Kley. Compression behavior of porous dust agglomerates. *Astronomy & Astrophysics*, 541:A59, may 2012. doi: 10.1051/0004-6361/201218855.
- A. Seizinger, S. Krijt, and W. Kley. Erosion of dust aggregates. *Astronomy & Astrophysics (in press)*, oct 2013a.
- A. Seizinger, R. Speith, and W. Kley. Tensile & shear strength of porous dust agglomerates. *Astronomy & Astrophysics (in press)*, aug 2013b.

- Y. Shen, B. T. Draine, and E. T. Johnson. Modeling Porous Dust Grains with Ballistic Aggregates. I. Geometry and Optical Properties. *Astrophysical Journal*, 689:260–275, dec 2008. doi: 10.1086/592765.
- F. H. Shu, F. C. Adams, and S. Lizano. Star formation in molecular clouds - Observation and theory. *Annual Review of Astronomy and Astrophysics*, 25:23–81, 1987. doi: 10.1146/annurev.aa.25.090187.000323.
- S.-I. Sirono. Conditions for collisional growth of a grain aggregate. *Icarus*, 167:431–452, feb 2004. doi: 10.1016/j.icarus.2003.09.018.
- M. V. Smoluchowski. Drei Vortrage uber Diffusion, Brownsche Bewegung und Koagulation von Kolloidteilchen. *Zeitschrift fur Physik*, 17:557–585, 1916.
- J. Teiser and G. Wurm. High-velocity dust collisions: forming planetesimals in a fragmentation cascade with final accretion. *Monthly Notices of the Royal Astronomical Society*, 393:1584–1594, mar 2009. doi: 10.1111/j.1365-2966.2008.14289.x.
- J. Teiser, I. Engelhardt, and G. Wurm. Porosities of Protoplanetary Dust Agglomerates from Collision Experiments. *Astrophysical Journal*, 742:5, nov 2011. doi: 10.1088/0004-637X/742/1/5.
- K. Wada, H. Tanaka, T. Suyama, H. Kimura, and T. Yamamoto. Numerical simulation of dust aggregate collisions. i. compression and disruption of two-dimensional aggregates. *Astrophysical Journal*, 661:320–333, may 2007. doi: 10.1086/514332.
- K. Wada, H. Tanaka, T. Suyama, H. Kimura, and T. Yamamoto. Numerical Simulation of Dust Aggregate Collisions. II. Compression and Disruption of Three-Dimensional Aggregates in Head-on Collisions. *Astrophysical Journal*, 677:1296–1308, apr 2008. doi: 10.1086/529511.
- K. Wada, H. Tanaka, T. Suyama, H. Kimura, and T. Yamamoto. Collisional Growth Conditions for Dust Aggregates. *Astrophysical Journal*, 702:1490–1501, sep 2009. doi: 10.1088/0004-637X/702/2/1490.
- K. Wada, H. Tanaka, T. Suyama, H. Kimura, and T. Yamamoto. The Rebound Condition of Dust Aggregates Revealed by Numerical Simulation of Their Collisions. *Astrophysical Journal*, 737:36, aug 2011. doi: 10.1088/0004-637X/737/1/36.
- S. J. Weidenschilling. Aerodynamics of solid bodies in the solar nebula. *Monthly Notices of the Royal Astronomical Society*, 180:57–70, jul 1977.
- R. Weidling, C. Güttler, J. Blum, and F. Brauer. The Physics of Protoplanetary Dust Agglomerates. III. Compaction in Multiple Collisions. *Astrophysical Journal*, 696:2036–2043, may 2009. doi: 10.1088/0004-637X/696/2/2036.
- R. Weidling, C. Güttler, and J. Blum. Free collisions in a microgravity many-particle experiment. I. Dust aggregate sticking at low velocities. *Icarus*, 218:688–700, mar 2012. doi: 10.1016/j.icarus.2011.10.002.

- G. W. Wetherill and G. R. Stewart. Accumulation of a swarm of small planetesimals. *Icarus*, 77:330–357, feb 1989. doi: 10.1016/0019-1035(89)90093-6.
- J. P. Williams and L. A. Cieza. Protoplanetary Disks and Their Evolution. *Annual Review of Astronomy and Astrophysics*, 49:67–117, sep 2011. doi: 10.1146/annurev-astro-081710-102548.
- L. Wilson, K. Keil, and S. J. Love. The internal structures and densities of asteroids. *Meteoritics and Planetary Science*, 34:479–483, may 1999. doi: 10.1111/j.1945-5100.1999.tb01355.x.
- F. Windmark, T. Birnstiel, C. Güttler, J. Blum, C. P. Dullemond, and T. Henning. Planetesimal formation by sweep-up: how the bouncing barrier can be beneficial to growth. *Astronomy & Astrophysics*, 540:A73, apr 2012. doi: 10.1051/0004-6361/201118475.
- A. Zsom and C. P. Dullemond. A representative particle approach to coagulation and fragmentation of dust aggregates and fluid droplets. *Astronomy & Astrophysics*, 489:931–941, oct 2008. doi: 10.1051/0004-6361:200809921.
- A. Zsom, C. W. Ormel, C. Güttler, J. Blum, and C. P. Dullemond. The outcome of protoplanetary dust growth: pebbles, boulders, or planetesimals? II. Introducing the bouncing barrier. *Astronomy & Astrophysics*, 513:A57, apr 2010. doi: 10.1051/0004-6361/200912976.
- A. Zsom, C. W. Ormel, C. P. Dullemond, and T. Henning. The outcome of protoplanetary dust growth: pebbles, boulders, or planetesimals?. III. Sedimentation driven coagulation inside the snowline. *Astronomy & Astrophysics*, 534:A73, oct 2011. doi: 10.1051/0004-6361/201116515.